Response and feedback of sea ice, terrestrial organic carbon, and meltwater discharge to last deglacial climate change (Beaufort Sea, Arctic Ocean)

Kumulative Dissertation

zur Erlangung des akademischen Grades

eines Doktors der Naturwissenschaften

-Dr. rer. nat.-

am Fachbereich Geowissenschaften

der Universität Bremen

vorgelegt von

Junjie Wu

Bremerhaven, 2021

Gutachter der Dissertation:

Prof. Dr. Rüdiger Stein

Prof. Dr. Ralph Schneider

Ph.D. Colloquium

Deglacial ice-sheet retreat and terrestrial organic carbon remobilization in northwestern Canada – A sedimentary record from the Beaufort Sea

October 13, 2021

Versicherung an Eides Statt / *Affirmation in lieu of an oath*

gem. § 5 Abs. 5 der Promotionsordnung vom 18.06.2018 /
according to § 5 (5) of the Doctoral Degree Rules and Regulations of 18 June, 2018

Ich / I, Junjie Wu, Schönianstraße 17, 27570 Bremerhaven, 3154155

(Vorname / First *Name*, Name / *Name*, Anschrift / *Address*, ggf. Matr.-Nr. / *student ID no., if applicable*)

versichere an Eides Statt durch meine Unterschrift, dass ich die vorliegende Dissertation selbständig und ohne fremde Hilfe angefertigt und alle Stellen, die ich wörtlich dem Sinne nach aus Veröffentlichungen entnommen habe, als solche kenntlich gemacht habe, mich auch keiner anderen als der angegebenen Literatur oder sonstiger Hilfsmittel bedient habe und die zu Prüfungszwecken beigelegte elektronische Version (PDF) der Dissertation mit der abgegebenen gedruckten Version identisch ist. / *With my signature I affirm in lieu of an oath that I prepared the submitted dissertation independently and without illicit assistance from third parties, that I appropriately referenced any text or content from other sources, that I used only literature and resources listed in the dissertation, and that the electronic (PDF) and printed versions of the dissertation are identical.*

Ich versichere an Eides Statt, dass ich die vorgenannten Angaben nach bestem Wissen und Gewissen gemacht habe und dass die Angaben der Wahrheit entsprechen und ich nichts verschwiegen habe. */ I affirm in lieu of an oath that the information provided herein to the best of my knowledge is true and complete.*

Die Strafbarkeit einer falschen eidesstattlichen Versicherung ist mir bekannt, namentlich die Strafandrohung gemäß § 156 StGB bis zu drei Jahren Freiheitsstrafe oder Geldstrafe bei vorsätzlicher Begehung der Tat bzw. gemäß § 161 Abs. 1 StGB bis zu einem Jahr Freiheitsstrafe oder Geldstrafe bei fahrlässiger Begehung. / *I am aware that a false affidavit is a criminal offence which is punishable by law in accordance with § 156 of the German Criminal Code (StGB) with up to three years imprisonment or a fine in case of intention, or in accordance with § 161 (1) of the German Criminal Code with up to one year imprisonment or a fine in case of negligence.*

Bremerhaven, 2021/08/04

Ort / *Place*, Datum / *Date*

Unterschrift / *Signature*

TABLE OF CONTENT

Abstract

Earth's climate system is changing rapidly under global warming. For instance, in the polar region, the Arctic Ocean is losing sea ice, which can influence the heat flux, albedo effect, "Arctic Amplification" (additional warming), and the Atlantic Meridional Overturning Circulation. Besides, permafrost temperatures are increasing to record high levels, and the permafrost is expected to release additional CO_2 and CH_4 to the atmosphere. These variabilities of the Arctic components have been proposed as responses to anthropogenic activities. However, the climate system is of complexity. The distinction of variability between anthropogenic forcing and natural (external and internal) forcing will help us to understand the complex climate system and improve our future predictions. The transition from the Last Glacial Maximum to the Holocene is an ideal time frame to study the natural variability of the Arctic components as a response to external forcing and subsequent internal feedbacks.

In this context, we performed a detailed study of a sediment core from the Canadian Beaufort Sea (core ARA04C/37), reconstructing sea-ice history, ancient terrestrial organic carbon mobilization (petrogenic organic carbon and permafrost carbon), and meltwater discharge. Sea-ice reconstruction has been achieved by analyses of multiple biomarkers, e.g., sea-ice biomarker IP_{25}, HBI-III, and specific sterols. In order to conduct a comprehensive reconstruction of the surface water characteristics, more biomarkers (e.g., long-chain diols and GDGTs) were used. For the study of ancient terrestrial organic carbon remobilization, radiocarbon dating was applied on both terrestrial compounds (long-chain fatty acids) and bulk organic carbon to characterize the carbon age. Finally, hydrogen isotope analyses were performed on specific compounds (i.e., phytoplankton sterols, short-chain and long-chain fatty acids) to reconstruct the paleo hydrology and the Laurentide Ice Sheet meltwater discharge, with particular interest in the Younger Dryas flood event.

The first study provides insights into the deglacial to Holocene variabilities in sea ice and surface water characteristics in the Beaufort Sea. This region was nearly ice free and characterized by variable sea surface temperatures (>0 °C) during the transition from the deglaciation to the early Holocene (~14-8 kyr BP). Throughout the mid-late Holocene (~8-0 kyr BP) a seasonal sea-ice cover developed with sea surface temperatures below 0 °C. Based on specific biomarkers ("HBI-III") indicative for marginal ice zone (MIZ), we further propose that the core site was probably close to a winter MIZ at ca. 5.6 kyr BP and to a summer MIZ at ca. 3.5 kyr BP. The changes in sea ice were most likely driven by changes in solar insolation. Besides, two events of high sediment flux at this core site were documented at ca. 13 and 11 kyr BP. The first event was attributed to the Younger Dryas flood, and the second event was likely related to coastal erosion induced by rapid sea-level rise.

The second study focuses on the relationship between ice-sheet retreat and ancient terrestrial organic carbon mobilization. Radiocarbon analyses of organic matter archived in core ARA04C/37 in concert with multiple thermal maturity proxies present evidence of enhanced ancient terrestrial carbon fluxes between 14.5-10 kyr BP. During this period, the Laurentide Ice Sheet retreat directly led to exhumation, exposure, and oxidation of

petrogenic organic carbon from bedrocks. Besides, reduction of ice volume has resulted in rapid sea-level rise which has caused permafrost carbon remobilization at ca. 14 and 11 kyr BP by coastal erosion. Assessment of carbon release from the two processes indicate that ice-sheet retreat driven by orbital forcing has played an important role in contributing terrestrial organic carbon to the deglacial CO_2 rise.

The third study addresses paleo hydrological changes in the Canadian Arctic region by hydrogen isotope analyses in the same core ARA04C/37. During the deglaciation (~14-8 kyr BP), the hydrology in the Canadian Beaufort Sea was largely influenced by the meltwater discharge from the Laurentide Ice Sheet. Particularly, an extremely strong freshening at the onset of the Younger Dryas (ca. 13 kyr BP) has been identified, with a sea surface salinity depression of ~24. The cooccurrence of strong freshwater signals in terrestrial and marine biomarkers confirms that the Makenzie River has served as a major outlet for the Younger Dryas flood. During the mid-late Holocene (~8-0 kyr BP), sea surface salinity has increased. It likely resulted from a decreased Mackenzie River discharge, implying a drier climate in the river basin.

In summary, our study on three significant components in the climate system in the Canadian Arctic, i.e., sea ice, ancient terrestrial organic carbon reservoirs, and the Laurentide Ice Sheet meltwater, provides more record evidence of how the Arctic components responded to external forcing and/or subsequent natural internal interactions. These new data will help to better understand the natural variability of the deglacial climate system.

Zusammenfassung

Durch die globale Erwärmung gerät unser Klimasystem zunehmend unter Druck. In der Polarregion beispielsweise verliert der Arktische Ozean an Meereis, was den Wärmefluss, den Albedo-Effekt, die "Arctic Amplification" (zusätzliche Erwärmung) und die atlantische meridionale Umwälzzirkulation beeinflussen kann. Steigende Temperaturen in Permafrostböden führen zur Freisetzung von Gasen wie CO_2 und CH_4 in die Atmosphäre. Diese Veränderungen der arktischen Region gelten als Reaktion anthropogener Aktivitäten was jedoch aufgrund der Komplexität des Klimasystems schwer zu bestimmen ist. Die Unterscheidung zwischen anthropogenem und natürlichem (externen und internen) Einfluss auf das komplexe Klimasystem wird uns dabei helfen, dieses besser zu verstehen und unsere zukünftigen Vorhersagen zu verbessern. Der Übergang vom letzten glazialen Maximum zum Holozän ist eine ideale Zeitspanne um die natürliche Variabilität der arktischen Komponenten als Reaktion auf externe Einflüsse und nachfolgende interne Rückkopplungen zu untersuchen.

In diesem Zusammenhang wurde der Sedimentkern ARA04C/37 aus der kanadischen Beaufortsee untersucht und die Meereisgeschichte, die Mobilisierung von altem terrestrischen, organischen Kohlenstoff (petrogener organischer Kohlenstoff und Kohlenstoff aus Permafrostböden), sowie der Schmelzwasserabfluss rekonstruiert. Die Meereisrekonstruktion erfolgte durch die Analyse mehrerer Biomarker, wie den Meereisproxy IP_{25} und spezifische Sterole. Für eine umfassende Rekonstruktion der Eigenschaften vom Oberflächenwasser wurden weitere Biomarker (z.B. langkettige Diole und GDGTs) verwendet. Für die Untersuchung der Remobilisierung von altem terrestrischen, organischen Kohlenstoff wurden Radiokohlenstoffdatierungen, sowohl für terrestrische Verbindungen (langkettige Fettsäuren) als auch für organischen Kohlenstoff, durchgeführt. Abschließend wurden Wasserstoffisotopenanalysen an speziellen Verbindungen (Phytoplanktonsterole, kurzkettige Fettsäuren und langkettige Fettsäuren) durchgeführt, um die Paläohydrologie und den Schmelzwasserabfluss des Laurentidischen Eisschildes zu rekonstruieren. Das Schmelzwasserereignis der Jüngeren Dryas war hier von besonderem Interesse.

Die erste Studie bietet einen Einblick in deglaziale bis holozäne Schwankungen der Meereis- und Oberflächenwassereigenschaften in der Beaufortsee. Diese Region war während des Übergangs vom Deglazial zum frühen Holozän (~14-8 kyr BP) nahezu eisfrei und durch variable Ozeanoberflächentemperaturen gekennzeichnet. Während des mittleren bis späten Holozäns (~8-0 kyr BP) entwickelte sich eine saisonale Meereisdecke mit Ozeanoberflächentemperaturen unter 0 °C. Wir kommen zu der Erkenntnis, basierend auf spezifischen Biomarkern („HBI-III“) als Indikator für die Marginale Ice Zone (MIZ), dass die Kernlokation vor ca. 5.6 kyr in der Nähe einer Winter-MIZ und vor ca. 3.5 kyr in der Nähe einer Sommer-MIZ gelegen haben muss. Die Veränderungen im Meereis wurden höchstwahrscheinlich durch Veränderungen der Sonneneinstrahlung verursacht. Zudem wurden an dieser Kernlokation zwei Ereignisse mit hohem Sedimentfluss um ca. 13 bzw. ca. 11 kyr BP dokumentiert. Das erste Ereignis wurde auf das Schmelzwasserereignis der Jüngeren Dryas zurückgeführt, während das zweite Ereignis wahrscheinlich in Zusammenhang mit Küstenerosion, ausgelöst durch einen raschen Meeresspiegelanstieg, stand.

Die zweite Studie befasst sich mit der Beziehung zwischen dem Rückzug des Eisschildes und der Mobilisierung von altem terrestrischen, organischen Kohlenstoff. Radiokarbon-Analysen von organischem Material an dem Kern ARA04C/37 liefern, in Verbindung mit mehreren Proxies für die thermische Reifung, Beweise für verstärkte alte terrestrische Kohlenstoffflüsse zwischen 14.5-10 kyr BP. Während dieses Zeitraums führte der Rückzug des Laurentidischen Eisschildes zur Exhumierung, Freilegung und Oxidation von petrogenem, organischen Kohlenstoff aus dem anstehenden Gestein. Außerdem hat die Verringerung des Eisvolumens zu einem raschen Meeresspiegelanstieg geführt. Die damit einhergehende Küstenerosion hat wiederum die Remobilisierung von im Permafrostboden gebundenem Kohlenstoff um ca. 14 und 11 kyr BP verursacht. Abschätzungen der Kohlenstofffreisetzung beider Prozesse deuten darauf hin, dass der durch orbitalen Antrieb bedingte Rückzug des Eisschildes eine wichtige Rolle im Beitrag zum terrestrischen organischen Kohlenstoff während des deglazialen CO_2-Anstieges gespielt hat.

In der dritten Studie wurden paläohydrologische Veränderungen in der kanadischen Arktis durch Wasserstoffisotopenanalysen, ebenfalls anhand des Sedimentkerns ARA04C/37, rekonstruiert. Während des Deglazials (~14-8 kyr BP) wurde die Hydrologie in der kanadischen Beaufortsee weitgehend durch den Schmelzwasserabfluss des Laurentidischen Eisschildes beeinflusst. So fand zu Beginn der Jüngeren Dryas (ca. 13 kyr BP) eine extrem starke Reduzierung des Salzgehaltes auf ca. 24 PSU statt. Sowohl terrigene als auch marine Biomarker weisen starke Süßwasser-Signale auf. Dies bestätigt, dass der Mackenzie River einer der größten Auslässe während der Schmelzwasserereignisse der Jüngeren Dryas gewesen sein muss. Während des mittleren bis späten Holozäns (~8-0 kyr BP) stieg der Salzgehalt an der Ozeanoberfläche an, was wahrscheinlich auf einen geringeren Abfluss des Mackenzie Rivers zurückzuführen ist und auf ein trockeneres Klima im Einzugsgebiet hindeutet.

Zusammenfassend lässt sich sagen, dass unsere Studie über drei wichtige Komponenten des Klimasystems in der kanadischen Arktis (Meereis, alte terrestrische organische Kohlenstoffspeicher und das Schmelzwasser des Laurentidischen Eisschildes) neue Beweise über die Reaktionen einzelner arktischer Komponenten auf externe Einflüsse und/oder nachfolgende interne Wechselwirkungen liefert. Die neuen Daten werden dazu beitragen, die natürliche Variabilität des deglazialen Klimasystems besser zu verstehen.

Acknowledgement

First, I would like to thank my supervisor Prof. Dr. Ruediger Stein. Thank you so much for offering me the opportunity to work on this PhD project. I'm very lucky to have had you for the last four years. Thank you for your mentorship, and I learned a lot from you during my PhD study, not only the knowledge but also being a scientist. Besides, thank you for your patience, strong scientific support, and encouragement all the time. These helped me through a lot of moments of confusion and frustration.

Many thanks to Prof. Dr. Ralph Schneider for reviewing my thesis.

Special thanks to Dr. Kirsten Fahl. Thank you for controlling my data quality in the laboratory. You are always there when I had questions or problems. Thank you for taking care of me all the time, and you always make me feel warm working in the group.

I would like to thank Prof. Dr. Gesine Mollenhaur. Thank you for being my committee member and for offering me the opportunity to conduct laboratory work in your group. Besides, thanks for your advice and help with my manuscript. You are always available to answer my questions and to give me good suggestions.

Walter Luttmer, thank you for your guidance in the laboratory. You know everything in the lab and it is wise to discuss with you the lab work. I can always learn something new from you outside of the lab and it is always of pleasure to talk to you. Thanks also to Jens Hefter, Torben Gentz, Elizabeth Bonk, Maylin Malter, Susanne Wiebe, and Valea Schumacher for your technique support.

Thanks to all co-authors for your contributions to the manuscripts and this thesis.

Great acknowledgment to all my colleagues at AWI. Thanks to our group members Dr. Henriette Kolling, Dr. Anne Kremer, Dr. Nicole Syring, Jeetendra Saini, and Defang You. Thanks also to Ling Liu, Dr. Elena Vorrath, Dr. Shuzhuang Wu, Kevin Küssner, Nele Lamping, Julia Hagemann, Wenig-si Chao, and Vincent Rigalleau. Special thanks to Dr. Hendrik Grotheer and Dr. Vera Meyer.

Finally, I would like to thank my parents and all my best friends for your love and support. Thanks to Dr. Meng Yu and Dr. Bingbing Wei, you always give me a hand when I had hard times. I'm also very glad to meet all my friends in Bremerhaven.

1. Introduction

1.1 preamble

The Arctic region plays a crucial role in the global climate system due to its climate-sensitive components. The most unique and prominent features in this region are the Arctic sea-ice cover and widely distributed permafrost in the terrestrial surface around the Arctic Ocean. Other components include the polar ice sheets, glaciers, and huge river discharge.

Under global warming, the Arctic temperature is increasing at more than double the global average (Notz and Stroeve, 2016). As a consequence, a number of the climate components in the polar region have responded to the warming. For instance, the sea-ice extent and thickness are decreasing at a high rate, and projections suggest that the Arctic Ocean will become summer ice-free by the end of this century (Notz and Stroeve, 2016). Besides, the Arctic Amplification of air temperature has increased the permafrost temperature by 0.29±0.12 °C between 2007-2016 (Biskaborn et al., 2019). Under strong Arctic warming, permafrost thawing will result in cumulated CO_2 release of 42-141 PgC and 157-313 PgC in years 2100 and 2300 (Schneider Von Deimling et al., 2015). Furthermore, the Arctic glacier as a whole is losing mass at a rate of –213±29 Gt yr^{-1}, a sea-level contribution of 0.59±0.08 mm yr^{-1} (cf., Meredith et al., 2019).

These responses of the climate components will further act on the global climate system and shape the physical, ecological, social, cultural, and political conditions of human activities. By far, most of the changes are observed during the last few decades, which are not long enough for us to comprehensively decipher the responses and feedbacks of these components. In this context, reconstructions of pre-industrial records will help us better understand their roles and improve our future predictions.

1.2 Modern Arctic physiography and oceanography

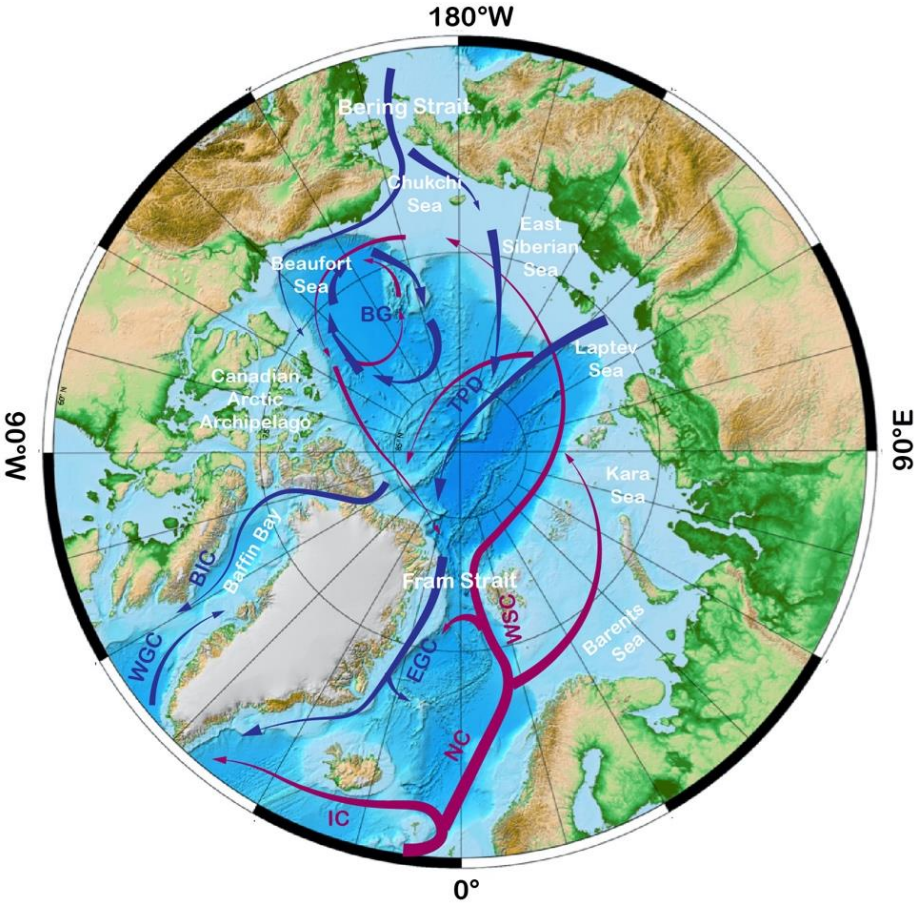

Figure 1.1: Map of the Arctic Ocean and the modern surface circulation. Warm Atlantic waters are indicated in red lines, including the Irminger Current (IC), Norwegian Current (NC), and the West Spitsbergen Current (WSC). Blue lines represent the circulation of polar water, including the Beaufort Gyre (BG), Transpolar Drift (TPD), Baffin Island Current (BIC), West Greenland Current (WGC), and East Greenland Current (EGC). Figure has been modified after (Macdonald et al., 2004), and the bathymetry is based on ETOPO1 (Amante and Eakins, 2009).

The Arctic Ocean is the northernmost and coldest of the all-encompassing world oceans. It is surrounded by the American and Eurasian continents, spanning between ~70-90°N on the Amerasian side and ~65-90°N on the Eurasian side (Fig. 1.1). The broad and shallow shelves extended from the continents comprise the Barents Sea, Kara Sea, Laptev Sea, East Siberian Sea, Chukchi Sea, Beaufort Sea, and the adjacent seas in the Hudson Bay and Baffin Bay (Fig. 1.1). These shallow regions cover ~52.7% of the total area of the Arctic Ocean (Stein and Macdonald, 2004). The Lomonosov Ridge divides the deep Arctic Ocean Basin into the Amerasian Basin and the Eurasian Basin. In the Amerasian Basin, the Alpha-Mendeleev Ridge subdivides the basin into the Canada Basin and Makarov Basin, whereas in the Eurasian Basin, the Gakkel Ridge subdivided it into the Amundsen Basin and Nansen Basin (Fig. 1.2).

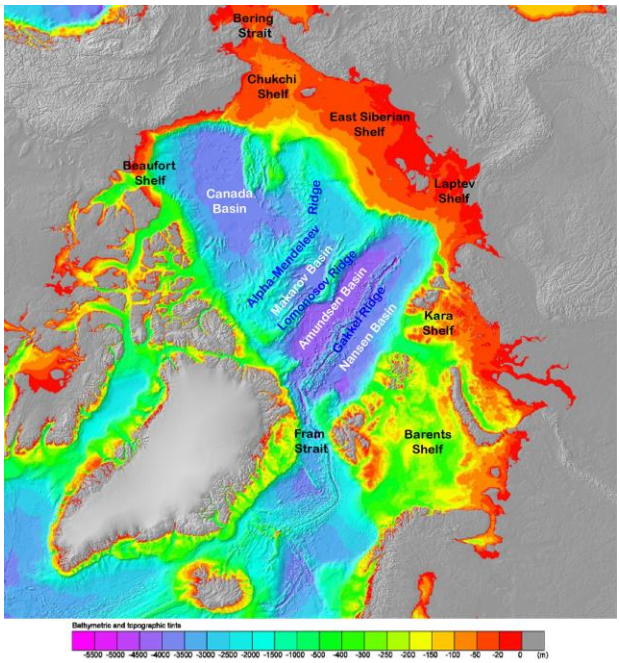

Figure 1.2: Bathymetry map of the Arctic Ocean. Submarine ridges and major basins are shown in the map (figure source: Syring, 2020, based on bathymetry data from Jakobsson et al., 2012).

The broad and deep Fram Strait, as well as the narrow and shallow Bering Strait, are the major gateways for the Arctic Ocean exchanging water masses with other oceans (Fig. 1.1 and Fig. 1.2). The northward inflow of the warm Atlantic Water through Fram Strait is a major carrier of heat towards the Arctic Ocean, which strongly influences the Arctic sea-ice distribution and stabilizes the stratification by supplying salt to the intermediate and bottom waters of the Arctic Ocean (Schauer et al., 2004; Spielhagen et al., 2011). Low-salinity Pacific Water enters the Arctic Ocean through Bering Strait, half of which travels northwest through Hope Valley while the other half travels along the Alaskan coast (Fig. 1.1; Winsor and Chapman, 2004).

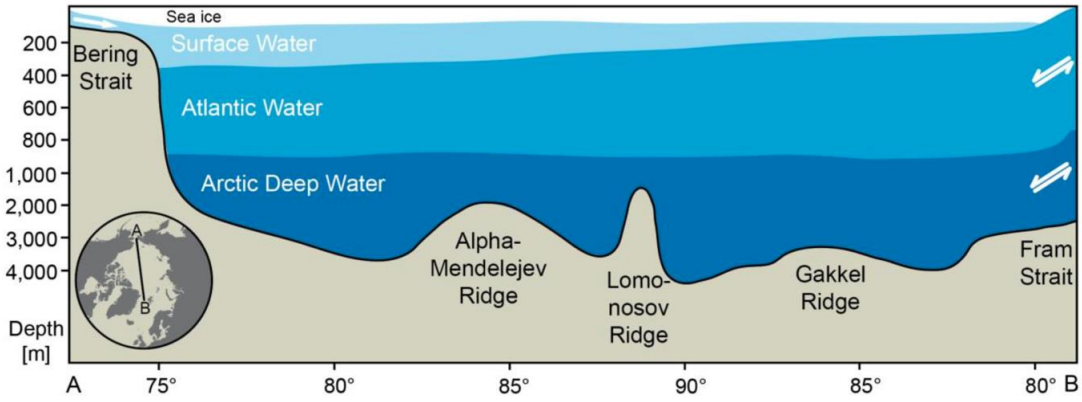

Figure 1.3: Hydrographic structure of the Arctic Ocean water masses, showing the transect from the Bering Strait towards the Fram Strait (figure source: Kremer, 2018, modified from Macdonald et al., 2004). White arrows indicate the exchange of water masses in Fram Strait with adjacent oceans.

The hydrographic structure of the Arctic water is composed of surface water, (Atlantic) intermediate water, and Arctic deep water (Fig. 1.3). The surface water (0-200 m) is of low salinity, and the sea surface temperature (SST) stays persistently around the freezing point due to the weak intensity of solar radiation. The surface layer has sources of less-saline waters from the Pacific Water, precipitation, and the Arctic river runoff which account for over 10% of the global runoff (Carmack et al., 2016; Serreze et al., 2006). The surface waters are steered by two wind-driven currents, i.e., the clockwise flowing Beaufort Gyre that locks the majority of freshwater in the Canada Basin and the Transpolar Drift that transports a large volume of freshwater and ice towards Fram Strait (Fig. 1.1). The (Atlantic) intermediate water (~200-800 m) is warm and saline (Fig. 1.3). The Atlantic Water enters the Arctic Ocean as the Norwegian Current, of which a substantial fraction flows into the Barents Sea while the remaining part flows along the continental margin as the West Spitsbergen Current. The currents merge in the outer shelf of the Kara Sea and continue in intermediate depth towards the Siberian shelf regions (Fig. 1.1). The Arctic deep water (>800 m) is characterized by high salinity due to lateral exchange with the Nordic Seas and brine formation on the Arctic shelves resulting in dense saline water into the deep Arctic Ocean (Fig. 1.3; Rudels, 2015).

Figure 1.4: Map of the pan-Arctic watershed. The Arctic great rivers comprise Ob', Yenisey, Lena, Kolyma, Yukon, and Mackenzie River (source: ArcticGRO; *https://arcticgreatrivers.org*).

The pan-Arctic watershed consists of many rivers among which six Arctic great rivers have basin areas exceeding 500 000 km^2, i.e., Ob', Yenisey, Lena, Kolyma, Yukon, and Mackenzie (Fig. 1.4). These great rivers supply substantial freshwater to the Arctic Ocean, which influence the stratification, sea-ice formation, melting,

and coastal fast-ice formation (Aagaard and Carmack, 1989; Bareiss and Görgen, 2005; Divine et al., 2004; Park et al., 2020; Proshutinsky et al., 2015). Besides, the Arctic great rivers transport a great amount of nutrients and terrestrial organic carbon (OC) in dissolved and particulate forms to the Arctic Ocean, stimulating the primary productivity in the marginal seas (Retamal et al., 2008) and regulating the Arctic Ocean carbon budget (Stein and Macdonald, 2004).

1.3 Sea ice in the Arctic Ocean and its role in climate system

Sea ice in the Arctic Ocean is characterized by strong seasonal variations. Arctic sea ice reached its annual maximum extent in late winter (15.05×10^6 km^2 in March 2020) (Fig. 1.5). During this time, it covered most parts of the Arctic Ocean and extended further south to the Okhotsk Sea in the Pacific Ocean and Hudson Bay in the Atlantic Ocean (Fig. 1.5). Sea ice retreated during the spring and summer, and reached its annual minimum extent in late summer (3.74×10^6 km^2 in September 2020), exposing most of the marginal seas in the Arctic Ocean (Fig. 1.5).

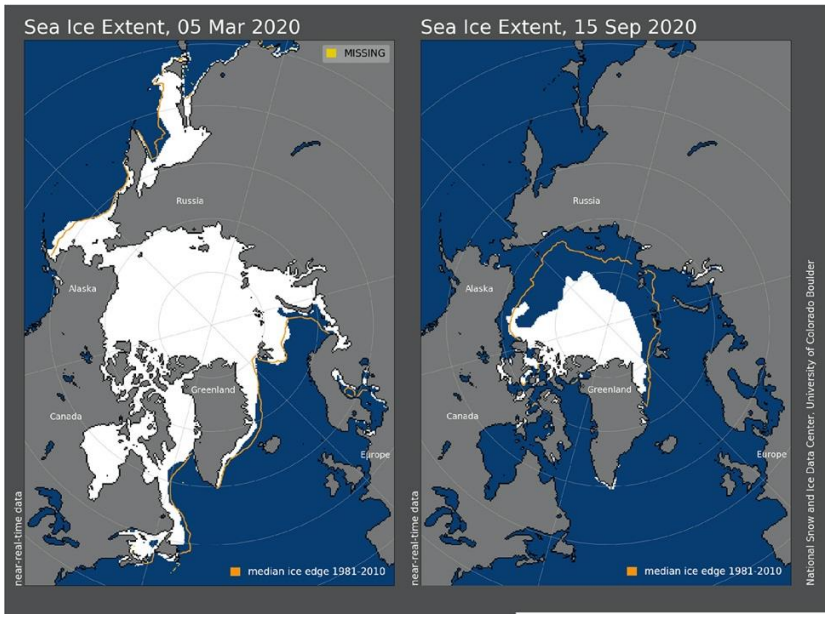

Figure 1.5: Arctic sea-ice extent for March 2020 and September 2020. Orange lines indicate the median ice edge between 1981-2010 (source: *https://nsidc.org/*).

The sea-ice extent has declined throughout the last decades (Comiso et al., 2017; Meredith et al., 2019; Stroeve and Notz, 2018). The minimum sea-ice extent has reduced with an areal reduction of –12.8% per decade compared to the mean value of 1981-2010 (Onarheim et al., 2018) (Fig. 1.6), dominantly observed in the Beaufort Sea, Chukchi Sea, East Siberian Sea, Laptev Sea, and the Kara Sea (Fig. 1.5 and 1.7). In winter, the sea-ice loss has a reduction of –2.7% per decade, and mainly occurred in the Barents Sea (Fig. 1.7) (Onarheim

et al., 2018; Onarheim and Årthun, 2017). The historical minimum sea-ice extent was observed in September 2012, and sea-ice extent in recent years is reaching close to this record minima. As the Arctic Ocean temperature is continuously going up, projections suggest that the Arctic Ocean may become summer ice-free by the end of this century (Fig. 1.7).

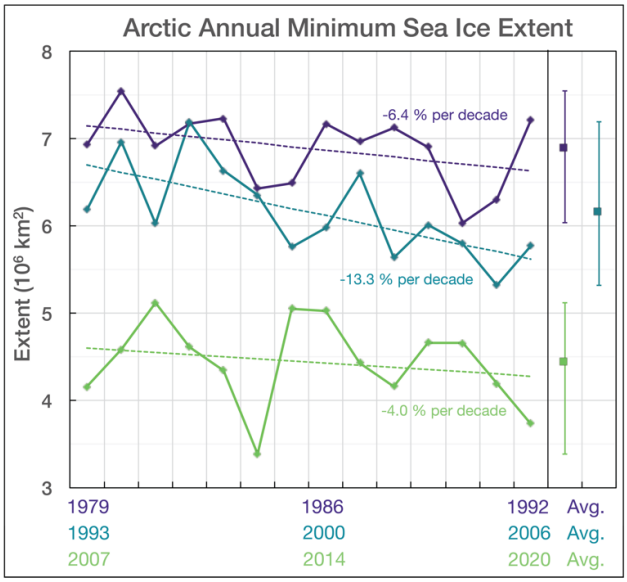

Figure 1.6: Arctic annual minimum sea-ice extent and linear trends for three 14-year periods. Trend percent values are relative to the average minimum extent between 1981-2010. The average and range of the minimum extent for each period are given on the right (source: *https://nsidc.org/*).

Sea ice, due to its light surface, reflects 50%-70% of the incoming energy (NSIDC, 2020: http://nsidc.org) and thus directly modulates the climate. Under anthropogenic warming, the sea-ice reduction tends to decrease the albedo and in return, amplifies Arctic warming. It has been identified that the "Arctic Amplification" (warming in the Arctic is faster than the rest of the world) exists in regions of large sea-ice loss (Dai et al., 2019; Kim et al., 2019). In addition, sea ice directly regulates the exchanges of heat, moisture, and gas between the ocean and the atmosphere. Less sea ice allows more transport of heat and moisture from the ocean to land and may further cause greenhouse gas release from the inland permafrost thawing (Vaks et al., 2020). Indirectly, the decrease of sea ice is able to trigger anomalous surface heat and freshwater fluxes, resulting in a positive buoyancy anomaly. The export of ice/freshwater into the Atlantic Ocean may weaken the Atlantic Meridional Overturning Circulation (AMOC) and its poleward heat transport, affecting global climate change (Sévellec et al., 2017).

Sea ice also influences the primary productivity in the (sub-)Arctic Ocean. Melting of sea ice is involved in water column stratification and nutrient release. It forms a stable and nutrient-rich environment above the pycnocline, that is favorable for phytoplankton blooms (Ackley and Sullivan, 1994; Mayot et al., 2020; Niebauer and Alexander, 1985; Smith. and Nelson, 1985; Strass and Nöthig, 1996). Besides, the sea-ice

thickness exerts control on light penetration and also influences the primary productivity (Belchansky and Douglas, 2002; Cremer, 1999).

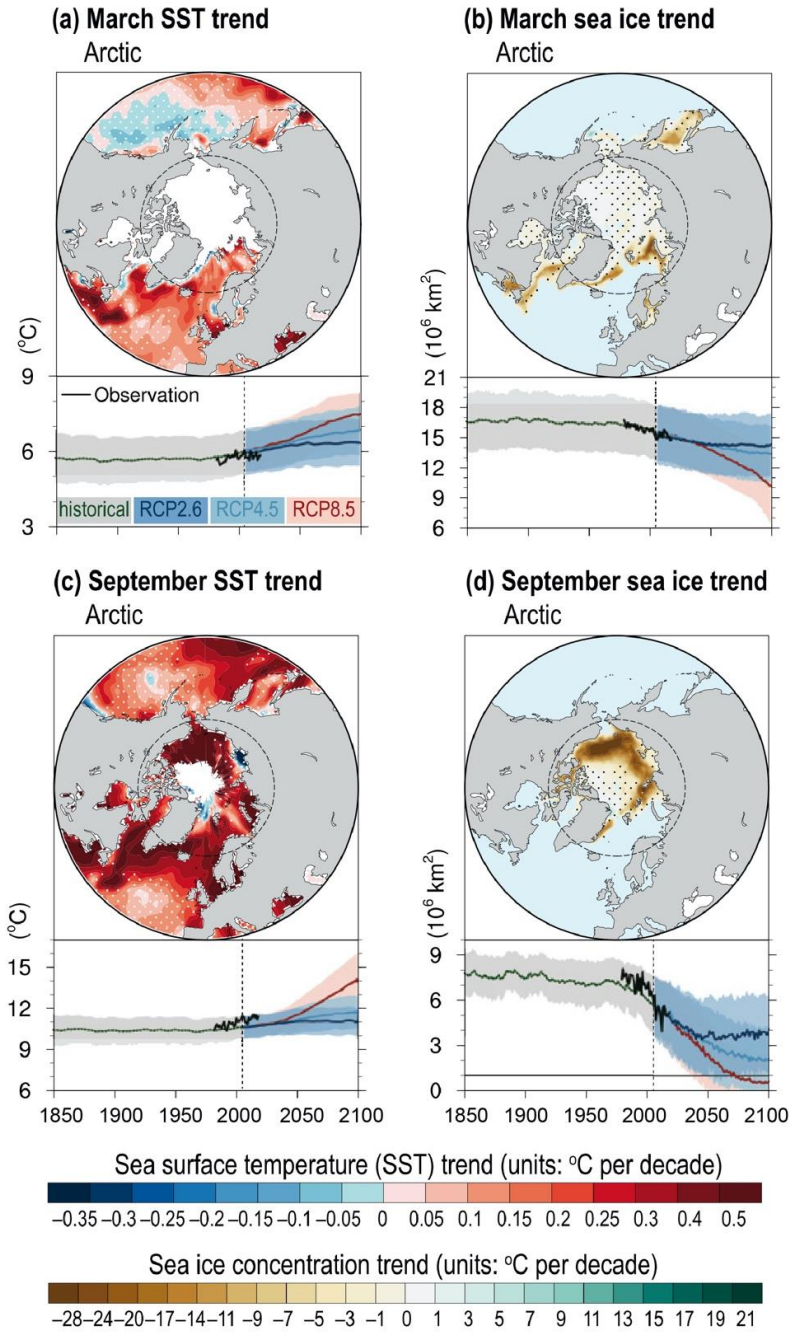

Figure 1.7: Maps of linear trends of SST and sea-ice concentration in the Arctic Ocean. Panels (**a**) and (**c**) indicate March SST trend and September SST trend for 1982-2017, while panels (**b**) and (**d**) show the March and September sea-ice trends respectively. Beneath the maps, black curves indicate observations, while other curves represent the Coupled Model Intercomparison Project Phase 5 (CMIP5) historical simulation and Representative Concentration Pathway (RCP)2.6, RCP4.5, and RCP8.5 projections (source: Meredith et al., 2019).

1.4 Terrestrial organic carbon in high latitude and its role in the carbon cycle

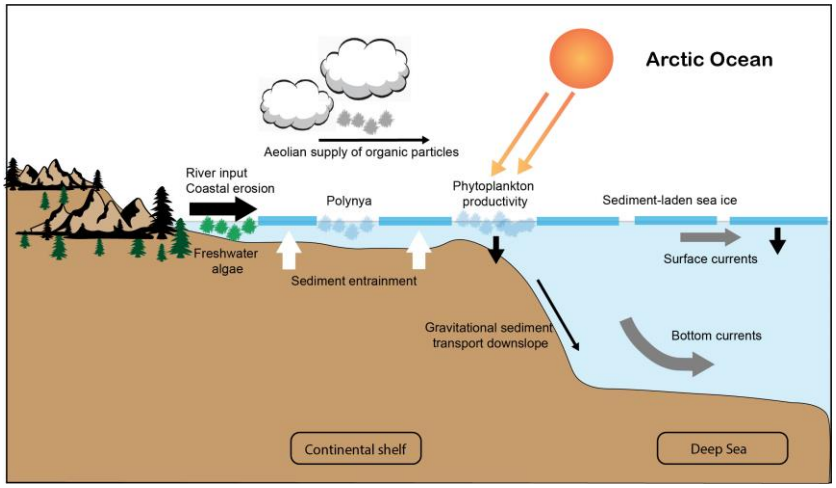

Figure 1.8: Schematic diagram for organic carbon cycle in the Arctic Region (modified after Stein and Macdonald, 2004).

Organic carbon cycle in the land-ocean system involves marine OC and terrestrial OC. In the Arctic regions, there are multiple pathways to transport terrestrial OC to the Arctic Ocean, including river input, coastal erosion, entrainment into sea ice and sea-ice transport, and aeolian transport (cf., Stein and Macdonald, 2004) (Fig. 1.8). Hence, terrestrial OC plays an important role in the carbon cycle in the Arctic regions.

Terrestrial OC, according to its carbon reservoirs (such as the biomass, soil, and bedrock), can be classified into two categories, i.e., the rock-derived organic carbon (OC_{petro}, defined as OC derived from rocks, greater than ~60,000 years old) (Copard et al., 2007; Drenzek et al., 2009; Hilton and West, 2020) and the terrestrial biospheric carbon ($OC_{terr\text{-}bio}$) from a variety of organisms, including riverine and lacustrine primary production, soils, and plants. Among these reservoirs, permafrost soil is a unique carbon reservoir of $OC_{terr\text{-}bio}$ in high latitude.

1.4.1 Permafrost carbon

Permafrost has been defined as ground (e.g., soil and rock) below 0°C for at least two consecutive years, and it occupies approximately a quarter of the landmass in the Northern Hemisphere (~25×10^6 km^2; Zhang et al., 2003) (Fig. 1.9). According to the area underlain by permafrost, permafrost zones can be further defined as continuous permafrost (90-100%), discontinuous permafrost (50-90%), sporadic permafrost (10-50%), and isolated patches (0-10%).

The permafrost soil today contains ~60% of the world's soil carbon and exceeds the modern carbon inventory in the atmosphere by a factor of about two (1,400 PgC; Hugelius et al., 2014). Because the permafrost carbon has been freeze-locked and protected from biodegradation, it is disconnected from the active carbon cycling on a millennial scale. Once permafrost thaws, the permafrost carbon becomes highly bioavailable (Tanski et

al., 2019; Vonk et al., 2012) and carbon release from such processes may have a strong impact on the global climate system.

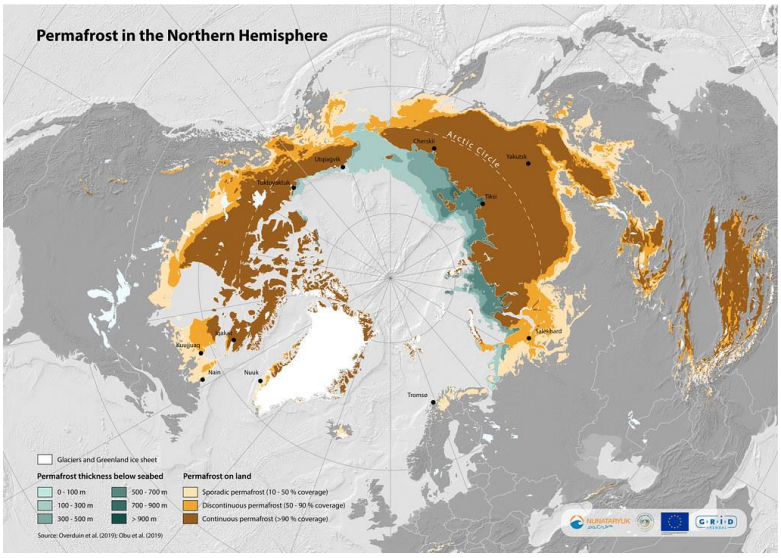

Figure 1.9: Map of permafrost distribution, showing terrestrial and submarine permafrost in the Northern Hemisphere (source: GRID-Arendal/Nunataryuk; *https://www.grida.no/resources/13519*).

Under global warming, permafrost temperature globally increased by 0.3°C in the last decade (Biskaborn et al., 2019). This led to deepening of the active layer that is seasonally thawed. Observation-based modeling suggests that the newly thawed permafrost (deepening of active layer) may result in significant carbon emission in the warming future (Schneider Von Deimling et al., 2015). In addition to the gradual thaw, model simulation suggests that the abrupt thaw through collapsing ground, landslides, and rapid erosion from 2.5 × 10^6 km^2 permafrost zone may have similar climate feedback with gradual permafrost thaw from 18 × 10^6 km^2 regions (Turetsky et al., 2020), highlighting the potential impacts from the abrupt thaw.

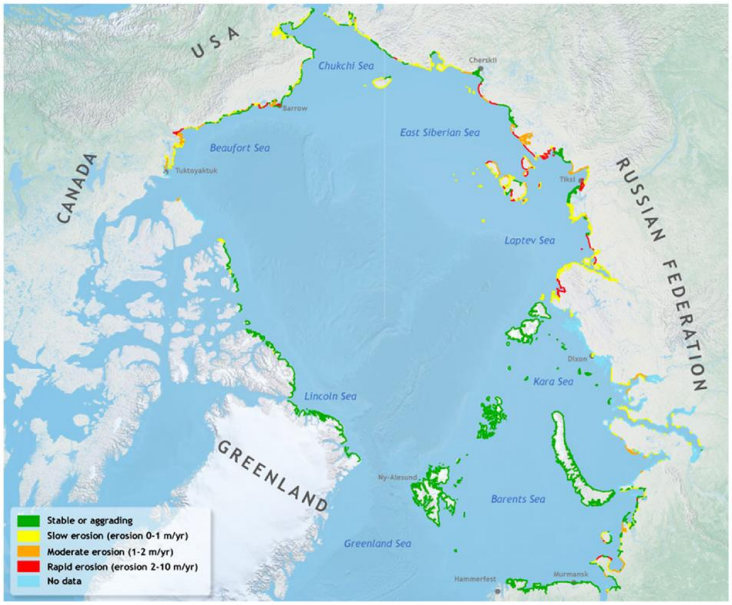

Figure 1.10: Circum-Arctic map of coastal erosion rates (source: Lantuit et al., 2012).

Coastal erosion is one of the processes of abrupt permafrost thaw. The Arctic coastline today has an average erosion rate of 0.5 m $year^{-1}$, and high erosion rates are observed in the Laptev Sea, the East Siberian Sea, and the Beaufort Sea (Fig. 1.10; Lantuit et al., 2012). The process of coastal erosion is controlled by multiple factors, including environmental conditions in the adjacent ocean. High water level is a prerequisite for coastal erosion. As at high water levels, the sea-ice condition, rate of sea-level rise, water temperature, and nearshore wavefield exert primary control on the rate of coastal erosion (Barnhart et al., 2014; Overeem et al., 2011).

1.4.2 Petrogenic organic carbon

OC_{petro} (also referred to as fossil organic carbon) is the OC stored in the rocks (Copard et al., 2007; Hilton and West, 2020). In settings of uplift, the sedimentary rocks outcrop at the continental surface and deliver OC_{petro} to modern environments by erosion and weathering. The Earth's surface (the first meter) holds a stock of OC_{petro} of ~1.1×10^6 MtC (Copard et al., 2007). The global distribution and storage of OC_{petro} have been estimated by Copard et al. (2007) and are shown in Figure 1.11.

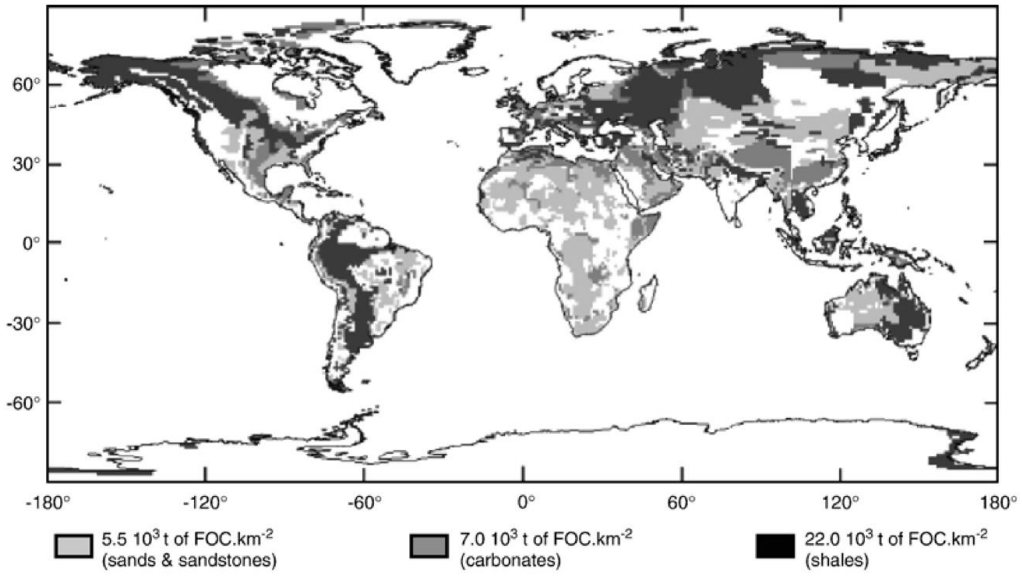

Figure 1.11: Storage and distribution of petrogenic/fossil OC in the first meter of sedimentary rock. Values for carbon storage are estimated using the average TOC for respective rock types (source: Copard et al., 2007).

Exhumation of OC_{petro} may lead to oxidation and CO_2 release from the ancient carbon reservoir. OC_{petro} oxidative weathering happens in the upper centimeters to meters of the Earth's surface, interacting with O_2 from air or waters enriched with oxygen (Keller and Bacon, 1998; Petsch et al., 2000; Soulet et al., 2018). Today, ~40-100 MtC of OC_{petro} are oxidized each year (Hilton and West, 2020). Because the carbon flux from OC_{petro} oxidative weathering is relatively small and it needs 10^4-10^6 years to replace the entire carbon mass of the oceans, atmosphere, and biosphere (Fig. 1.12; Hilton and West, 2020), this process thus has been regarded

to play a role in the geological carbon cycle. For instance, oxidation of remobilized fossil organic carbon (10^2-10^4 PgC) has been proposed to sustain global warming and a global carbon isotope excursion during the Palaeocene-Eocene Thermal Maximum body (70-100 kyr) (Lyons et al., 2019).

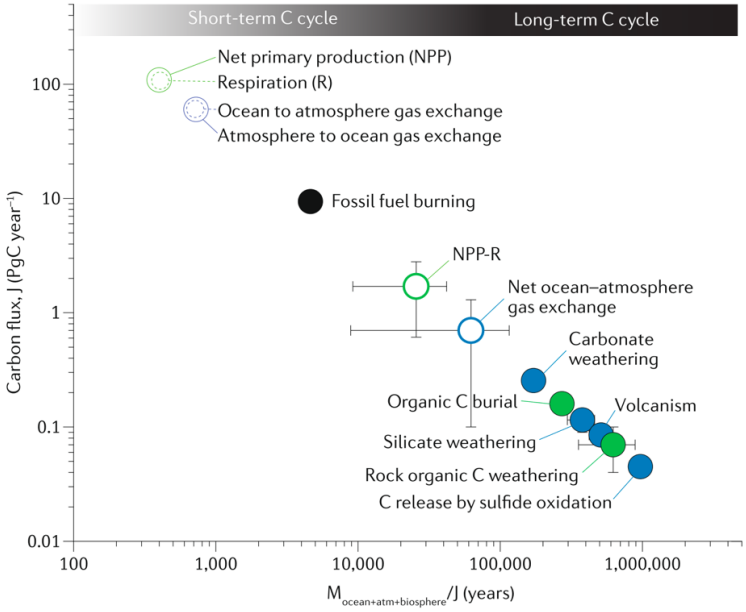

Figure 1.12: Estimate of pre-industrial carbon fluxes and the timescale for each flux to replace the entire carbon mass of the oceans, atmosphere, and biosphere (in total 43,540±550 PgC). Rapid carbon release from fossil-fuel burning is highlighted as a black symbol (source: Hilton and West, 2020).

Studies to measure the flux of OC_{petro} oxidative weathering identified that rock erosion rate exerts first-order control on OC_{petro} oxidation rate, and thus the OC_{petro} oxidation is proposed as a supply-limited process (Hilton et al., 2014; Hilton and West, 2020; Horan et al., 2017). High OC_{petro} supply is found in mountain regions whereas extremely high OC_{petro} supply has been observed in glaciated mountain regions (Cui et al., 2016; Horan et al., 2017). This can be attributed to the fact that glacial retreat and enhanced ice flux may increase the physical erosion of bedrock by glacial erosion/abrasion, supplying rock flour with more effective surface areas. Consequently, the OC_{petro} oxidation rate is further enhanced in glacier-dominated regions even at the same physical erosion rate (Horan et al., 2017).

Not all exhumed/eroded OC_{petro} can be oxidized. It is observed that ~10%-70% of the exhumed OC_{petro} in mountain regions is oxidized whereas the proportion is up to >90% in the floodplains of large tropical rivers (Bouchez et al., 2010; Hemingway et al., 2018; Hilton et al., 2014; Horan et al., 2017). The OC_{petro} re-buried in river sediments may indicate a chemically and physically resilient component. Alternatively, the OC_{petro} oxidation may be locally limited by other factors, e.g., temperature and O_2 (Hilton and West, 2020, and references therein).

1.5 Climate evolution since the last deglaciation

The climate history of Quaternary (2.6 Ma - present) is characterized by a distinctive feature of glacial-interglacial cycles (Batchelor et al., 2019; Ehlers and Gibbard, 2007; Svendsen et al., 2004). During the glacial (cold) periods, continental ice sheets advanced and covered much of the Northern Hemisphere, while during the interglacial (warm) periods, ice sheets drastically retreated. Alternation of glacial and interglacial periods coincides with the cyclic changes in Earth's orbit ("Milankovitch cycle") and thus it is proposed driven by orbital forcing, with frequencies of 100 kyr, 41 kyr, and 23 kyr.

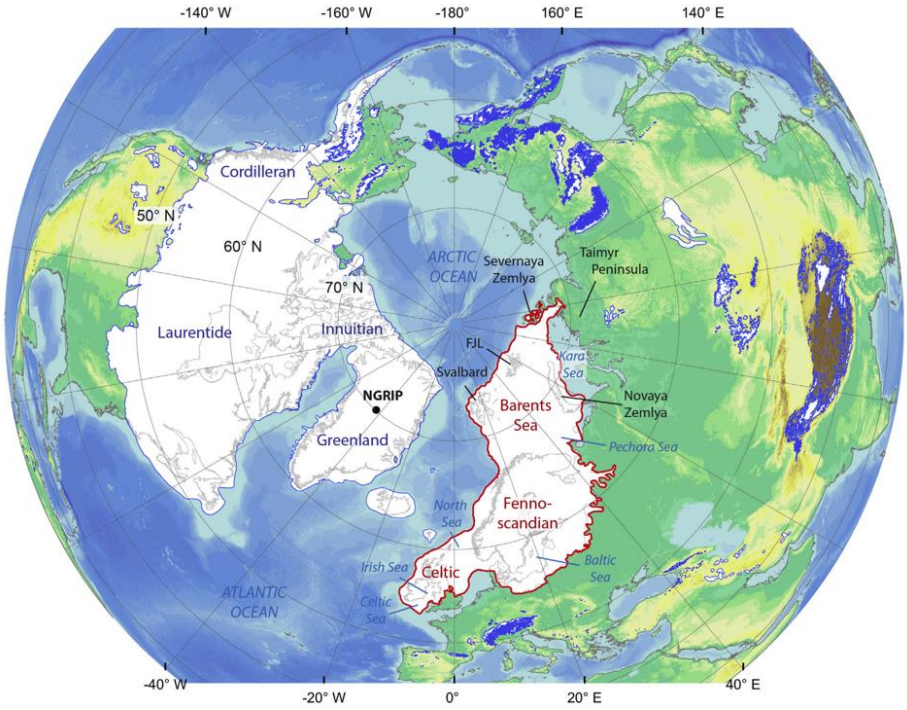

Figure 1.13: Map of maximum ice-sheet extent in the Northern Hemisphere during the LGM (source: Patton et al., 2016).

The last glacial period occurred from the end of the Eemian to the end of the Younger Dryas (YD) (115 kyr-11.7 kyr BP). Within this period, ice sheets reached the maximum position during 26.5-19 kyr BP (the Last Glacial Maximum, LGM) (Fig. 1.13) and the sea level fell by ~130 m (Clark et al., 2009). After the LGM, ice sheets started to retreat and the climate system underwent a dramatic transformation during the last deglaciation.

1.5.1 The last deglaciation

The ice-sheet retreat since the LGM has directly resulted in sea-level rise. During the major phase of deglaciation (~16.5-7 kyr BP), the total ice-volume equivalent sea-level (esl) increased by ~120 m (Fig. 1.14) (Lambeck et al., 2014). The sea-level rise also occurred in pulses in certain periods. The meltwater pulse 1a (MWP-1a) is one of the largest and most rapid events. It occurred at ca. 14.6 kyr BP and caused a sea-level rise

of ~20 m within 500 years (Lambeck et al., 2014). Recent model simulation suggests that meltwater from Antarctica and Scandinavia contributed 1.3 m and 4.6 m respectively, whereas the contribution from North America was 12.0 m (Lin et al., 2021). Another meltwater pulse (MWP-1b) has been reported at ca. 11.3 kyr BP, but its existence remains elusive (Bard et al., 2010). Nonetheless, an increased rate of sea-level rise has been observed within the time window (Lambeck et al., 2014).

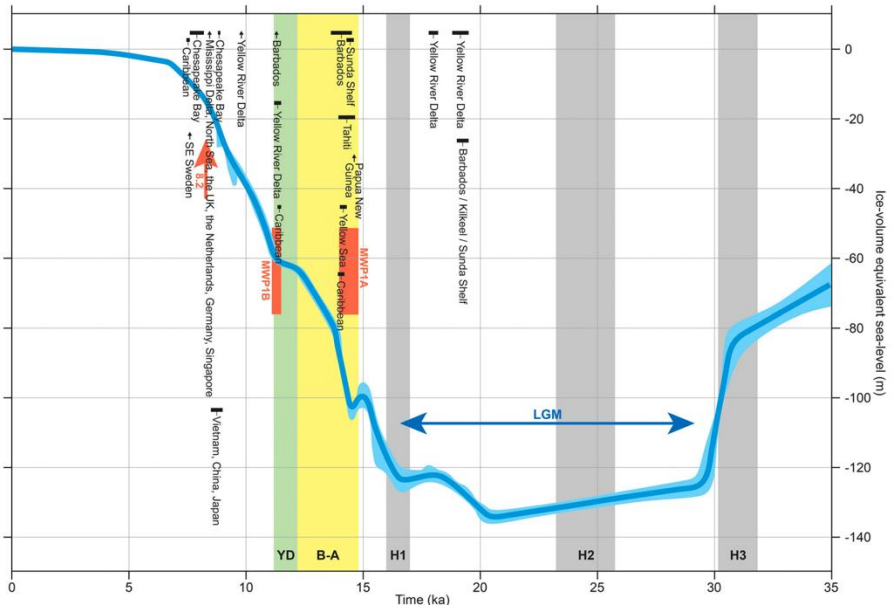

Figure 1.14: Ice-volume equivalent sea-level (m) since the Lateglacial times, data are from Lambeck et al. (2014). Major climate events are indicated, including the Heinrich events H1-3, Bølling–Allerød (B/A), and Younger Dryas (YD) (source: Harrison et al., 2019).

Abrupt climate changes occurred during the last deglaciation. According to the $\delta^{18}O$ record of Greenland ice core (North Greenland Ice Core Project members, 2004), the Heinrich stadial 1 (HS1) occurred in the early deglaciation (~18-15.6 kyr BP), followed by the Bølling–Allerød (B/A) interstadial (~14.6-13.0 kyr BP). At the termination of B/A, another abrupt cooling event – the Younger Dryas (YD) stadial – existed between ~13.0-11.7 kyr BP (Fig. 1.15). The cause of the HS1 event has been related to iceberg calving (Bond and Lotti, 1995). Explanation of the YD cooling has been mainly attributed to a catastrophic meltwater outburst from proglacial Lake Agassiz, which may have caused a collapse of the AMOC and a reduction of the associated northward heat transport (Broecker et al., 1985). However, such a single process cannot support a full collapse of the AMOC during the YD (Barker et al., 2010), and thus multiple explanations of the YD cooling have been offered, e.g., extraterrestrial impact, a large solar minimum, and a shift in atmospheric circulation (Firestone et al., 2007; Renssen et al., 2000; Wunsch, 2006). The meltwater outburst as a main/most probable trigger for YD cooling, its pathway remains unresolved, and there is a debate whether the freshwater discharge drained first into the Arctic Ocean and then to the Atlantic Ocean or whether it drained directly into the Atlantic Ocean (Broecker et al., 1989; Keigwin et al., 2018; Leydet et al., 2018; Peltier et al., 2006).

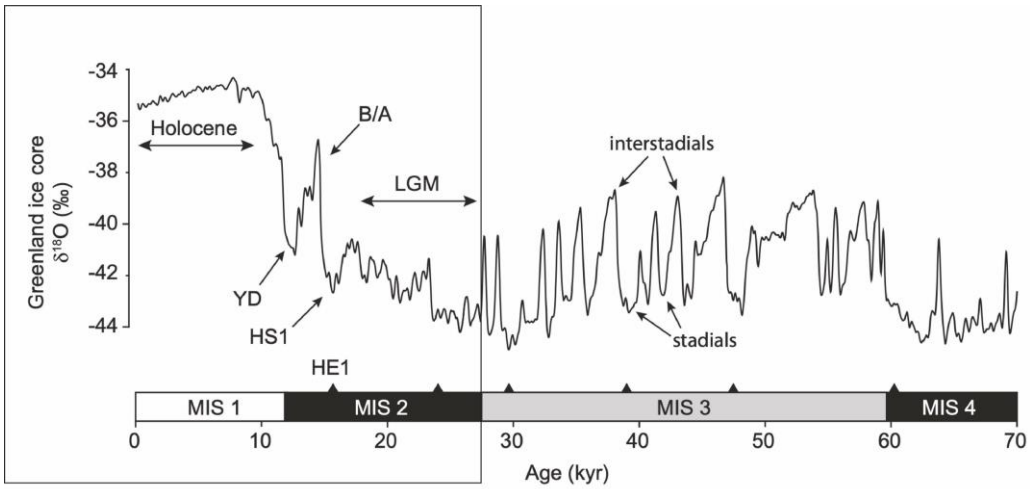

Figure 1.15: Millennial-scale climate variability documented by $\delta^{18}O$ record of the Greenland ice core (North Greenland Ice Core Project members, 2004) (source: Barker and Knorr, 2021).

Atmospheric CO_2 has increased by ~75 ppm during the last deglaciation, with an onset at ca. 17.5 kyr BP (Monnin et al., 2001). At the same time, radiocarbon content ($\Delta^{14}C$) and stable carbon isotope values ($\delta^{13}C$) of CO_2 declined (Bauska et al., 2016; Reimer et al., 2020). Because of the close correlation between CO_2 concentration and Antarctic temperature, it is consensus that oceanic carbon release from the Southern Ocean acted as a major contributor to the deglacial atmospheric CO_2 rise (Anderson and Burckle, 2009; Monnin et al., 2001). However, the oceanic CO_2 release alone cannot account for the full amplitude of CO_2 rise or the $\delta^{13}C$ and $\Delta^{14}C$ anomalies, thus more processes have been invoked to explain the CO_2 variations, e.g., oceanic biological pump and oxidation of terrestrial OC (Bauska et al., 2016). More recently, multiple lines of evidence suggest that flooding of Arctic shelves may have contributed substantial permafrost carbon to the deglacial CO_2 rise (Köhler et al., 2014; Martens et al., 2020; Meyer et al., 2019; Winterfeld et al., 2018).

Greenhouse gas CH_4 also started to rise at ca. 17.5 kyr BP. A rapid increase occurred at about 14.7 kyr BP, followed by an abrupt decrease at about 12.9 kyr BP. The last rapid increase in CH_4 occurred at 11.7 kyr BP and then CH_4 concentrations sustained high during the Holocene (Marcott et al., 2014; Monnin et al., 2001). The rapid increases in CH_4 concentrations were synchronous with the abrupt climate changes in Northern Hemisphere, and have been related to carbon sources from the Northern Hemisphere (Marcott et al., 2014; Monnin et al., 2001). A recent study suggests that, instead of old carbon reservoirs, the contemporaneous CH_4 sources may have played a dominant role in these increases (Dyonisius et al., 2020).

1.5.2 The Holocene

The Holocene began at approximately 11.7 kyr BP, marked by a significant increase in stable oxygen isotope ($\delta^{18}O$) values in the Greenland ice core (Fig. 1.15) (North Greenland Ice Core Project members, 2004; Rasmussen et al., 2006). The Holocene is characterized by a warmer climate and weaker fluctuations in comparison to the last deglaciation. The Holocene can be generally subdivided into three periods. The early

Holocene (11.6-9 kyr BP) correlates with the “Preboreal” and the “Boreal” chronozones. The mid-Holocene (9-5 kyr BP) links to the “Atlantic” chronozone, whereas the late Holocene (5 kyr BP to pre-industrial times) coincides with the “Subboreal” and the “Subatlantic” chronozones (Fig. 1.16) (Nesje and Dahl, 1993; Wanner et al., 2008).

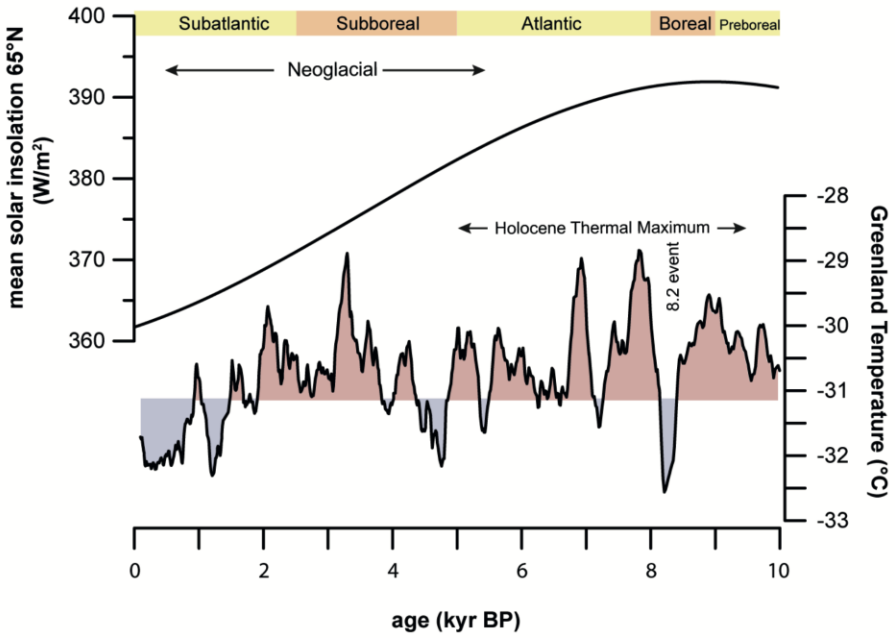

Figure 1.16: Holocene Greenland temperature and Northern Hemisphere solar insolation curve (figure source: Kolling, 2017; data from Alley et al., 2010 and Laskar et al., 2004).

The early Holocene was characterized by enhanced summer insolation with its maximum at around 9 kyr BP (Fig. 1.16) (Laskar et al., 2004). Synthesis of marine records has identified warmer conditions during the early Holocene exceeding the modern warmth (Marcott et al., 2013), which is known as the Holocene Thermal Maximum (HTM). However, climate models only simulated long-term warming from the early Holocene to the late Holocene, and the mismatch between proxy reconstructions and computational simulations makes the period a “Holocene temperature conundrum” (Liu et al., 2014). Recent research proposed to use a seasonal solution (seasonal bias in proxy reconstructions) to explain the discrepancy, and the study demonstrated that the global mean annual SST has increased steadily during the last 12 kyrs (Bova et al., 2021). Whether the discrepancy is indeed caused by seasonal bias in reconstructions or by the model bias needs more work to improve our understanding. The mid-Holocene climate was relatively warm but interrupted by a prominent cooling event at around 8.2 kyr BP (Fig. 1.16). During this time, a significant reduction in the AMOC has been observed and it has been related to an outburst of the proglacial Lake Agassiz-Ojibway in many studies (cf., Barber et al., 1999). Recently, a study based on Mg/Ca and oxygen isotope ratios of benthic foraminifera proposed that the strengthening of the Western Greenland Current has accelerated the Hudson Bay Ice Saddle collapse during this period, and it may have a much larger effect on the AMOC than the lake outburst (Lochte

et al., 2019). The late Holocene was characterized by decreased solar insolation (Fig. 1.16) as well as glacier advances in Greenland, Svalbard, and Scandinavia (Isaksson et al., 2005; Levy et al., 2017; Nesje et al., 2001; Svendsen and Mangerud, 1997; Werner, 1993). Therefore, this time frame is also referred to as the Neoglacial cooling period (Wanner et al., 2008).

1.6 Study area – the Canadian Beaufort Sea

Our study area is the Canadian Beaufort Sea (Fig. 1.17). The Beaufort shelf has a width of ~70-120 km in the American Beaufort Sea and a width of ~65-180 km east of the Mackenzie (shelf-break at ~80 m water depth) (Carmack et al., 2004). The surface water circulation in the Beaufort Sea is dominated by the wind-driven anticyclonic Beaufort Gyre (Fig. 1.17a), which drives the offshore currents westward and locks the majority of the Arctic Ocean's freshwater in the Canada Basin (Serreze et al., 2006). Another energetic feature in this region is the shelf-break current below a water depth of 50 m, transporting Pacific Water eastward along the slope (Fig. 1.17a) (Pickart, 2004).

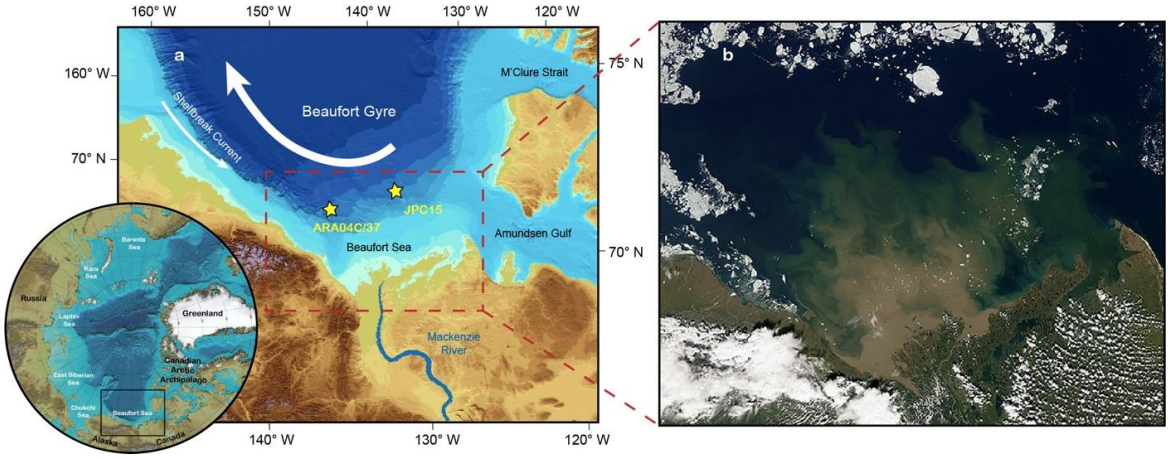

Figure 1.17: (**a**) Maps of the Canadian Beaufort Sea. The yellow star in panel (a) represents the location of the study sediment core ARA04C/37. (**b**) The Mackenzie River plume on July 5, 2012 (source: NASA/Goddard Space Flight Center; *https://visibleearth.nasa.gov*).

The Mackenzie River supplies substantial freshwater and sediments to the Beaufort Sea. It is the 4th largest Arctic river by annual water discharge (316 km^3 yr^{-1}) and the largest Arctic river in terms of sediment flux (124-128 Mt yr^{-1}) (Holmes et al., 2002; Stein and Macdonald, 2004). Sediments discharged from the Mackenzie River are dominated by silt and clay, forming a feature of plume off the Mackenzie River mouth (Fig. 1.17b). The highest sedimentation rates occur in the Mackenzie Trough (~40-320 cm kyr^{-1}) and the continental shelf and slope nearby (~100-200 cm kyr^{-1}) (Gamboa et al., 2017, and references therein).

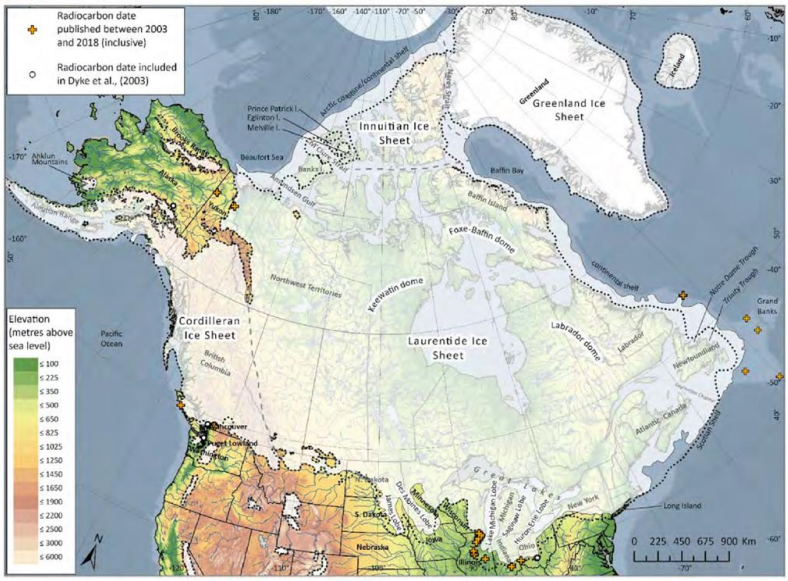

Figure 1.18: Map of maximum ice-sheet extent in North America and Greenland during the LGM (18 kyr ^{14}C). Black dashed line indicates the previous 18 kyr ^{14}C isochrone of Dyke et al. (2003). Note that the maximum ice-sheet extent was asynchronous in each region (source: Dalton et al., 2020).

During the LGM, the Laurentide Ice Sheet (LIS) has advanced and covered most of North America (Fig. 1.18) (Dalton et al., 2020). At that time, the LIS has reached the Rocky Mountains in the west and covered the entire region where the modern Mackenzie River basin is located in. The Mackenzie River drainage system has been established due to glacial erosion and became an outlet of meltwater since the late Wisconsinan (i.e., Marine Isotope Stage 2) (Duk-Rodkin and Hughes, 1994).

1.7 Approaches for paleoenvironmental reconstruction

In the Arctic Ocean, paleoenvironmental reconstruction are mainly based on micropaleontological, sedimentological, and geochemical proxies. For example, the foraminiferal assemblages, diatom assemblages, dinoflagellate cysts, and IRD are commonly used to reflect the past sea-ice conditions (cf., Pieńkowski et al., 2017; Scott et al., 2009; Weckström et al., 2013). The terrestrial biomarkers and bulk OC parameters, e.g., C/N ratio, lignin phenols, and Rock-Eval parameters are often used to indicate terrestrial OC input (cf., Copard et al., 2006; Martens et al., 2020; Syring et al., 2020b). In addition, the approach widely used to reconstruct hydrological changes in surface water in the Arctic Ocean is primarily based on the oxygen and stable carbon isotopic composition ($\delta^{18}O$ and $\delta^{13}C$) of planktic foraminifera (cf., Poore et al., 1999; Spielhagen et al., 2005; Stein et al., 1994a) and sediment proxies (cf., Not and Hillaire-Marcel, 2012).

In this current study, paleoenvironmental reconstructions are based on a number of biomarkers and multiple isotopes. They were analyzed to reconstruct the variabilities of different climate components in the Arctic region, and we give an introduction of the principal biomarkers and proxies used here for sea ice, primary

productivity, terrestrial OC, and freshwater discharge. Other bulk parameters and proxies are described in detail in chapter 2.

1.7.1 Sea ice and primary productivity

The sea-ice biomarker, mono-unsaturated highly branched isoprenoid (HBI) alkane with 25 carbon atoms (IP_{25} monoene; Fig. 1.19), has been first discovered by Belt et al. (2007) in their study from the Canadian Arctic. Producers of IP_{25} have been identified only in three (or four) sea-ice diatoms (i.e., *Pleurosigma stuxbergii var. rhomboides*, *Haslea kjellmanii*, *Haslea crucigeroides*, and/or *Haslea spicula*) and IP_{25} was absent in the dominant taxa (Brown et al., 2014). Hence, it shows the potential of being an ideal proxy for sea-ice reconstructions. In the Canadian Beaufort Sea, approximately 90% of the IP_{25} is accumulated during the ice-algal spring bloom, whereas sediment traps at the southern Lomonosov Ridge also show enhanced IP_{25} accumulation in summer (Brown et al., 2011; Fahl and Stein, 2012). Therefore, the sea-ice biomarker IP_{25} is usually used to reconstruct spring/summer sea-ice conditions.

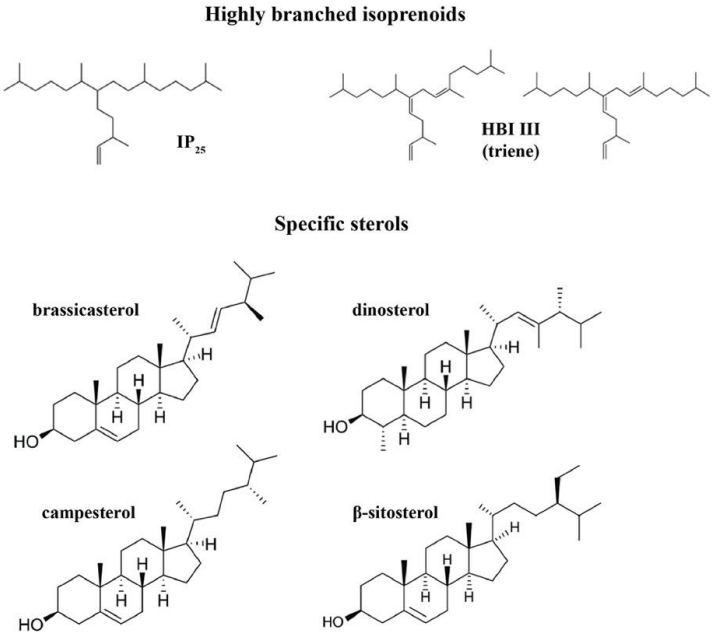

Figure 1.19: Chemical structure of highly branched isoprenoids (HBIs) and specific sterols.

Application of IP_{25} for sea-ice reconstruction is challenged by two extreme scenarios, as permanent sea-ice and ice-free conditions can both result in absence of IP_{25}. In this context, combining with open-water phytoplankton biomarkers can help to distinguish between the two scenarios. Under the circumstances of absent IP_{25}, high concentrations of open-water phytoplankton biomarker indicate ice-free conditions while low to absent

phytoplankton biomarkers reflect a permanent sea-ice cover. Accordingly, Müller et al. (2011) has established a semi-quantitative approach (PIP_{25} index) to reconstruct sea-ice concentrations:

$$PIP_{25} = [IP_{25}] / ([IP_{25}] + [\text{Phytoplankton biomarker}]*c)$$

in which factor c = mean IP_{25} concentration/mean phytoplankton biomarker concentration.

High PIP_{25} values (>0.75) indicate permanent sea-ice conditions, whereas intermediate values (0.5-0.75) reflect seasonal sea-ice conditions. Low PIP_{25} values (<0.5) are indicative for reduced sea ice or ice-free conditions (Müller et al., 2011).

The biomarkers brassicasterol and dinosterol are often used as indicators for marine phytoplankton (Fig. 1.19) (Fahl and Stein, 1999; Volkman, 1986). Their concentrations reflect open-water primary productivity. However, the brassicasterol in some settings has significant sources from freshwater systems, and interpretation in such cases needs more caution (Fahl et al., 2003; Hörner et al., 2016; Rampen et al., 2010; Volkman, 1986).

The tri-unsaturated HBI (triene) usually consists of two isomers (Z- and E-isomers) (Fig. 1.19). The Z-isomer of triene (also referred to as "HBI-III") is commonly found in open-water conditions and has also been proposed to indicate pelagic algal production (Belt et al., 2015; Smik et al., 2016a). Particularly, significant enhancement of HBI-III has been identified in marginal ice zones (MIZs). Therefore, HBI-III has been further used as an indicator for MIZs (Belt et al., 2015; Collins et al., 2013; Ribeiro et al., 2017; Smik et al., 2016a).

Recently, a study from the western Barents Sea found a close relationship between the spring chl *a* and the relative proportion of Z-triene and E-triene. Hence, the authors proposed a novel proxy HBI TR_{25} to indicate the spring phytoplankton blooms (Belt et al., 2019):

$$\text{HBI } TR_{25} = [\text{Z-triene}] / ([\text{Z-triene}] + [\text{E-triene}])$$

1.7.2 Terrestrial organic carbon

Multiple biomarkers have been applied to assess terrestrial OC input, e.g., campesterol, β-sitosterol, high molecular weight fatty acid (HMW-FA), and branched glycerol dialkyl glycerol tetraethers (b-GDGTs). The terrestrial biomarkers campesterol, β-sitosterol, and HMW-FA (consisting of 24-36 carbon atoms) typically have primary sources from the vascular leaf waxes (Eglinton and Eglinton, 2008; Volkman, 1986), while b-GDGTs are produced by bacteria and widely distributed in soil, lake, river, and peat (Blaga et al., 2010; De Jonge et al., 2014; Hopmans et al., 2004; Schouten et al., 2013; Weijers et al., 2007).

In addition to the specific terrestrial biomarkers, the $\delta^{13}C$ value of OC has been extensively used to distinguish terrestrial OC and marine OC. The terrestrial vascular plants fix carbon dominantly through a C_3 pathway, in which fractionation results in average biomass $\delta^{13}C$ values of −32‰ to −24‰ (Kohn, 2010), whereas C_4 plants fix carbon more efficiently and their biomass $\delta^{13}C$ values are between −13‰ to −10‰ (Cerling et al., 1997). Marine phytoplankton assimilates surface water dissolved organic carbon (DIC), characterized by $\delta^{13}C$ values

between −22‰ to −20‰ (Meyers, 1997). However, marine end-member values in the Arctic Ocean are less constrained due to many factors, e.g., high concentration of dissolved CO_2 at low SST, cell size, and cell membrane CO_2 permeability (Stein and Macdonald, 2004, and references therein). In the Arctic Ocean, a recent compilation shows that $\delta^{13}C$ of sea-ice phytoplankton ranges between −23‰ to −17‰ while values of phytoplankton are between −28‰ to −22‰ (Martens et al., 2019).

In combination with $\delta^{13}C$, the radiocarbon composition of bulk OC and terrigenous compounds can provide additional information of OC ages and sources. For instance, terrestrial OC from different reservoirs may be characterized by overlapped $\delta^{13}C$ values, and in this context, radiocarbon composition can help elucidate OC sources, e.g., fresh vegetation vs. pre-aged soil OC, topsoil OC vs. deeper soil OC. Besides, the radiocarbon age of terrestrial biospheric carbon to some degree reflects the residence time of terrestrial OC from intermediate pools, and their changes can further imply changes in climate factors and watershed properties, such as temperature, precipitation, and discharge (Douglas et al., 2014; Eglinton et al., 2021; Hein et al., 2020; Kusch et al., 2010; Schefuß et al., 2016; Vonk et al., 2019).

1.7.3 Freshwater discharge and hydrology

Long-chain alkyl diols produced by aquatic organisms (e.g., diatoms and marine microalgae) occur widely in marine and freshwater environments (cf., Rampen et al., 2012). The C_{28} 1,13- and C_{28} 1,14-diol, C_{30} 1,13-, C_{30} 1,14- and C_{30} 1,15-diol, and C_{32} 1,15-diol are often detected in marine sediments. Among them, the C_{32} 1,15-diol has been found particularly abundant in coastal regions and has been further identified dominantly produced in freshwater systems (de Bar et al., 2016; Lattaud et al., 2017b; Zhang et al., 2011). Accordingly, Lattaud et al. (2017) has used the fractional abundance of C_{32} 1,15-diol as a riverine input index:

$$\%C_{32}\ 1,15 = [C_{32}\ 1,15] / ([C_{32}\ 1,15] + [C_{30}\ 1,15] + [C_{30}\ 1,13] + [C_{28}\ 1,13]) \times 100\%$$

A study from the Amazon River suggests that the fractional abundance of C_{32} 1,15-diol can also be indicative for running water. The highest abundance of C_{32} 1,15-diol occurs in water bodies with low flow velocity and low turbidity, whereas in conditions of high flow velocity and high turbidity the fractional abundance of C_{32} 1,15-diol is the lowest (Häggi et al., 2019).

As the isotopic composition of freshwater is highly depleted in δ^2H/ $\delta^{18}O$ in comparison to that of seawater, it thus allows us to reconstruct river discharge by using hydrogen and/or oxygen isotopes. One of the most common approaches is to analyze the $\delta^{18}O$ and $\delta^{13}C$ of the planktic foraminifera (Keigwin et al., 2018; Poore et al., 1999; Spielhagen et al., 2005; Stein et al., 1994a). However, although $\delta^{18}O$ of the planktic foraminiferal shells mostly reflects the water salinity, one should keep in mind that the $\delta^{18}O$ can also be influenced by the water temperature (cf., Bagniewski et al., 2017) and they may have a counteracting effect. Besides, the dissolution of microfossils limits the application in some regions of the Arctic Ocean.

In this context, determining δ^2H values of marine algae biomarkers (e.g., dinosterol and brassicasterol) is an ideal approach to reconstruct river discharge or seawater salinity. The δ^2H of water mass and the water salinity together determine the δ^2H in marine algae biomarkers (cf., Sachs et al., 2018). In environments influenced by strong river discharge, the δ^2H gradients of surface water are closely related to salinity gradients and phytoplankton incorporates hydrogen isotopes into their lipids in proportion to the concentrations in water (Schouten et al., 2006; Zhang and Sachs, 2007). Besides, salinity influences the fractionation of hydrogen isotope, as higher salinity results in less $^2H/^1H$ fractionation (M'boule et al., 2014; Maloney et al., 2016; Nelson and Sachs, 2014; Schouten et al., 2006). These two effects work additively in marine environments and thus provide a basis for paleo-salinity reconstruction. Recently, a pilot study has successfully applied this approach in the Laptev Sea and the Beaufort Sea for salinity reconstruction (Sachs et al., 2018b).

Hydrological changes on land can be inferred from the isotopic composition of plant leaf wax lipids (δ^2H_{wax}). Hydrogen in water is the primary source to be incorporated into the leaf wax lipids by photosynthesis, and thus the changes in the isotopic composition of source water (δ^2H_{water}) can be recorded in δ^2H_{wax} (Sachse et al., 2012). On a global scale, the δ^2H_{wax} has a strong correlation with the δ^2H of local precipitation (Ladd et al., 2021; Liu and An, 2019; McFarlin et al., 2019). Therefore, δ^2H_{wax} has been widely used to reconstruct the hydroclimate change (Hein et al., 2020; Sachs et al., 2018a).

1.8 Rationale and key questions of this thesis

Sea ice is an important component of the Arctic climate system, and modern satellite observation has recorded drastic sea-ice loss over the past decades. Anthropogenic activities and greenhouse gas emissions have been proposed as the main triggers for Arctic warming and sea-ice retreat (Notz and Stroeve, 2016). However, the history of sea-ice natural variability beyond instrumental records, especially the sea-ice record from glacial to interglacial period is limited. Some records extending to the last deglaciation are mainly from the eastern Arctic and the Fram Strait (Belt et al., 2015; Fahl and Stein, 2012; Hörner et al., 2016; Müller et al., 2009; Müller and Stein, 2014), therefore more records from the western Arctic are needed to study sea-ice variability and its response to insolation forcing and climate change.

In addition to the Arctic sea ice, another important component in the climate system at high latitude is the ice sheet. The glacial-interglacial cycles are characterized by significant ice-sheet advance and retreat, driven by insolation changes. During the deglaciation, a direct consequence of ice-sheet decay is the meltwater injection into the ocean. The meltwater injection may modulate the rate and timing of climate change by regulating the freshwater budget and oceanic circulation (Fisher et al., 2002; Lohmann et al., 2020; Peltier et al., 2006; Tarasov and Peltier, 2005; Zhu et al., 2014). One of the most famous abrupt climate changes is the Younger Dryas cooling event which has been related to a slowdown of AMOC and likely triggered by meltwater discharge from the LIS (Broecker et al., 1989; McManus et al., 2004; Murton et al., 2010). Hence, identification of timing, magnitude, and pathway of this meltwater discharge is of significance to improve our understanding of abrupt climate change during the transition from glacial to interglacial period.

The ice-sheet decay may also have influences on the remobilization of terrestrial OC via direct and indirect ways. For example, the retreat of ice sheets has resulted in a sea-level rise of 120 m during the last deglaciation (Lambeck et al., 2014). It has flooded the Arctic shelves/coasts which contained large amounts of permafrost carbon. Some initial evidence suggests that such a process may have occurred in pulses and the remobilized permafrost carbon probably has contributed to the rapid deglacial CO_2 rises (Martens et al., 2020; Meyer et al., 2019; Winterfeld et al., 2018). However, so far, the processes of shelf flooding/coastal erosion of permafrost cannot be unambiguously distinguished from other processes, particularly during the warm periods when permafrost thawing from the inland active layer may have also contributed old permafrost carbon to marine sediments.

Besides, for regions covered by ice sheets, the relationship between glacial retreat and OC_{petro} mobilization is understudied. During the last deglaciation, the ice-sheet retreat has exposed substantial eroded rock, resulting from glacial grinding/erosion and glacial-retreat-induced isostatic uplift. As modern observations suggest that the oxidation rates of OC_{petro} are controlled by physical erosion of rocks (Hilton and West, 2020; Horan et al., 2017), it is of interest to investigate the OC_{petro} mobilization during the ice-sheet retreat and evaluate its potential impact on atmospheric CO_2.

Marine sediments from the Canadian Beaufort Sea archiving information of regional sea-ice history, surface-water characteristics, and land-derived OC, present an excellent opportunity to study the above-mentioned components of the Arctic climate system. In this thesis, multiple biomarkers and isotopes are used to address the following research objectives and hypotheses:

1. What was the sea-ice history in the Beaufort Sea over the last 14 kyrs? What did control the sea-ice variability?

It is an ideal region to study the possible mechanisms controlling sea-ice variabilities, i.e., insolation, climate, or freshwater discharge. Sea-ice biomarker IP_{25} from the core ARA04C/37 has been used to reconstruct sea-ice variability in the Beaufort Sea. Besides, the proxies indicative for SST and terrestrial input have been reconstructed to study the relationship with sea-ice changes.

2. Did permafrost OC remobilization also occur in the Canadian Beaufort Sea? If yes, what were the timing and source?

The existence of LIS hindered permafrost-soil formation in the hinterland, therefore the OC from inland permafrost thawing was negligible during the last deglaciation. Any identification of ancient permafrost carbon most likely indicates a source from coastal permafrost OC via coastal erosion. Radiocarbon dating of terrestrial compounds (i.e., HMW-FAs) has been conducted to test the hypothesis of coastal erosion and its timing.

3. Did ice-sheet retreat cause OC_{petro} mobilization? What was its potential impact on atmospheric CO_2?

Radiocarbon dating of bulk OC and indicators for carbon thermal maturity have been used to identify the OC_{petro} mobilization during the deglaciation. As shales are the primary sources for OC_{petro}, an estimate of OC_{petro} release from shales during the glacial retreat provides new insights into the potential impact of OC_{petro} oxidation on atmospheric CO_2.

4. Was the Mackenzie River an outlet for the Younger Dryas flood into the Arctic Ocean? If yes, what was the timing and magnitude of the flood?

One of the hypotheses about the Younger Dryas flood is that the flood was an outburst from Lake Agassiz and it drained through the Mackenzie River into the Arctic Ocean, further to the region of the Deep Atlantic Water Formation. To test the hypothesis, δ^2H values of leaf wax lipids (HMW-FAs) and marine phytoplankton biomarkers (i.e., brassicasterol and dinosterol) have been analyzed to reconstruct the paleo-salinity of surface water of the Canadian Beaufort Sea. Both the hydrological changes on land and in surface water can provide information about the timing, magnitude, and pathway of the YD flood.

1.9 Outline of thesis and declaration of author's contribution

The thesis consists of 6 main chapters and they are outlined as follows:

Chapter 1 gives an introduction of (1) Arctic sea ice, (2) terrestrial OC at high latitude, (3) climate evolution since the LGM, (4) study area, and (5) approaches used in this thesis. Key scientific questions and strategies to answer these questions are addressed in this chapter.

Chapter 2 presents the study core ARA04C/37 and describes the main methodology of organic geochemical analyses used in this thesis.

Chapter 3 (paper I) presents reconstructions of sea ice, SST, primary production, and terrestrial input in the Canadian Beaufort Sea, based on a biomarker approach. The southern Beaufort Sea was nearly ice-free during the deglaciation and sea ice expanded during the Holocene. Two events of high sediment flux were identified at ca. 13 kyr BP and 11 kyr BP, respectively. The first event can be attributed to the Younger Dryas flood and the second one seems to be related to coastal erosion.

Chapter 4 (paper II) presents a study of ancient terrestrial OC remobilization in the Beaufort region. Radiocarbon dating on bulk OC and terrestrial compounds (i.e., HMW-FAs) were performed to characterize the carbon age, while multiple proxies derived from biomarker and pyrolysis were used to indicate the thermal maturity of OC. Glacial retreat has caused substantial OC_{petro} mobilization during the deglaciation and occurrences of coastal erosion have been identified at ca. 14 kyr BP and 11 kyr BP. Carbon release from the two processes has a long-term effect on atmospheric CO_2, i.e., an increase of 12 ppm in CO_2 levels and a decrease of 12 permil in $\Delta^{14}C$.

Chapter 5 (paper III) aims to present the reconstructions of past hydrological changes in the Beaufort region. We analyzed δ^2H values of algal lipids (brassicasterol and dinosterol), leaf wax lipids (HMW-FAs), and generic FAs (short-chain FAs). Both the δ^2H records of algal lipids and leaf wax lipids have identified the Younger

Dryas flood event at the onset of YD. Meanwhile, salinity reconstruction based on δ^2H of dinosterol suggests a salinity depression of ~24 during the YD flood, which is larger than the previous estimate.

Chapter 6 concludes all findings and addresses key questions of the thesis. In the end, this chapter discusses remaining questions and presents an outlook of future research.

The cumulative thesis is constituted of three joint-authorship papers that have been or will be published in scientific journals. The author's contributions for each work have been outlined as follows:

Paper I: Deglacial to Holocene variability in surface water characteristics and major floods in the Beaufort Sea

Authors: Junjie Wu, Ruediger Stein, Kirsten Fahl, Nicole Syring, Seung-Il Nam, Jens Hefter, Gesine Mollenhauer, Walter Geibert

Publication state: This manuscript has been published (October 2020) in the Journal Communications Earth & Environment.

J. Wu, R. Stein and K. Fahl designed the project and experiment. The sediment core ARA04C/37 was provided by S. Nam. J. Wu performed the biomarker analyses (i.e., HBI, GDGTs, diols, and sterols). K. Fahl and J. Hefter conducted data quality control. N. Syring performed preparation of samples (freeze-drying and grinding) and bulk OC analyses (TOC, CNS). S. Nam carried out bulk parameter analyses ($\delta^{13}C$). J. Wu identified foraminifers to develop an age-depth model and W. Geibert measured ^{210}Pb for age constraint of surface sediments. J. Wu wrote the first version of manuscript with strong input from R. Stein. Afterwards, all authors contributed to the final version of this paper.

Paper II: Deglacial exhumation of petrogenic carbon and mobilization of thawed permafrost in the Canadian Arctic and their impact on the carbon cycle

Authors: Junjie Wu, Gesine Mollenhauer, Ruediger Stein, Peter Köhler, Jens Hefter, Kirsten Fahl, Hendrik Grotheer, Bingbing Wie, Seung-Il Nam

Publication state: This manuscript has been submitted to the Journal Nature Communications and is in review.

J. Wu, R. Stein and G. Mollenhauer designed this study, and the material was provided by S. Nam and L. Keigwin. S. Nam also provided the X-ray digital photographs J. Wu carried out biomarker analysis (i.e., hopanes and alkanes). For radiocarbon dating, J. Wu analyzed radiocarbon of bulk OC and extracted lipids (HMW-FAs) for compound dating. J. Hefter purified the long-chain FAs by preparative capillary gas chromatography (PCGC). H. Grotheer, T. Gentz, and E. Bonk analyzed radiocarbon content using the MICADAS system. P. Köhler estimated carbon release from OC_{petro} oxidation and assessed its impact on atmospheric CO_2 by using the carbon cycle model BICYCLE. R. Stein provided and evaluated the Rock-Eval

pyrolysis of bulk OC. J. Wu wrote the manuscript with input from G. Mollenhauer and R. Stein. All co-authors contributed to the final version of the manuscript.

Paper III: Lipid hydrogen isotopes and freshwater discharge in the Younger Dryas and Holocene Beaufort Sea, Arctic Ocean

Authors: Junjie Wu, Ruediger Stein, Julian Sachs, Matthew Wolhowe, Kirsten Fahl

Publication state: This manuscript is in preparation and to be submitted to the Journal Organic Geochemistry.

J. Wu and R. Stein designed this study. J. Wu and M. Wolhowe extracted lipids, i.e., brassicasterol, dinosterol, and FAs. M. Wolhowe purified these lipids and conducted hydrogen isotope analyses of all the lipids. J. Wu wrote the manuscript with input from R. Stein and J. Sachs. All co-authors contributed to the final version of the manuscript.

2. Material and methods

The thesis focuses on sediment core ARA04C/37 from the southern Beaufort Sea in concert with a few samples from the nearby core JPC15 (Keigwin et al., 2018) (Fig. 1.17a). Investigations are based on analyses of multiple biomarkers and isotopes. This chapter gives an introduction to the study material, including the core location and chronology. In the second part of this chapter, the organic-geochemical approaches were described.

2.1 Material

2.1.1 Core ARA04C/37

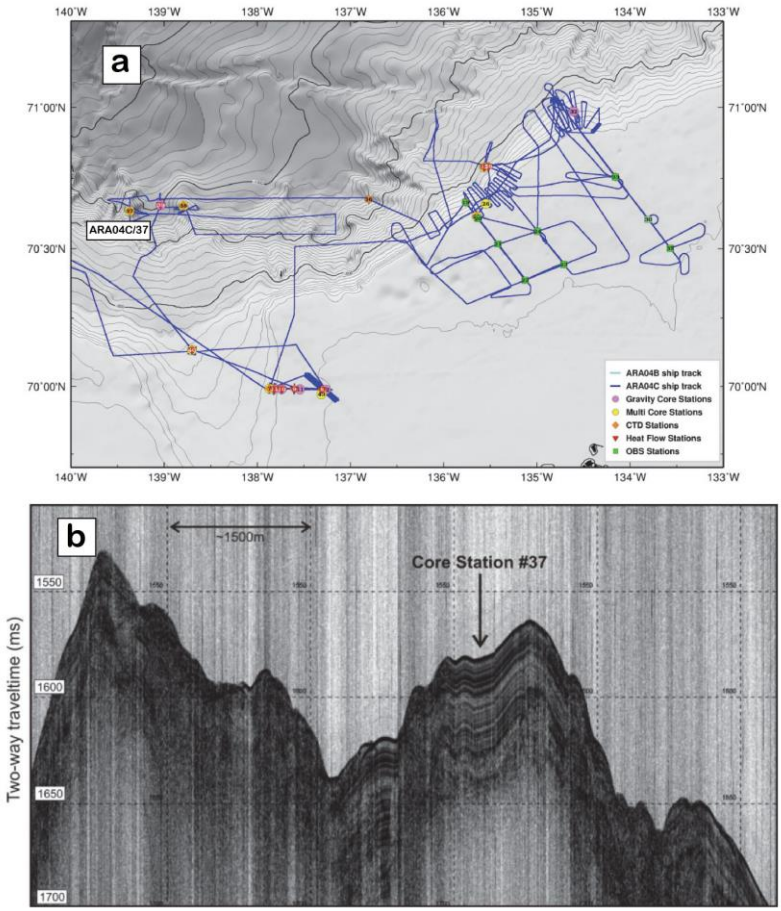

Figure 2.1: (**a**) Ship track for Expedition ARA04C. (**b**) Acoustic profile across core station #37. The core site was chosen to target the package of well laminated sediments on top of the western ridge seen in the area (source: Jin, 2013).

The gravity core ARA04C/37 was obtained during the Araon Cruise ARA04C in 2013 (Jin, 2013). The core was recovered from the southern Beaufort Sea continental slope (Fig. 2.1; water depth of 1173 m) off the Mackenzie River (Fig. 1.17a; 70°38.0212′N, 139° 22.0749′W). Total recovery of this core is 595 cm and it

consists of two units. Unit 1 (0-280 cmbsf) contains bioturbated silty clay and Unit 2 (280-595 cmbsf) consists of finely laminated sediments (discussed in chapter 4), i.e., silty clay/clayey silt alternations.

2.1.2 Chronology

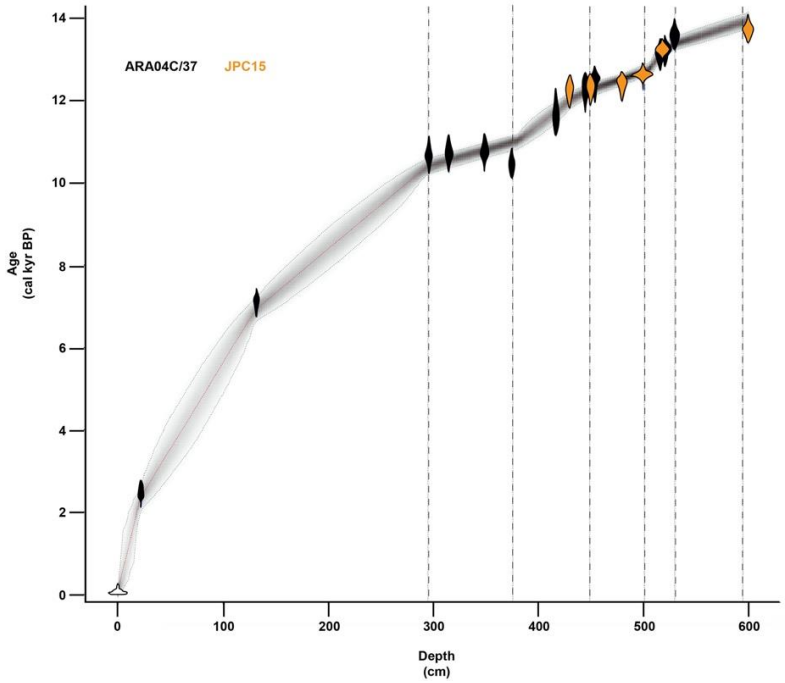

Figure 2.2: Age-depth model based on Bacon (Blaauw and Christen, 2013; Blaauw and Christeny, 2011) combines AMS ^{14}C dates from core ARA04C/37 (black) and core JPC15 (orange) (Keigwin et al., 2018).

The chronology of core ARA04C/37 is constrained by accelerator mass spectrometry (AMS) ^{14}C dating of calcareous foraminifera. As the magnetic susceptibility of core ARA04C/37 is in good correlation with the nearby core JPC15 between ca. 300-520 cmbsf and ^{14}C dates from the two cores are highly consistent below 400 cmbsf, we established the age-depth model by including six AMS^{14}C dates from core JPC15 (Table 2.1). Choice of ΔR in the southern Beaufort Sea has been discussed in detail by Keigwin et al. (2018). These authors propose that no proper data from the western Arctic can be used to estimate ΔR but the data from the Nordic Seas suggest an increase of ΔR of 200 years during the YD. Therefore, ΔR of 200±100 years was assigned for AMS^{14}C dates from the YD, and ΔR of 0±100 years was assigned for dates from the Holocene and B/A. Excess ^{210}Pb in the uppermost centimeters and detectable anthropogenic ^{137}Cs in the core-top sample identified modern surface sediments, therefore the core top was fixed to 0 kyr BP. The age-depth model has been established by the "Bacon" software of Blaauw and Christen (2013) (Fig. 2.2). Because the most up-to-date marine calibration curve Marine20 is intended for marine radiocarbon samples from non-polar regions (Heaton et al., 2020), all ^{14}C ages were transformed into calendar age via the Marine13 curve (Reimer et al., 2013).

Table 2.1: Chronology of core ARA04C/37 and AMS ^{14}C dates adopted from core JPC15

Lab ID	Depth (cm)	Species	AMS14C age (year)	△R	Calibrated age* (cal. year BP)	Model age** (cal. year BP)
AWI-2104.1.1	22	mixed	2738±73	0±100	2469±157	2345±313
AWI-2261.1.1	132	mixed	6588±86	0±100	7093±149	6923±287
AWI-2105.1.1	296	planktic	9735±103	0±100	10648±198	10394±190
AWI-2106.1.1	315	planktic	9782±94	0±100	10711±187	10549±186
AWI-2107.1.1	349	planktic	9812±99	0±100	10750±189	10787±179
AWI-2108.1.1	375	planktic	9561±101	0±100	10538±184	10974±176
AWI-2109.1.1	417	planktic	10450±110	0±100	11615±267	11726±243
NOSAMS-134017[a]	430	*Nps*	10800±35	0±100	12262±185	11996±202
AWI-2110.1.1	445	planktic	10846±102	0±100	12295±213	12206±166
NOSAMS-110672[a]	450	*Nps*	11050±45	200±100	12323±179	12256±164
AWI-2111.1.1	454	mixed	11195±103	200±100	12482±181	12292±160
NOSAMS-131596[a]	480	*Nps*	11100±30	200±100	12392±160	12512±132
NOSAMS-123914[a]	500	*Nps*	11300±35	200±100	12621±87	12705±144
AWI-2114.1.1	516	planktic	11652±106	0±100	13121±156	13092±161
NOSAMS-131597[a]	520	*Nps*	11750±35	0±100	13226±103	13200±131
AWI-6472.1.2	521	planktic	11756±101	0±100	13233±140	13220±123
AWI-6474.1.2	530	planktic	12095±104	0±100	13553±154	13381±157
NOSAMS-110673[a]	600	*Nps*	12250±60	0±100	13707±142	13948±195

[a]AMS14C dates adopted from core JPC15 (Keigwin et al., 2018).

*Calibrated ages with 1σ uncertainty, using Calib 7.1 (Stuiver et al., 2020) and based on calibration curve Marine13 (Reimer et al., 2013).

**model ages with default 95% confidence ranges based on Bayesian model (Bacon) (Blaauw and Christeny, 2011) and Marine13 in this study (Reimer et al., 2013). AMS^{14}C dates from core JPC15 were recalibrated.

2.2 Methods

Sediments were sub-sampled, freeze-dried, and ground. The geochemical analyses of each sample are described in detail in the following subsections, procedures shown in Fig. 2.3.

2.2.1 Bulk parameters

(1) Total organic carbon (TOC)

For TOC analyses, sediments were freeze-dried, ground, and homogenized. Removal of carbonates was performed by adding hydrochloric acid. TOC contents of 100 ug sediments were determined using a Carbon-Sulfur Analyser (CS-125, Leco).

(2) Total carbon (TC)

The TC contents were analyzed by a Carbon-Nitrogen-Sulfur Analyser (Elementar III, Vario). Assuming calcite is the primary source of carbonate, carbonate contents can be estimated by the equation $CaCO_3$ = (TC-TOC) * 8.333 and 8.333 is the stoichiometric factor.

(3) Carbon isotope composition of organic carbon ($\delta^{13}C_{org}$)

The stable carbon isotope composition of organic matter ($\delta^{13}C_{org}$) was analyzed by Thermo Delta V Isotope Ratio Mass Spectrometer connected to a Thermo Flash 2000 CHNS/OH Elemental Analyzer after decarbonization with hydrochloric acid. The $\delta^{13}C_{org}$ values are given in per mil notation relative to Vienna Pee Dee Belemnite International Standard. The analytical error was determined by duplicate analyses for randomly selected samples. Analytical precision is within 0.2‰.

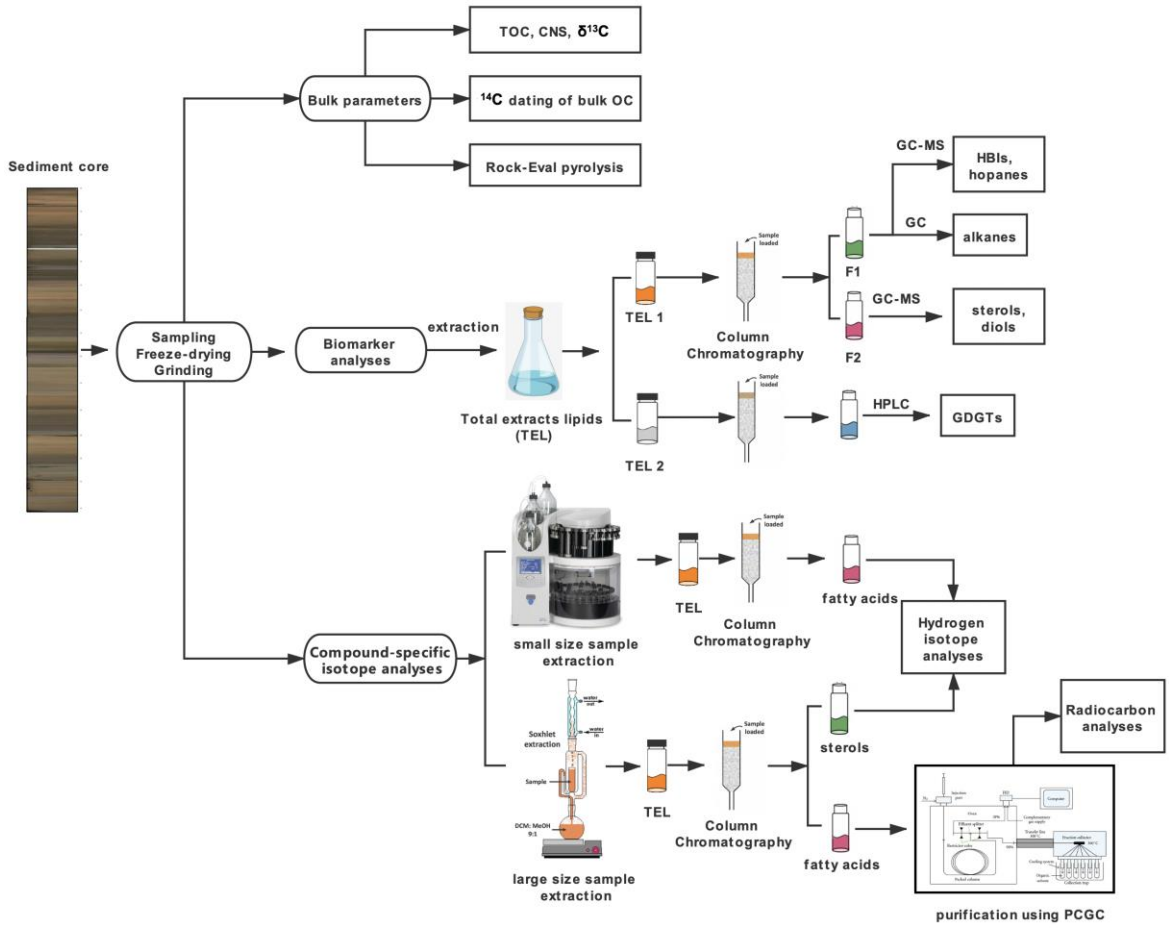

Figure 2.3: Schematic sketch of the laboratory procedures.

(4) Rock-Eval pyrolysis

Rock-Eval pyrolysis was performed on bulk sediment samples following Espitalie et al. (1977). Hydrogen contents were measured as hydrocarbon-type compounds whereas oxygen contents of samples were measured as carbon dioxide yields. These contents were normalized to organic carbon as hydrogen index (mgHC/gC) and oxygen index ($mgCO_2$/gC), respectively. In a van Krevelen-type diagram, a classification illustrating carbon types is possible (cf., Meyers and Teranes, 2002). Furthermore, the temperature at which cracking of

kerogen produces the maximum hydrocarbons (T_{max}) is characteristic of the maturity stage of the OC. Immature OC has T_{max} values of less than 435 °C.

(5) Radiocarbon dating of bulk organic carbon

Sediment samples containing ca. 1 mg OC were acidified (6N HCl) in silver capsules to remove inorganic carbon. Samples were dried and stored at 60 °C until analyses. Sediments as well as the silver capsules were packed into tin capsules and combusted by an Elementar vario ISOTOPE EA (Elemental Analyzer). Oxidized carbon (CO_2) was graphitized by the Ionplus AGE3 system (Wacker et al., 2010c). Radiocarbon analyses of the samples were conducted along with reference standards (oxalic acid II; NIST 4990c) and blanks (phthalic anhydride; Sigma-Aldrich 320064) and in-house reference sediments via the Ionplus MICADAS dating system (Mollenhauer et al., 2021). Blank correction and standard normalization were performed by the BATS software (Wacker et al., 2010b).

2.2.2 Biomarker analyses

(1) Biomarker lipid extraction and purification

(**a**) Freeze-dried sediments (ca. 5-7 g) were added with internal standards prior to analytical treatment, 7-hexylnonadecane (7-HND, 0.076 ug per sample), 5α-androstan-3β-ol (androstanol, 10.7 ug per sample), and squalene (3.2 mg per sample). Samples were extracted ultrasonically (15 min) with 30 ml of DCM:MeOH (2:1, v/v), repeated for three times. The total lipid extracts (TLE) were concentrated to 5 ml by rotary evaporation (40-45 °C), and then transferred to a glass vial by MeOH. The lipids were further extracted by *n*-hexane for 3 times.

TLE were purified by open column chromatography filled with silica gel (6 mm i.d.*4.5 cm) (60-200 um particle size). The lipids were eluted by 5 ml *n*-hexane for hydrocarbon fractions, followed by 9 ml ethyl acetate:hexane (1:4, v/v) for alcohol fractions.

The alcohol fractions were further derivatized with 200 μl bis-trimethylsilyl-trifluoracet-amid (BSTFA) at 60 °C for 2 hours.

(**b**) For GDGT analyses, sediments (ca. 5-7 g) were extracted ultrasonically (15 min) with 30 ml of DCM:MeOH (2:1, v/v) for three times, with internal standard (C_{46}-GDGT, 1 μg per sample) added prior to analytical treatment. TLE were concentrated to 5 ml by rotary evaporation (40-45 °C), and then transferred to a glass vial by MeOH and then dried under nitrogen.

TLE were purified by open column chromatography filled with silica gel (6 mm i.d.*4.5 cm) (60-200 um particle size). The lipids were eluted by 5 ml *n*-hexane for hydrocarbon fractions, followed by 5 ml DCM:MeOH (1:1, v/v) for GDGT fractions.

The GDGT fractions were dried and re-dissolved in hexane:isopropanol (99:1, v/v), and then filtered via a polytetrafluoroethylene filter with a pore size of 0.45 μm.

(2) Instrumental analyses

(**a**) **HBIs analyses**: The hydrocarbon fractions were analyzed by gas chromatography (GC) Agilent 7890B (30 m DB-1MS column, 0.25 mm i.d., 0.25 μm film thickness) coupled to a mass spectrometry (MS) Agilent 5977A MSD (70 eV constant ionization potential, Scan 50-550 *m/z*, ion source temperature 230 °C, Performance Turbo Pump). The GC oven temperature program is: 60 °C for 3 min, a ramp of 15 °C/min to 150 °C, followed by a ramp of 10 °C/min to 320 °C and the final temperature held for 15 min.

(**b**) **Sterols analyses**: The alcohol fractions were analyzed by GC-MS (Agilent 7890B GC-Agilent 5977A MSD, same conditions as above). The GC oven ramped temperature program is: 60 °C for 2 min, at a heating rate of 15 °C/min to 150 °C, followed by a ramp of 3 °C/min to 320 °C and the final temperature held for 20 min.

(**c**) **Hopanes and long-chain diols analyses**: The hydrocarbon fractions (containing hopanes) and alcohol fractions (containing long-chain diols) were analyzed by GC-MS (Agilent 6850 GC-Agilent 5975C VL MSD) operating in electron impact mode (70 eV). The GC is equipped with a fused silica capillary column (30 m Restek Rxi-1MS, 0.25 mm i.d., 0.25 μm film thickness). The GC temperature program is: 60 °C for 3 min, at a heating rate of 20 °C/min to 150 °C, followed by a ramp of 4 °C/min to 320 °C and the final temperature held for 15 min.

(**d**) **Alkanes analyses**: The hydrocarbon fractions were analyzed using an Agilent 7890A GC (60 m DB-5MS column, 0.25 mm i.d., 0.25 μm film thickness coupled to a 5 m, 0.53 mm i.d. deactivated fused silica precolumn) and a flame ionization detector (FID). The ramped temperature program is: 60 °C for 1 min, at a heating rate of 20 °C/min to 150 °C, followed by a ramp of 6 °C/min to 320 °C and the final temperature held for 35 min.

(**e**) **GDGT analyses**: The GDGT fractions were analyzed by a high-performance liquid chromatography (HPLC, Agilent 1200 series HPLC system) coupled to a single quadrupole MS (Agilent 6120 MSD) via an atmospheric pressure chemical ionization (APCI) interface. Separation of individual GDGTs was achieved on two UPLC silica column in series (Waters Acquity BEH HILIC, 2.1×150 mm, 1.7 μm), with a 2.1×5 mm pre-column maintained at 30 °C. Mobile phase A consists of hexane:chloroform (99:1, v/v), and mobile phase B consists of hexane:2-propanol:chloroform (89:10:1, v/v/v). Samples (20 μl) were eluted with 18 % mobile phase B for 25 min, followed by a linear increase in mobile phase B to 50% within 25 min, and then to 100% for the next 30 min.

(3) Identification and quantification of biomarkers

(**a**) **HBIs** were analyzed in selected ion monitoring (SIM) mode with a detection window of 17-19 min. Identification of compounds was carried out on basis of GC retention time and fragmentation pattern from MS. The fragmentation pattern has been compared with published mass spectra (Belt et al., 2007; Brown and Belt, 2016). The calculated Kovats Index is 2085 for IP_{25}, 2084 for HBI II, and 2046 for HBI III. For quantification

of HBIs, their molecular ions (*m/z* 350 for IP_{25}, *m/z* 348 for HBI II, and *m/z* 346 for HBI-III) were used in relation to the fragment ion *m/z* 266 (internal standard 7-HND). External calibration curves were applied and specific response factors were calculated for these ions. For more details we refer to Fahl and Stein (2012).

(**b**) **Sterols** were measured in a full scan (SCAN) mode. Identification of sterols was carried out by comparison with published mass spectra (Boon et al., 1979; Volkman, 1986). Retention indices for brassicasterol (as 24-methylcholesta-5,22E-dien-3β–O–$Si(CH_3)_3$), dinosterol (as 4α,23,24R-trimethyl-5α-cholest-22E-en-3β-O-$Si(CH_3)_3$), campesterol (as 24-methylcholest-5-en-3β–O–$Si(CH_3)_3$), and β-sitosterol (as 24-ethylcholest-5-en-3β–O–$Si(CH_3)_3$) were calculated to be 1.018, 1.019, 1.042, and 1.077 (normalized to androstanol to be 1.000), respectively. For quantifications of sterols, the molecular ions (*m/z* 470 for brassicasterol, *m/z* 472 for campesterol, *m/z* 486 for β-sitosterol, and *m/z* 500 for dinosterol) were used in relation to the *m/z* 348 of internal standard androstanol. External calibration curves and specific response factors were applied.

(**c**) **Long-chain diols** were identified in a SIM mode with following *m/z*: 313.3 (C_{28} 1,13-diol, C_{30} 1,15-diol) and 341.3 (C_{30} 1,13-diol, C_{32} 1,15-diol) (Rampen et al., 2012; Versteegh et al., 1997). Fractional abundances were calculated based on peak areas of these compounds.

(**d**) **Hopanes** were measured in a SCAN mode. Homohopane (C_{31}) isomers 17β,21β(H), 22R (C_{31}ββR), 17β,21α(H), 22R (C_{31}βαR), 17β,21α(H), 22S (C_{31}βαS), 17α,21β(H), 22R (C_{31}αβR), and 17α,21β(H), 22S (C_{31}αβS) were identified by *m/z* 191 and 205. Fractional abundances were calculated based on peak areas of these compounds.

(**e**) **Alkanes** were identified by comparison of compound retention times with reference sample. For quantification of alkanes, respective peak areas of alkanes (different chain length) were used in relation to the peak area of internal standard squalene.

(**f**) **GDGTs** were identified by a SIM mode of the following $(M+H)^+$ ions: *m/z* 1302.3 (iGDGT-0), *m/z* 1300.3 (iGDGT-1 and OH-GDGT-0), *m/z* 1298.3 (iGDGT-2 and OH-GDGT-1), *m/z* 1296.3 (iGDGT-3 and OH-GDGT-2), *m/z* 1292.3 (Crenarchaeol and its isomer), *m/z* 1050 (GDGT-IIIa/IIIa'), *m/z* 1048 (GDGT-IIIb/IIIb'), *m/z* 1046 (GDGT-IIIc/IIIc'), *m/z* 1036 (GDGT-Iia/Iia'), *m/z* 1034 (GDGT-Iib/Iib'), *m/z* 1032 (GDGT-Iic/Iic'), *m/z* 1022 (GDGT-Ia), *m/z* 1020 (GDGT-Ib), *m/z* 1018 (GDGT-Ic), and *m/z* 744 (C_{46}-GDGT). Quantification of GDGTs was carried out by comparison of respective peak areas to that of internal standard C_{46}-GDGT.

(4) Calculation of accumulation rates

All biomarker concentrations were normalized to weight of sediment or TOC content. Accumulation rates of bulk sediment, bulk OC, $CaCO_3$, and biomarkers are calculated by following equations:

$$BulkAR = SR * (WBD-1.026*PO)$$

$$TOCAR = BulkAR * TOC$$

$$CaCO_3AR = BulkAR * CaCO_3$$

$$BMAR = BulkAR * BM$$

BulkAR = bulk sediment accumulation rate (g cm^{-2} kyr^{-1});

SR = sedimentation rate (cm kyr^{-1});

WBD = wet bulk density (g cm^{-3});

PO = porosity (%);

TOCAR = total organic carbon accumulation rate (g cm^{-2} kyr^{-1});

$CaCO_3AR$ = carbonate accumulation rate (g cm^{-2} kyr^{-1});

BMAR = biomarker accumulation rate (μg cm^{-2} kyr^{-1});

BM = biomarker concentration (μg g^{-1} Sed).

2.2.3 Compound-specific isotope analyses

(1) Lipid extraction and purification

(**a**) **Sediments (ca. 50-70 g)** were extracted with DCM:MeOH (9:1, v/v) using a Soxhlet apparatus for over 48 hours. Total extracts were saponified with potassium hydroxide (KOH, 0.1 M) in MeOH:H_2O (9:1, v/v) at 80 °C for 2 hours. The neutral lipids were recovered from alkaline solution with *n*-hexane. The *n*-alkanoic acids were extracted from the remaining solution with DCM after adjusting the pH to a value of around 2 by addition of 37% HCl.

Purification of long-chain FAs: The extracted *n*-alkanoic acids were methylated with MeOH:HCl (95:5, v/v) with a known ^{14}C-signature in a nitrogen atmosphere at 80 °C for 12 hours. The fatty acid methyl esters (FAMEs) were extracted with *n*-hexane and further purified by silica gel column chromatography using DCM:hexane (2:1, v/v) as elution. The purified FAMEs with chain lengths >C_{24} were separated for target compounds by preparative caplillary gas chromatography (PCGC). The Agilent 6890N GC (30 m Restek Rxi-XLB, 0.53 mm i.d., 0.5 μm film thickness) equipped with a Gerstel Cooled Injection System (GIS) and connected to a Gerstel preparative fraction collector (Kusch et al., 2010). Around 1% of the column effluent was diverted to an FID, and the remaining 99% were collected in a series of glass U-traps. The target compounds were recovered by rinsing the traps with DCM.

Purification of sterols: The neutral lipids were separated on a 4 cm silica gel column chromatography (combusted silica gel+1% H_2O in *n*-hexane). Apolar compounds were eluted by 4 ml *n*-hexane, followed by polar-compound elution with ca. 4 ml DCM:MeOH (1:1, v/v). Apolar fractions were further separated on 5% H_2O deactivated silica gel column chromatography. The hydrocarbon fractions were eluted with 10 ml *n*-hexane, and the ketones fractions were eluted with 6 ml DCM:hexane (1:1, v/v). Finally, the alcohol fraction was eluted with 8 ml ethyl acetate:hexane (1:4, v/v). The alcohol fractions were divided into 5 approximately

equal aliquots and each was acetylated in 40 µl pyridine and 40 µl acetic anhydride, with a known isotopic composition, at 70°C for 0.5h. The hydrogen isotopic composition of the acetic anhydride was previously determined by derivatization of a derivatization working standard, and comparison to the same working standard derivatizat with acetic anhydride of known composition, provided by Arndt Schimmelmann of Indiana University.

Dinosterol and brassicasterol were then isolated from each aliquot using a preparative HPLC (Agilent 1100) following the methods of Nelson and Sachs (2013). Briefly, each aliquot was injected into a 4.6 × 250 mm, 5-micron Agilent XDB-C18 column in 30 ul of DCM:MeOH (2:1, v/v). The eluent was acetonitrile:MeOH (95:5, v/v), which was maintained for 10 min, then transitioned to acetonitrile:ethyl acetate:MeOH (85:10:5, v/v/v) over 10 min, maintained for 45 min, transitioned to 100% ethyl acetate over 10 min, and maintained for 10 min. Flow rate was constant at 1.5 ml min^{-1} and the column was maintained at 30°C. Brassicaterol and dinosterol were collected between 29.5-33.5 and 50.5-55.5 min, respectively. Sterol fractions were characterized via GC-FID and GC-MS, along with 1-minute-long collection windows before and after each sterol fraction to ensure quantitative recovery of the HPLC chromatographic peak. After characterization, the sterol isolates from parallel aliquots were recombined (per sterol).

(**b**) **Sediments (ca. 4 g)** were extracted with an Accelerated Solvent Extractor using DCM:MeOH (9:1, v/v) at 1000 psi and 100 °C for three 10-min cycles. The total extracts were saponified with 10 ml 1N KOH in MeOH and 1ml H_2O at 70°C for 12h, neutralized with 2 ml 6N HCl and 10 ml H_2O, phase separated into 10 ml *n*-hexane three times, the combined *n*-hexane fractions washed with an additional 10 ml H_2O, and passed through ~2 g of Na_2SO_4. FAs were collected off a 0.5 g aminopropyl-functionalized silica gel (Supelco) column in 8 ml of 4% acetic acid in diethyl ether after removing neutral compounds with 8 ml of DCM:isopropyl alcohol (3:1, v/v).

Purification of FAs: The acid fractions were methyl esterified overnight at 60 °C in 1 ml of dry *n*-hexane and 2 ml of 10% acetyl chloride in dry MeOH. Samples were phase-partitioned with 2 ml of *n*-hexane (3×) and 2 ml H_2O. The combined *n*-hexane fractions were passed through 2 g of Na_2SO_4. The hydrogen isotopic composition of the methanol derivatization reagent was previously determined by derivatization of phthalic acid of known composition, provided by Arndt Schimmelmann of Indiana University.

(2) Isotope analyses

(**a**) **Radiocarbon analyses**: The purified FAMEs were transferred in to 50 µl tin capsules and packed. The samples were combusted at 950 °C by the Elementar vario ISOTOPE EA (Elemental Analyzer) and the isotopic ratio ($^{14}C/^{12}C$) of produced CO_2 were determined by the directly connected MICADAS system which is equipped with a gas-ion source. The radiocarbon content of CO_2 produced from the reference standard (oxalic acid II; NIST 4990C) and blank (phthalic anhydride; Sigma-Aldrich 320065) were determined alongside with samples. Blank correction and standard normalization were performed using the BATS software (Wacker et al., 2010b). Radiocarbon data are reported as fraction modern carbon ($F^{14}C$).

Procedure blank was assessed by determination of $F^{14}C_{blank}$ ($F^{14}C$ of the blank) and the size of blank (m_{blank}). For this purpose, the in-house reference samples from ^{14}C-free Messel Shale ($F^{14}C_{OC} = 0$) and modern apple peel ($F^{14}C_{OC} = 1.029 \pm 0.001$) were processed in the same way as the compound-specific samples were conducted. Radiocarbon analyses of the reference samples were performed, and $F^{14}C_{blank}$ and m_{blank} were determined following the method of Sun et al. (2020). The procedure blank using 50 µl tin capsule is reported as 2.039 ± 0.135 µg C with the $F^{14}C$ value of 0.532 ± 0.032. All radiocarbon data of FAMEs were corrected for the procedural blank and, to remove the contribution of methyl group during the derivatization process, a methyl-correction was performed through isotopic mass balance. Uncertainties were fully propagated.

(**b**) **Hydrogen isotope analyses**: Hydrogen isotopic composition of lipids (δ^2H_{lipid}) were analyzed by a gas-chromatography isotope-ratio mass spectrometry (GC-IRMS). Gas chromatography was conducted using a Thermo Trace GC Ultra equipped with a GC-TC (pyrolysis) interface. Samples (~175 ng of the target compound per 2 ul injection) in toluene were injected into the 320 °C inlet in splitless mode, with a 1.1 ml/min helium carrier flow through a VF-17ms column (60 m, 0.25 mm i.d., 0.25 µm film thickness). For sterols (as acetates), the oven temperature was held at 130 °C for the 2-min splitless time, increased to 220 °C at a rate of 20 °C/min, increased to 325 °C at a rate of 2 °C/min, and held for 15 min. For FAs (as methyl esters), the oven temperature was held at 130 °C for the 2-min splitless time, increased to 320°C at a rate of 4 °C/min, and held for 28 min. The pyrolysis interface was operated at 1410 °C, and the sample hydrogen admitted to a Thermo Delta V Plus isotope ratio mass spectrometer via open split. External standards of known isotopic composition (*n*-alkanes; Arndt Schimmelmann of Indiana University) were injected throughout each sample sequence and used to correct lipid data for drift and offsets with sample size and retention time. For details of external standards and correction we refer to Sachs et al. (2016) and Nelson and Sachs (2014). Samples were analyzed in triplicate, and derivatization-corrected compositions determined via mass balance.

3. Deglacial to Holocene variability in surface water characteristics and major floods in the Beaufort Sea

Junjie Wu[1*], Ruediger Stein[1,2,3], Kirsten Fahl[1], Nicole Syring[1], Seung-Il Nam[4], Jens Hefter[1], Gesine Mollenhauer[1,2,3], Walter Geibert[1]

[1]Alfred Wegener Institute Helmholtz Centre for Polar and Marine Research, Am Alten Hafen 26, Bremerhaven 27568, Germany

[2]Faculty of Geosciences (FB5), University of Bremen, Klagenfurter Strasse 4, Bremen 28359, Germany

[3]MARUM—Center for Marine Environmental Sciences, University of Bremen, Bremen 28359, Germany

[4]Korea Polar Research Institute, 26 Songdomirae-ro, Yeonsu-gu, Incheon 21990, Republic of Korea

Abstract

Surface water characteristics of the Beaufort Sea have global climate implications during the last deglaciation and the Holocene, as (1) sea ice is a critical component of the climate system and (2) Laurentide Ice Sheet meltwater discharge via Mackenzie River to the Arctic Ocean and further to its outflow near the deep-water source area of the Atlantic Meridional Overturning Circulation. Here we present high-resolution biomarker records from the southern Beaufort Sea. Multi-proxy biomarker reconstruction suggests that the southern Beaufort Sea was nearly ice-free during the deglacial to Holocene transition, and a seasonal sea-ice cover developed during the mid-late Holocene. Superimposed on the long-term change, two events of high sediment flux were documented at ca. 13 and 11 kyr BP, respectively. The first event can be attributed to the Younger Dryas flood and the second event is likely related to a second flood and/or coastal erosion.

3.1 Introduction

Arctic sea ice, characterized by strong seasonal variations, is a critical component in the global climate system as sea ice has direct impact on climate change by regulating energy exchanges between the atmosphere and the ocean. The variability of sea ice contributes to changes of the albedo effect, the freshwater system, and the surface energy budget in the Arctic Ocean (Dai et al., 2019; Kim et al., 2019; Screen and Simmonds, 2010; Serreze et al., 2007). In a positive ice-albedo feedback, increases of absorbed energy result in further sea-ice melting (Loeb et al., 1997; Mundy et al., 2009). Increased melting and sea-ice export can slow down the Atlantic Meridional Overturning Circulation (AMOC) as well as the poleward heat transport (Sévellec et al., 2017). Due to these complex feedback processes, the Arctic is both a contributor of climate change and a region that is most strongly affected by global warming (Dai et al., 2019; Kim et al., 2019; Routson et al., 2019; Stroeve et al., 2007).

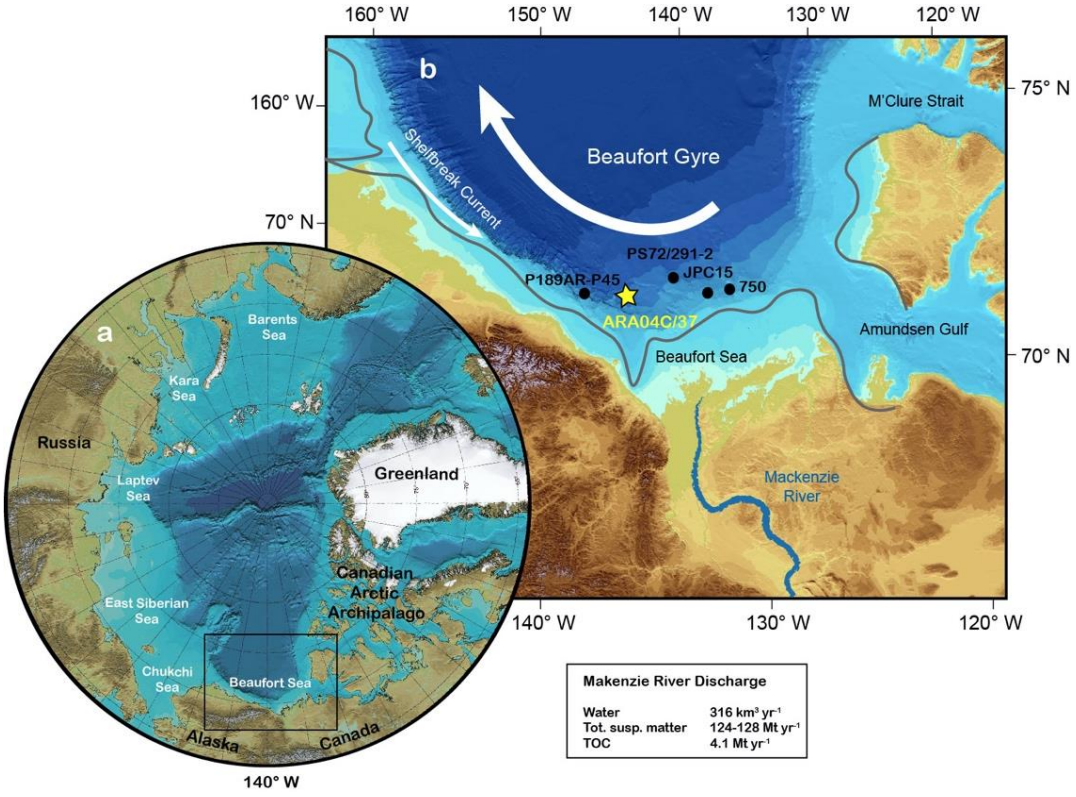

Figure 3.1 Overview of the Arctic Ocean and core location in this study. a overview of the Arctic Ocean and the study area (black box). **b** regional map presents the Beaufort Sea surface water circulation (white arrows), the Mackenzie River (blue line), and the coast at 14 kyr BP (gray lines) (Peltier et al., 2015). Location of Core ARA04C/37 is indicated by yellow star and other sediment cores discussed in the text (core information can be found in Supplementary Table 3.3) are indicated by black circles. Mackenzie River discharge of water, total suspended matter, and total organic carbon is listed in the box (Holmes et al., 2002; Stein and Macdonald, 2004).

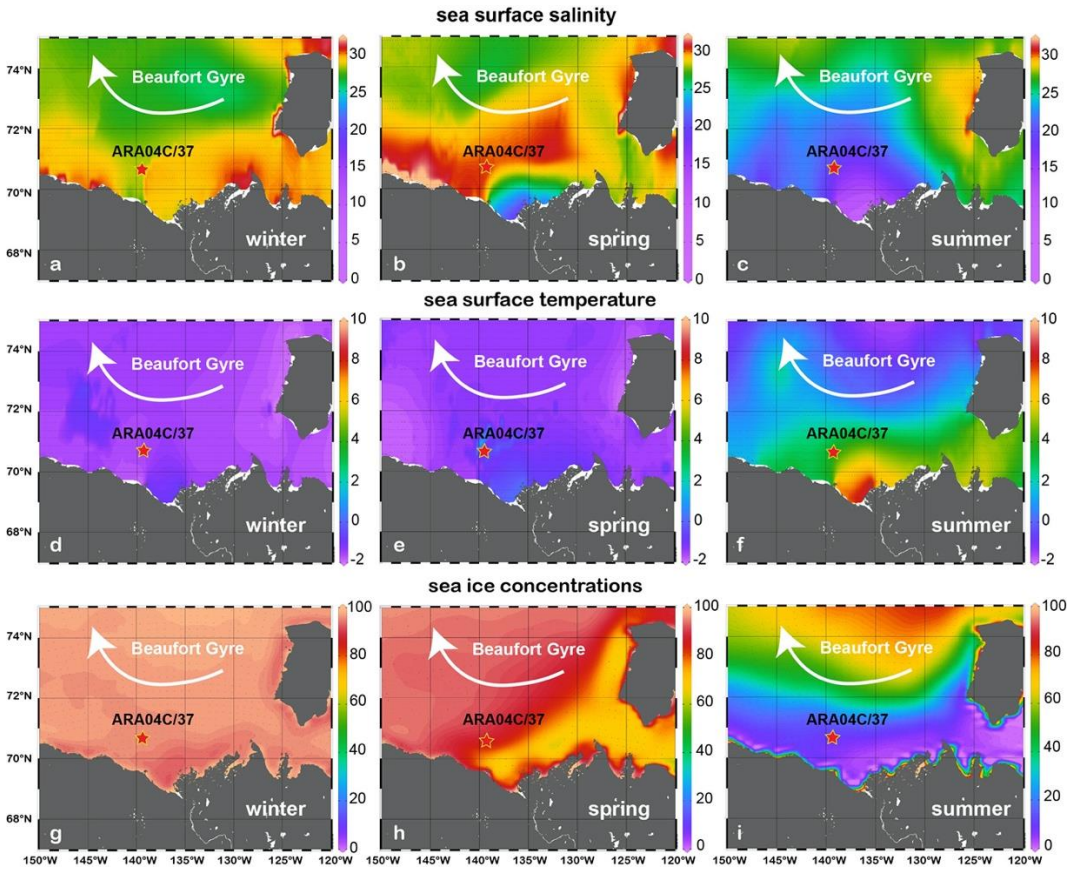

Figure 3.2 Modern surface water characteristics in the Beaufort Sea. a-c modern sea surface salinity, **d-f** modern sea surface temperature, **g-I** modern sea-ice concentrations. Data of (**a-f**) are from the World Ocean Atlas 2013 (data source: https://www.nodc.noaa.gov/OC5/woa13/). Data of (**g-i**) are averaged sea-ice concentrations from 1988-2007 (data source: http://nsidc.org). Maps were produced with Ocean Data View software (source: http://odv.awi.de/). White arrow represents the Beaufort Gyre circulation. Red star indicates location of Core ARA04C/37.

Arctic sea ice has reduced drastically over the past few decades, recognized in both satellite observations and model simulations (Parkinson and Cavalieri, 2008; Stroeve et al., 2007, 2012). Since 1980, the sea-ice cover has had a mean annual areal reduction of ~20% and an even stronger decrease of ~30% in September (Sévellec et al., 2017). This decrease in sea ice is also suggested to be the driver of the frequent cold extremes over Eurasia in the past two decades (Matsumura and Kosaka, 2019). Historical observations spanning the last few decades are deficient in length to decipher the processes of accelerated sea-ice retreat, thus longer-term and high-resolution proxy records of paleoenvironmental changes are needed. During transition from the last deglacial to the Holocene, climate system underwent numerous abrupt changes, particularly the Bølling/Allerød (B/A) interstadial and the Younger Dryas (YD) stadial periods. The Holocene, not concluded yet, has experienced a significantly warmer period during its early stage ("Early Holocene Thermal Maximum") (Kaufman et al., 2004). Causes of the abrupt climate change are not fully understood, hence special emphasis on the transition from the deglacial into the Holocene is of significance to understand the forcing mechanisms

of the climate system. In this context, the Arctic marginal seas characterized by strong seasonal variability in sea-ice cover, primary productivity and terrigenous (riverine) input are very sensitive to environmental changes and thus of major importance for paleoclimate reconstructions. One of these marginal seas is the Beaufort Sea (Fig. 3.1) which we focus on in this paper.

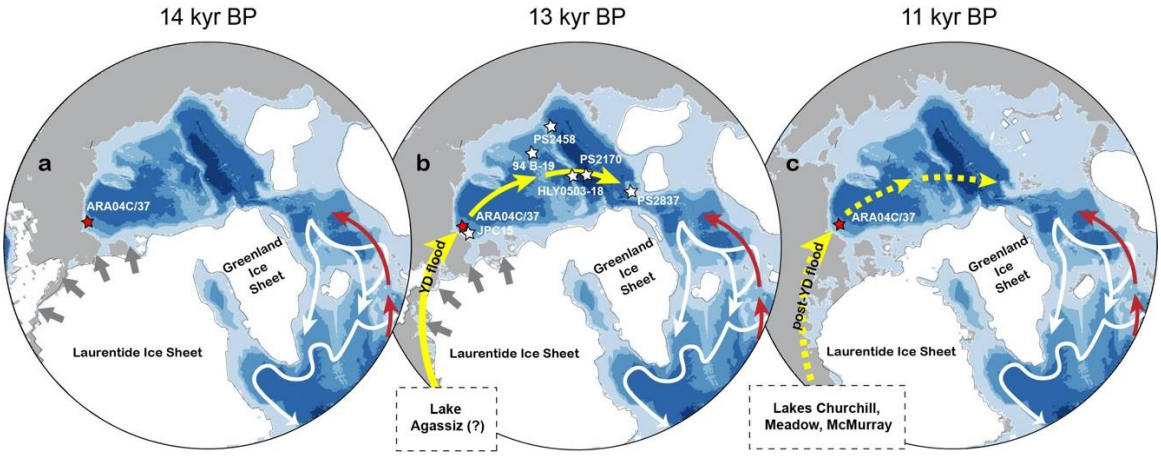

Figure 3.3 Schematic illustrations of ice sheets and flood events during the deglacial to Holocene transition. a Northern Hemisphere ice-sheet extent at 14 kyr BP. **b** YD flood event at ca. 13 kyr BP. Yellow arrows indicate the possible route of YD flood (Broecker, 2006). White stars indicate the studied cores representing the YD flood (Fahl and Stein, 2012; Keigwin et al., 2018; Nørgaard-pedersen et al., 2003; Not and Hillaire-Marcel, 2012; Poore et al., 1999; Spielhagen et al., 2005; Stein et al., 1994a) (discussed in text). **c** post-YD flood event at ca. 11 kyr BP. Dashed yellow arrows show the possible route of post-YD flood from Lake Churchill, Meadow and McMurray (Fisher et al., 2009). In **a-c**, red stars indicate location of Core ARA04C/37, and gray arrows show the melting of the LIS. Red and white arrows represent the warm Atlantic inflow to the Nordic Sea and the main bottom currents. Ice-sheet extent (white areas) outlined in a-c is according to Peltier et al. (2015).

Today, the Mackenzie River is the largest fluvial source of water and sediment into the Beaufort Sea, characterized by water discharge of 316 km^3 yr^{-1} and sediment flux of 124-128 Mt yr^{-1} (Fig. 3.1 and Fig. 3.2) (Holmes et al., 2002). Since the drainage system was established during the late Wisconsinan (i.e., Marine Isotope Stage 2) as a result of glacial erosion, it was an outlet of glacial meltwater during the last deglaciation (Duk-Rodkin and Hughes, 1994). During this period, a cold episode known as YD coincides with a significant reduction of AMOC caused by increased freshwater flux into the North Atlantic deep-water formation region (McManus et al., 2004). The freshwater discharge has been linked to an outburst from the Lake Agassiz, and there is an ongoing debate about the pathway of this freshwater discharge, i.e., whether it drained first into the Arctic Ocean and then to the Atlantic Ocean or whether it drained directly into the Atlantic Ocean (Broecker et al., 1989; Keigwin et al., 2018; Leydet et al., 2018; Peltier et al., 2006) (Fig. 3.3). More recently, field data indicate the freshwater of Lake Agassiz could not drain northward during the YD (Fisher and Lowell, 2012), while model simulations suggest the meltwater drainage via Mackenzie River (northwestern outlet) as a competitive candidate triggering the YD cooling (Peltier et al., 2006; Tarasov and Peltier, 2005). Following the

YD cold period, field data from the Fort McMurray and the Mackenzie Delta point to a post-YD flood from proglacial lakes which drained through the Mackenzie River to the Arctic Ocean during the early Holocene (Fisher et al., 2009; Murton et al., 2010). The timing of the flood coincides with the Preboreal Oscillation (PBO) and thus it has been proposed as the trigger of PBO (Fisher et al., 2002). Above-mentioned events are of significance to climate change but corresponding marine records are scarce. Therefore, high-resolution records are needed to identify these events and the timing of their inception.

Here, we apply a biomarker approach on a well-dated sediment core from the Beaufort Sea directly off the Mackenzie River (Fig. 3.1), covering the time interval of the last deglaciation and the Holocene. Multiple biomarker proxies are used to reconstruct the changes in sea ice, sea surface temperature (SST), primary productivity, and terrigenous input. Based on our records, we demonstrate that (1) the Beaufort Sea region was nearly ice-free with variable SSTs during the last deglaciation and the early Holocene, (2) sea-ice cover developed during the mid-late Holocene, coinciding with a drop in terrigenous sediment flux, SST and primary production, and (3) two major events, characterized by prominent maxima in sediment flux, occurred at 12.83±0.15 and ca. 11 kyr BP. Whereas the former is related to the YD flood event, the origin of the second event is related to a post-YD flood and/or coastal erosion.

3.2 Results

3.2.1 Chronology and approach

Core ARA04C/37 was recovered during the 2013 Araon Cruise ARA04C (Jin, 2013) at the Beaufort Sea continental slope off the Mackenzie River (70°38.0212'N, 139°22.0749'W; 1173 m) (Fig. 3.1), an area characterized by high sedimentation rates. The highest sedimentation rates occur at the Mackenzie Trough (~40–320 cm kyr^{-1}) as well as the continental shelf and slope nearby (~100–200 cm kyr^{-1}) (Gamboa et al., 2017, and references therein).

The chronology of Core ARA04C/37 was constrained by accelerator mass spectrometry (AMS) ^{14}C dating on calcareous foraminifera (planktic and mixed species; Fig. 3.4a, Supplementary Table 3.1, see methods) and, in the uppermost centimeters, excess ^{210}Pb. The age-depth model is established by a combination of AMS^{14}C dates of cores ARA04C/37 and JPC15 (Keigwin et al., 2018) (Fig. 3.4), based on the good correlation of AMS^{14}C dates and magnetic susceptibility (Fig. 3.4a, 3.5a-b) from both cores (see methods). Ages in this paper are provided as calendar years BP. The age-depth relation reveals a mean sedimentation rate of 27 and 100 cm kyr^{-1} in the upper and lower 300 cm, respectively, with high sedimentation rates in two layers near 13 kyr BP (450-500 cmbsf) and 11 kyr BP (295-375 cmbsf). The core represents the deglacial to Holocene transition in high resolution, including the B/A and YD intervals. This enables reconstructions of sea ice, primary productivity, SST, and freshwater discharge in the Beaufort Sea, with special emphasis on the flood events during the transition, in great detail.

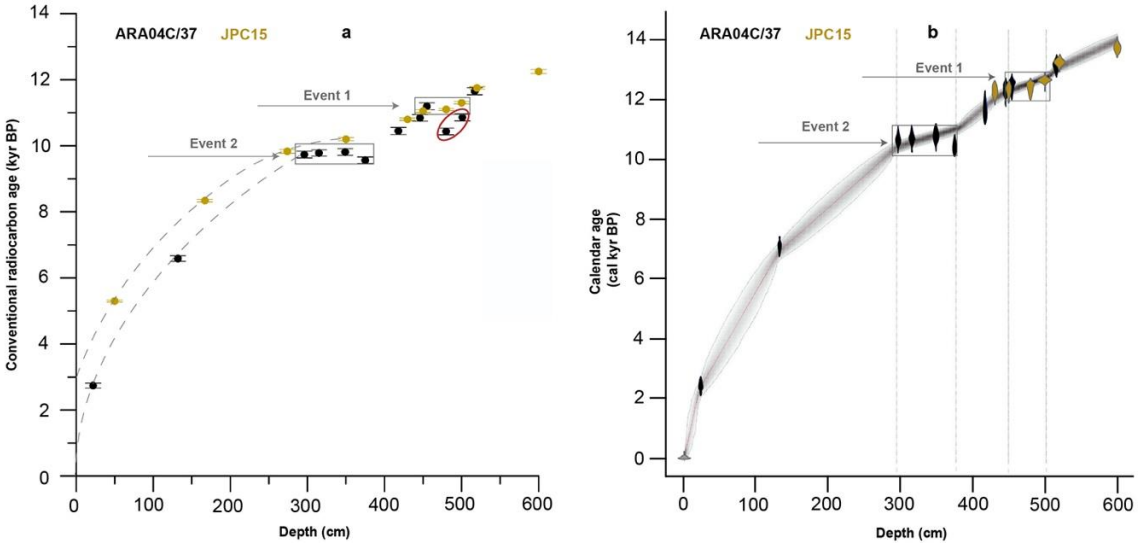

Figure 3.4 Chronology. a uncalibrated AMS14C dates of Core ARA04C/37 (black dots) and Core JPC15 (brown dots) (Keigwin et al., 2018). The vertical error bars represent the 1 sigma analytical errors. Blue boxes mark two intervals characterized by nearly constant ages, possibly related to two events. Red circle shows the excluded "outliers" of Core ARA04C/37. **b** age-depth model based on Bacon (Blaauw and Christeny, 2011) combines 10 AMS^{14}C dates from Core ARA04C/37 (black) and 6 AMS^{14}C dates from Core JPC15 (brown) (Keigwin et al., 2018).

The sea-ice biomarker IP_{25} (Belt et al., 2007; Brown et al., 2014) in combination with open-water phytoplankton biomarkers (e.g., dinosterol), the so-called "PIP_{25}" index, allows semi-quantitative reconstructions of sea-ice concentrations (e.g., Müller et al., 2011; Smik et al., 2016b). The newly developed ring index (RI-OH') of hydroxylated isoprenoid glycerol dialkyl glycerol tetraethers (OH-GDGTs) has been used as a potential tool to reconstruct SST in cold environments (ca. <15 °C) (Lü et al., 2015). The biomarkers brassicasterol and dinosterol are indicators for marine phytoplankton, whereas β-sitosterol and campesterol are indicators for terrigenous input (Fahl and Stein, 2012, 1999; Volkman, 1986). The brassicasterol in some settings has significant sources from freshwater (Rampen et al., 2010; Volkman, 1986) which is the case in our study (discussed below), and we focus on dinosterol to reconstruct marine primary production (Supplementary Fig. 3.1a-b). The branched GDGTs (b-GDGT) are indicative for terrestrial input (Blaga et al., 2010; De Jonge et al., 2014; Hopmans et al., 2004; Weijers et al., 2007), and the $F_{C32\ 1,15}$ index (fractional abundance of C_{32} 1,15-diol) is indicative for aquatic riverine input as the C_{32} 1,15-diol is found particularly abundant in freshwater systems (de Bar et al., 2016; Lattaud et al., 2017a, 2017b; Zhang et al., 2011). More details can be found in the method section.

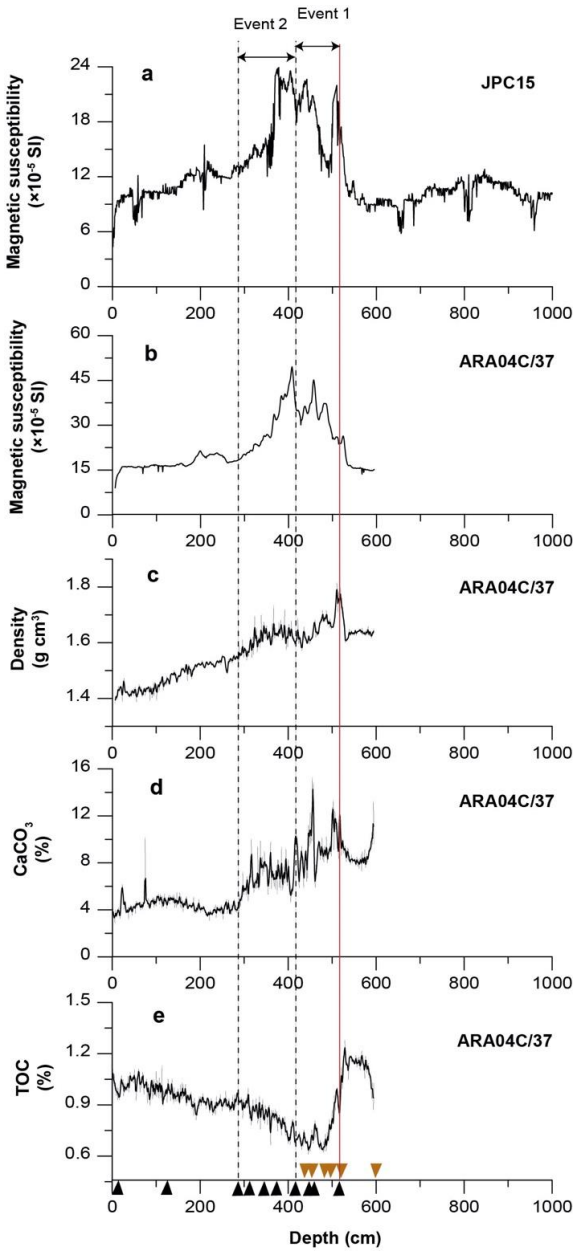

Figure 3.5 Physical properties and chemical records showing two major events. a magnetic susceptibility from Core JPC15 (Keigwin et al., 2018). **b-e** exhibit records from Core ARA04C/37, (**b**) magnetic susceptibility, (**c**) density, (**d**) CaCO3 content (see methods), I TOC content. The vertical lines and horizonal arrows indicate the range of depth recording the two major events. The red vertical line also aligns the same AMS14C dates from both cores, which indicates a good age constraint of magnetic susceptibility rise. Triangles refer to AMS14C dates used in the age-depth model, black triangles from Core ARA04C/37 (this study) and brown triangles from Core JPC15 (Keigwin et al., 2018).

3.2.2 Deglacial-Holocene changes in sea ice and primary production

During the deglaciation and the early Holocene (~14-8 kyr BP), minimum concentrations of IP_{25} (close to the detection limit) and low PIP_{25} values point to dominantly ice-free conditions (Fig. 3.6a and Fig. 3.7c, Supplementary Fig. 3.1c). In such a situation, open-water conditions would be expected to promote primary production. However, concentrations of dinosterol (1-5 µg $gTOC^{-1}$) were low to moderate, implying low primary production during the B/A interstadial (Fig. 3.6c). This may be explained by the fact that the Beaufort Sea itself is an oligotrophic system (Mundy et al., 2009), and the Bering Strait was still closed at that time (>13 kyr BP), hence preventing the inflow of nutrient-rich Pacific Water (Jakobsson et al., 2017; Pico et al., 2020).

Primary productivity shortly increased during the early YD (Fig. 3.6c and Fig. 3.7e), probably promoted by higher nutrient levels supplied by the YD flood (see below). In the early Holocene, the primary productivity experienced a rapid increase at ca. 11 kyr BP as well as subsequent moderate increases during the early Holocene (Fig. 3.7e), possibly caused by high terrigenous input (including nutrients) and the total inundation of Bering Strait respectively (Pico et al., 2020). Furthermore, maximum summer insolation (Laskar et al., 2004) may have caused shorter sea-ice seasons at the core site. More open waters and longer duration of ice-free conditions were favorable for dinosterol production in spring and summer.

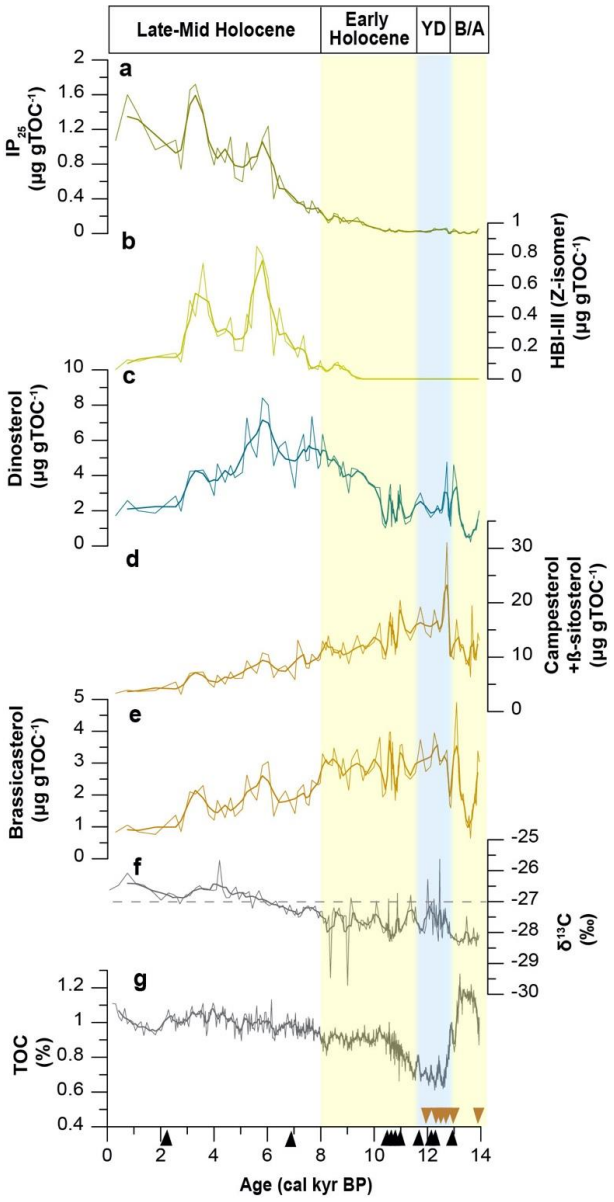

Figure 3.6 Biomarker concentrations (in µg·g TOC^{-1}) and bulk parameters. a IP_{25}, **b** HBI-III (Z-isomer), **c** dinosterol, **d** terrigenous biomarker (campesterol + β-sitosterol), **e** brassicasterol, **f** $\delta^{13}C$ values of TOC (‰), **g** TOC content (%). Triangles refer to AMS^{14}C dates used in the age-depth model (see Figure 3.5).

During the mid-late Holocene (8-0 kyr BP), sea ice expanded, as evidenced by elevated IP_{25} and PIP_{25} values (Fig. 3.6a and Fig. 3.7c), which reveals an evolution from dominantly ice-free conditions (PIP_{25} <0.2) to more extended ice-cover conditions (PIP_{25} >0.8) due to decreasing summer insolation. In turn, expanded sea-ice cover and longer sea-ice duration reduced primary production since the middle Holocene (ca. 8-2.5 kyr BP) as clearly reflected in decreased dinosterol accumulation rates (Fig. 3.7e). The TOC-normalized dinosterol concentrations differ from dinosterol accumulation rates during the mid-Holocene, increasing between ca. 8-5 kyr BP (Fig. 3.6c). This is attributed to simultaneous decreases in marine primary production and terrestrial input, due to sea-ice formation and decrease in river discharge, respectively. During this phase, the reduction of terrestrial organic carbon input was probably larger than that of marine organic carbon input, resulting in increased TOC-normalized dinosterol concentrations. During the late Holocene (ca. 2.5-0 kyr BP), an extended sea-ice cover even hindered primary production by limiting light penetration and nutrient release from sea-ice melt (Fig. 3.7c and Fig. 3.7e).

3.2.3 Reconstruction of marginal ice zones

Abundant phytoplankton production is commonly found in marginal ice zones (MIZs). In these regions, melting sea ice releases nutrients and less-saline waters into the surface layer, forming a stable and nutrient-rich environment above the pycnocline, i.e., favorable conditions for algae blooms (Ackley and Sullivan, 1994; Niebauer and Alexander, 1985; Smith. and Nelson, 1985; Strass and Nöthig, 1996).

Dinosterol and HBI-III (Z-isomer) (further referred to as "HBI-III"; see methods), have both been proposed to indicate pelagic algal production. Studies of surface sediments from different polar regions show significant enhancement of HBI-III in the MIZs (Belt et al., 2015; Collins et al., 2013; Ribeiro et al., 2017; Smik et al., 2016a), while no significant difference in abundances or distributions of phytoplankton sterols was found between the MIZs and open waters (Belt et al., 2015; Smik et al., 2016a). Thus, the HBI-III has been proposed as a MIZ indicator by these authors. Cross-plots of IP_{25} vs HBI-III show a better correlation than IP_{25} vs dinosterol (Supplementary Fig. 3.1c-d), supporting that HBI-III is closely associated with sea-ice environments. Hence, HBI-III is more or less absent when sea-ice cover is strongly reduced or absent (i.e., between ~9 and 14 kyr BP; Fig. 3.7b-c and Fig. 3.7e). The IP_{25} and HBI-III accumulation rates peaked at ca. 5.6 and 3.5 kyr BP (Fig. 3.7d-e), probably representing two periods of MIZ situations (see details in discussion).

3.2.4 Deglacial-Holocene changes in freshwater discharge

Synchronous changes (Fig. 3.6d-e) as well as the positive correlation (Supplementary Fig. 3.1a) between terrigenous biomarkers (campesterol and β-sitosterol) and brassicasterol suggest that brassicasterol in our record has a mixed source from freshwater and marine algae.

During the last deglaciation and the early Holocene (~14-8 kyr BP), very negative $\delta^{13}C_{org}$ values of –28‰ to –27‰ (Fig. 3.6f), relatively high terrigenous biomarker accumulation rates of 5-20 μg cm^{-2} kyr^{-1} (Fig. 3.7f), and high $F_{C32\ 1,15}$ values up to 0.5 (Fig. 3.7g) all point to high terrigenous input. Relatively warm and wet

environments promoted terrigenous matter transport, and low sea-level conditions resulted in a closer distance of the core site to the river mouth receiving more terrigenous matter. In the mid-late Holocene (8-0 kyr BP), $\delta^{13}C_{org}$ values increased (>–27‰) and terrigenous biomarker accumulation rates decreased to 1 µg cm^{-2} kyr^{-1} (Fig. 3.6f and Fig. 3.7f). Similarly, $F_{C32\ 1,15}$ values decreased to 0.3 (Fig. 3.7g), reflecting a descending river discharge and an increasing distance of the core site to the river mouth (cf., Wagner et al., 2011).

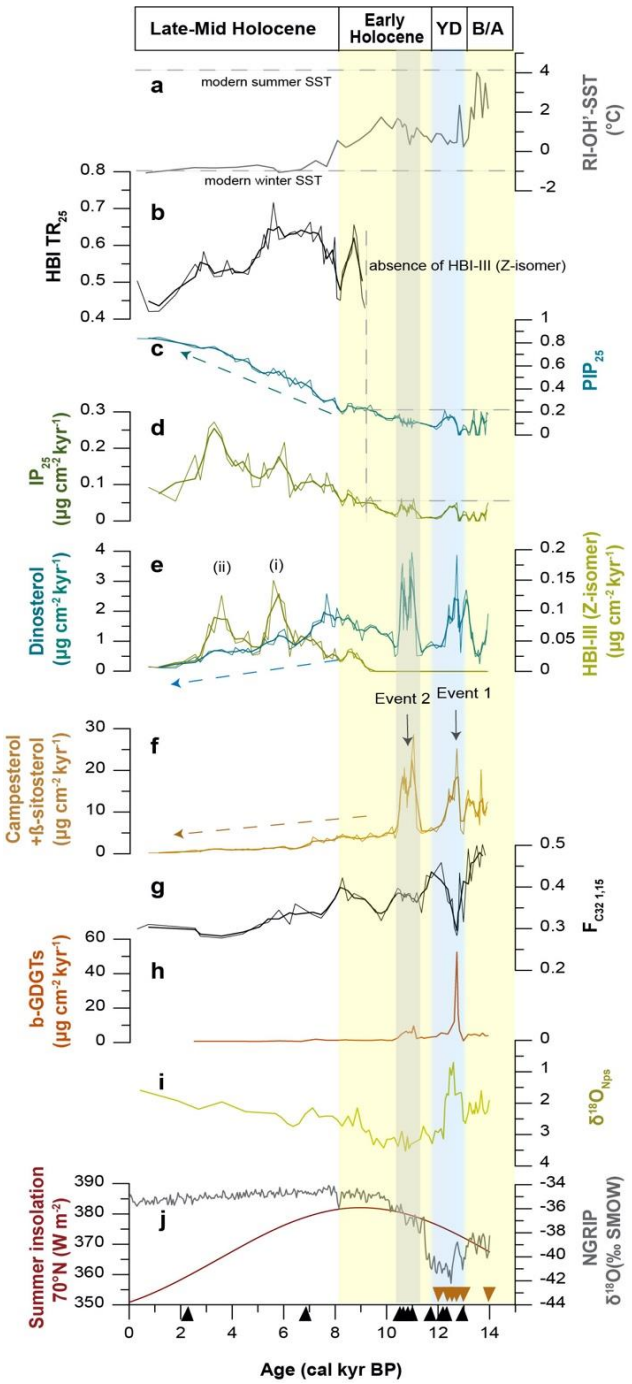

Figure 3.7 Compilation of proxies from Core ARA04C/37 (a-h) and Core JPC15 (i). (**a**) Sea surface temperature proxy RI-OH'-SST; (**b**) spring phytoplankton bloom proxy HBI TR_{25}; (**c**) sea-ice proxy PIP_{25} based on dinosterol; (**d**) IP_{25}; I dinosterol (blue) and HBI-III (yellow); (**f**) terrigenous biomarkers; (**g**) $F_{C32\ 1,15}$, fractional abundance of C_{32} 1,15-diol; (**h**) b-GDGTs; **d-f** are biomarker accumulation rates. **I** $\delta^{18}O$ values of *Neogloboquadrina pachyderma* in Core JPC15 (Keigwin et al., 2018). **j** Summer insolation (grey) (Laskar et al., 2004) and $\delta^{18}O$ values from NGRIP ice core (red) (North Greenland Ice Core Project members, 2004). Triangles refer to AMS^{14}C dates used in the age-depth model (see Figure 3.5).

3.2.5 Sea surface temperature variations

During the deglaciation (~14-11.7 kyr BP), SST values were variable and higher in comparison to the mid-late Holocene SSTs (Fig. 3.7a), indicating relatively warm and open-water conditions. Open-water conditions with less sea ice allowed sufficient heat exchange between ocean and atmosphere. Hence the SST variations followed the global climate history recorded in the Greenland ice core (North Greenland Ice Core Project members, 2004) (Fig. 3.7a and Fig. 3.7j), with typical higher RI-OH'-SST values in the B/A interstadial and lower SST values during the YD stadial (Fig. 3.7a). In the early Holocene (11.7-8 kyr BP), RI-OH'-SST values rose again (Fig. 3.7a), most likely attributed to the summer insolation maximum. Additionally, the total inundation of the Bering Strait occurred at ca. 11 kyr BP and the Pacific Water inflow may have contributed warm water to this site (Pico et al., 2020). In the mid-late Holocene (8-0 kyr BP), RI-OH'-SST values were quite low and stable (Fig. 3.7a), reflecting expanded/seasonal sea-ice conditions in the mid-late Holocene (Fig. 3.7c).

3.2.6 Major sediment flux events at 13 and 11 kyr BP

Two distinct peaks at ca. 13 and 11 kyr BP are found in the accumulation rates of terrigenous biomarkers, dinosterol, and bulk sediment (Fig. 3.7e-f, Supplementary Fig. 3.2). The first peak may reflect the YD flood event (cf., Keigwin et al., 2018) characterized by input of large amounts of terrigenous material and nutrients into the Beaufort Sea. Accumulation rates of terrigenous biomarkers β-sitosterol and campesterol as well as b-GDGTs started to increase at 12.83±0.15 kyr BP (Fig. 3.7f and Fig. 3.7h), close to the onset of Beaufort Sea freshening (12.94±0.15 kyr BP) estimated by Keigwin et al. (2018). The YD flood transported large amounts of heterogeneous sediments into the Beaufort Sea and resulted in increases in magnetic susceptibility, density, and (probably detrital) $CaCO_3$ contents (Fagel et al., 2014; Not and Hillaire-Marcel, 2012) (Fig. 3.5b-d). These sediments were most probably non-biogenic/organic and thus have caused a significant decrease of TOC content (Fig. 3.5e and Fig. 3.6g, Supplementary Fig. 3.2). Such changes in physical and chemical properties occurred slightly before the YD flood, probably attributed to culminated meltwater production in the northwestern outlet area at the end of B/A.

In the earliest Holocene, an even stronger peak in terrigenous input occurred (Fig. 3.7f) at ca. 11 kyr BP. High heterogeneous sediment flux resulted in similar characteristics as caused by the YD event (Fig. 3.5b-e). Although the second event is characterized by high sediment flux and coincides with the post-YD flood, its origin could not be unambiguously proven yet. The second event may have partially different sediment sources from the YD event (see discussion below).

3.3 Discussion

Core site ARA04C/37 is particularly sensitive to changes in paleo sea-ice cover, because it is located in the area of modern seasonal sea-ice cover (Fig. 3.2). In contrast to a foraminifera-based study on the nearby Core

750 that proposed a permanent ice cover during the last deglaciation (14-11.5 kyr BP) (Scott et al., 2009), the records of PIP_{25} and RI-OH'-SST in Core ARA04C/37 clearly point to open-water conditions that allowed heat exchange with the atmosphere (Fig. 3.7a and Fig. 3.7c). Additionally, the minor differences of ^{14}C ages between planktic and benthic foraminifera (Supplementary Table 3.2) indicate that the surface and bottom water masses were relatively well ventilated, further corroborating the scenario of ice-free conditions during the last deglaciation. During the early Holocene, on the other hand, both the foraminifera study (Scott et al., 2009) and our biomarker records (Fig. 3.7c) display more open-water conditions in comparison to the modern Beaufort Sea.

The Beaufort Sea itself is an oligotrophic system6 and the nutrient-rich Pacific Water inflow is an important nutrient source stimulating primary productivity. Studies (foraminifera, geochemical and geophysical data) from sediment cores suggest an initial opening of Bering Strait at about 11.5 kyr BP (Hill and Driscoll, 2008; Jakobsson et al., 2017; Keigwin et al., 2006) whereas other evidence based on marine species dispersal suggests an earlier connection at about 13.3 kyr BP (Dyke et al., 1996; Dyke and Savelle, 2001; England and Furze, 2008). These contradictory evidences are recently reconciled by a gravitationally self-consistent sea-level simulation (Pico et al., 2020). The authors predict the first opening of Bering Strait with shallow inundation at ca. 13 kyr BP. Substantial melting of the Cordilleran Ice Sheet and western Laurentide Ice Sheet (LIS) may have resulted in a local sea-level stillstand during 13-11.5 kyr BP, and then the total inundation of the Bering Strait occurred until ca. 11.5 kyr BP (Pico et al., 2020). Primary production in our records remained relatively low during the deglacial to Holocene transition and generally increased from the early Holocene, except for two rapid increases triggered by high terrigenous input (Fig. 3.7e and Fig. 3.7f). It implies that even if the Bering Strait opened at 13 kyr BP, probably because of its shallow inundation, the Pacific Water influence on primary production in the southern Beaufort Sea was small. Upon the total inundation of the Bering Strait at the early Holocene, primary production started to increase, reflecting more influence of Pacific Water inflow.

HBI-III has been proposed as an indicator for MIZ (Belt et al., 2015; Collins et al., 2013; Ribeiro et al., 2017; Smik et al., 2016a). Among these studies, a study of surface sediments from the Barents Sea found that HBI-III maxima are correlated with the winter ice edge and thus proposed HBI-III as an indicator for winter MIZ (Belt et al., 2015). This is challenged by a study from the East Greenland shelf where an enhancement of HBI-III was observed near the mid-July ice edge in an East Greenland fjord (Ribeiro et al., 2017). The difference in seasonality is controlled by the general sea-ice situations in both areas. Major parts of the Barents Sea are more or less ice-free during late spring, summer and autumn, and thus the ice edge is restricted to the cold/winter season. Along the East Greenland continental margin controlled by the East Greenland Current, on the other hand, sea ice is much more extended throughout the year and thus, the ice edge is more restricted to the summer season.

In our case, HBI-III production was enhanced twice during the Holocene (Fig. 3.7e). In the early Holocene, i.e., prior to the first HBI-III peak, it was nearly ice-free throughout the year, reflected in very low PIP25 values <0.2 and variable SSTs (Fig. 3.7a and Fig. 3.7c). Then, a general trend towards an increasing sea-ice cover is coinciding with weakened insolation (Fig. 3.7c and Fig. 3.7j). Due to sea-ice expansion, the core site was first

proximal to a MIZ situation during cold seasons, when HBI-III peaked at ca. 5.6 kyr BP (Fig. 3.7e). The interval between the two HBI-III peaks (ca. 5-4 kyr BP) characterized by a clear decrease in HBI-III probably represents seasonal sea-ice conditions. As sea ice further expanded, the second period of MIZ may have existed during warm seasons at ca. 3.5 kyr BP, shown by peaked HBI-III (Fig. 3.7e). During the last 2.5 kyrs, reduced HBI-III and dinosterol production (Fig. 3.6b-c and Fig. 3.7e) implies a more extended ice cover. Sea-ice variability is illustrated in Figure 3.8.

A novel proxy HBI TR_{25} shows strong associations with the satellite-derived spring chlorophyll *a* concentration in the Barents Sea, and thus has been proposed as a spring phytoplankton bloom proxy (Belt et al., 2019). Although the proxy is restricted to a regional area, the HBI TR_{25} determined in Core ARA04C/37 seems to support our reconstruction of the MIZ history and by this the applicability of the proxy. Higher values of HBI TR_{25} may point to enhanced occurrence of spring blooms between 8 to 5 kyr BP, indicating that the core site was relatively ice-free in spring. Hence, a winter MIZ may have existed at certain times within this period. On the other hand, lower values of HBI TR_{25} may suggest reduced numbers of spring blooms from 5.6 kyr BP to present. One of the explanations is the existence of a spring sea-ice cover which may have limited the spring blooms. This coincides with the expanding sea-ice cover and longer sea-ice duration during this time interval. To some extent, a summer MIZ may have existed occasionally within this period. These scenarios are in agreement with the HBI-III record suggesting that the core site was probably close to a winter MIZ at ca. 5.6 kyr BP and to a summer MIZ at ca. 3.5 kyr BP.

The changes in RI-OH'-SST values seem to correlate with changes in sea-ice concentrations. That means quite high but variable temperatures occurred during dominantly ice-free periods while low but stable temperatures during ice-covered periods (Fig. 3.7a and Fig. 3.7c), suggesting the proxy's potential as a tool for temperature reconstruction in the Arctic Ocean. To our knowledge, the RI-OH'-SST proxy was first studied on surface sediments from the Chinese coastal seas and the Yangtze Estuary, and then a global surface sediment compilation was assessed (Lü et al., 2015). Samples from northern high latitudes are mainly collected from the Fram Strait (Fietz et al., 2013). In these samples, residual SSTs derived from RI-OH'-SST minus remote sensing SST, are relatively small but generally above zero. Therefore, the absolute values should still be interpreted with caution. Nevertheless, based on the close association between the RI-OH'-SSTs and the sea-ice concentrations, we propose that the proxy most likely reflects winter/spring SSTs in the southern Beaufort Sea. Low and stable SSTs during the seasonal sea-ice periods (mid-late Holocene) (Fig. 3.7a and Fig. 3.7c) suggest that RI-OH' may record SST in the ice-covered seasons, likely in winter. As insolation declined in the mid-late Holocene, ice-covered seasons might have prolonged and persisted into early spring.

Superimposed on the long-term changes in sea ice, primary production, terrestrial input, MIZ, and SST are two extremely high sediment flux events during the deglacial to Holocene transition (at ca. 13 and 11 kyr BP), which are related to the YD flood and the post-YD flood events.

The YD cooling event (12.9-11.7 kyr BP) was the longest interruption to the gradual warming of the climate since the severe Last Glacial Maximum (Fig. 3.7j). Meltwater of LIS draining through the Arctic Ocean to the Nordic seas has been suggested to have profound impacts on slowing down the AMOC and triggering the YD

cooling (Peltier et al., 2006; Tarasov and Peltier, 2005). Glacial system modeling, and seismic reflection data as well as physical properties from the Beaufort slope, show massive floods possibly via a northwestern outlet into the Arctic Ocean at the onset of the YD (Klotsko et al., 2019; Tarasov and Peltier, 2005) (Fig. 3.3). Recently, Keigwin et al. (2018) provided initial freshening evidence of the southern Beaufort Sea. Core JPC15 recorded the freshening in a decrease of $\delta^{18}O$ of the planktic foraminifera *Neogloboquadrina pachyderma* by at least 1‰ at the start of the YD (Fig. 3.7i). In a pilot work, paleosalinity reconstruction from $\delta^{2}H$ of palmitic acid in the same region (Core PS72/291-2; Fig. 3.1) shows a significant reduction of salinity directly prior to the YD (Sachs et al., 2018b). Other evidence, e.g., decreased $\delta^{18}O$ values of planktic foraminifera found in the Laptev Sea, Yermak Plateau, Amundsen Basin, and Mendeleev Ridge (Nørgaard-pedersen et al., 2003; Poore et al., 1999; Spielhagen et al., 2005; Stein et al., 1994a), a prominent increase in sea-ice cover in the Laptev Sea continental margin (Fahl and Stein, 2012), and a pulse in detrital dolomitic-limestones (Arctic-Canadian sediment source) in the central Arctic Ocean (Not and Hillaire-Marcel, 2012), point to a YD-age Arctic freshening sourced from the LIS (Fig. 3.3).

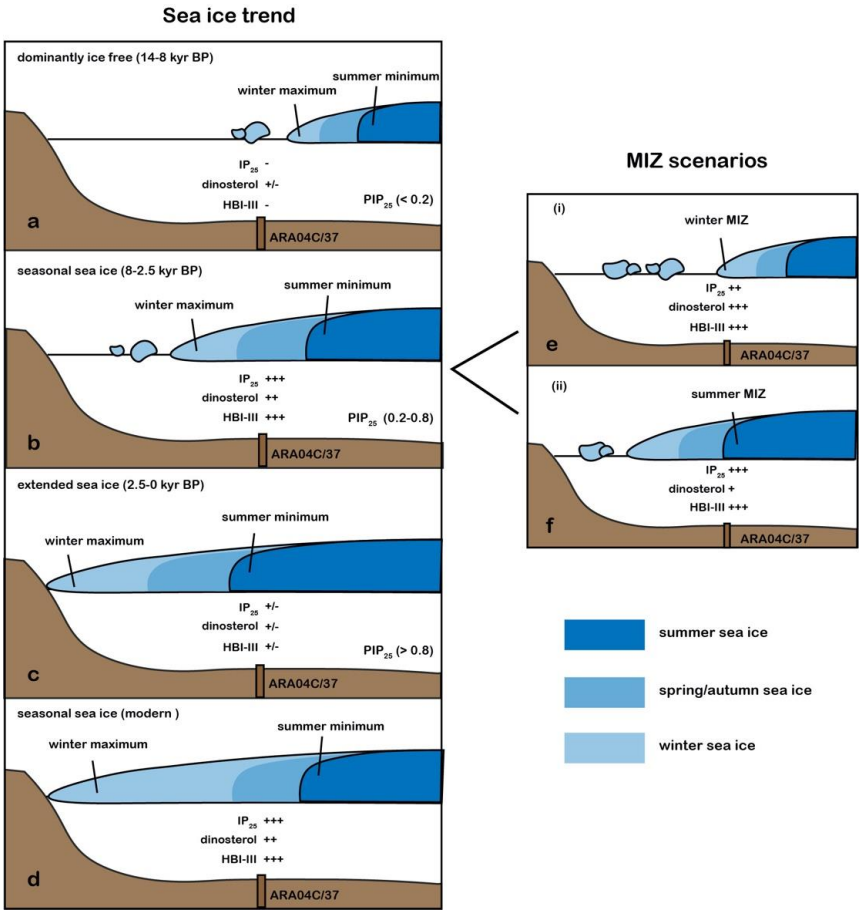

Figure 3.8 Schematic illustration of sea-ice variability in the southern Beaufort Sea. a-c paleo sea-ice variability based on PIP_{25} record, **d** modern sea-ice conditions according to sea-ice concentrations from 1988-2007 (see Fig. 3.2). **e-f** show the winter and summer MIZ conditions of seasonal sea ice.

Meltwater production from the northwestern sector of the LIS might be a component causing the Beaufort Sea freshening. Model simulation suggests that runoff to the Arctic Ocean from melting Keewatin Dome alone was sufficient to slow down the AMOC during YD (Tarasov and Peltier, 2005). Thus, it is possible that such melting culminated at the end of the B/A and strengthened freshening. This is supported by changes in physical properties of Core ARA04C/37 that slightly predated YD (Fig. 3.5). Another possible freshwater component is the outburst from proglacial or subglacial lakes, such as Lake Agassiz. Our multiple biomarker records also document this YD event and suggest the freshening was more related to a flood event as outlined in the following (Fig. 3.5 and Fig. 3.7).

B-GDGTs are synthesized by bacteria and can be found in numerous terrestrial settings, e.g., soils, lakes, and rivers (Blaga et al., 2010; De Jonge et al., 2014; Hopmans et al., 2004; Weijers et al., 2007). As freshly deglaciated surfaces probably have negligible soil organic matter, the increase of b-GDGTs at the onset of YD does likely not indicate input from soils. On the other hand, increase of meltwater in the rivers would not increase the b-GDGTs production. Hence the main contribution of the b-GDGTs increase seems not from the rivers. Another possible source could be from the melting ice sheet, i.e., the b-GDGTs might have been entrained into the base of the ice sheet when it glaciated and were released when it deglaciated. However, such release and accumulation of b-GDGTs should be continuous processes. The sharp increase and peak accumulation of b-GDGTs at the start of YD (Fig. 3.7h) point to lakes as the most probable source. In such lakes b-GDGTs could have been accumulated in a relatively stable environment for a long time and then been delivered to the Beaufort Sea within a short period.

This interpretation is supported by the riverine input proxy $F_{C32\ 1,15}$ (fractional abundance of C_{32} 1,15-diol). The C_{32} 1,15-diol is found particularly abundant in freshwater systems (Zhang et al., 2011), and its production has been related to flow regimes (Häggi et al., 2019). A study from the Amazon River shows that the highest abundance of C_{32} 1,15-diol exists in water bodies with low flow velocity and low turbidity, while the lowest abundance of C_{32} 1,15-diol is found in conditions with high turbidity and high flow velocity (Häggi et al., 2019). This suggests that a high-velocity flow regime like a flood producing higher turbidity would limit the C_{32} 1,15-diol production. Thus, the significant drop in $F_{C32\ 1,15}$ values during the YD (Fig. 3.7g) characterizes a flood event of high erosive power and high flow velocity in turbid waters.

Assuming that the high-resolution terrestrial records of Core ARA04C/37 represent the YD flood event, a duration was estimated based on records of terrigenous sterols and b-GDGTs (Fig. 3.6d and Fig. 3.7h). The peak discharge started at 12.78±0.15 kyr BP and ended up at 12.63±0.13 kyr BP, resulting in a flood duration of about 150 years. Such estimate is close to the duration of 130 year estimated by Keigwin et al. (2018).

Although our biomarker records in combination with previous paleo-salinity reconstructions (Keigwin et al., 2018; Sachs et al., 2018b) indicate a strong YD flood, the flood water source still remains unclear. Coinciding with the YD event, a large lake-level drop of Lake Agassiz (with an estimated freshwater release of ~17,000 km^3) (Breckenridge, 2015) has been proposed as the freshwater source (Murton et al., 2010). According to more recent studies, however, no clear field evidence (ice margins or shorelines) supports that Lake Agassiz

drained to any northwestern outlet before 10.8-10.1 kyr BP (Fisher et al., 2009; Fisher and Lowell, 2012). It cannot be excluded that the northwestern outlet of Lake Agassiz opened at an earlier phase and its evidence has been removed by a re-advance of LIS. Otherwise, the flood may have other water sources, e.g., outburst from further northern proglacial/subglacial lakes. If so, the freshwater discharge from these lakes alone was too small to trigger the YD cooling. Besides freshening in the Beaufort Sea, input of freshwater during the YD was also found in the Northeast Pacific sea (Praetorius et al., 2020, and references therein). A recent model simulation suggests that if the Bering Strait partially opened at the start of YD (Pico et al., 2020), some of the freshwater from the Northeast Pacific could be transported through the Arctic Ocean to the Nordic seas, contributing to a collapse of the AMOC (Praetorius et al., 2020).

In the earliest Holocene, following the YD flood, a post-YD flood at ca. 11.3 kyr BP has been identified by field data from the Fort McMurray area, and the freshwater source is suggested to derive from proglacial lakes McMurray, Meadow, and Churchill (Fisher et al., 2009). Evidence in the Fort McMurray region is in line with field data from the Mackenzie Delta supporting that a second high-energy fluvial episode occurred in the delta between 11.7 and 9.3 kyr BP (Murton et al., 2010). More recently, seismic and geophysical data from the Beaufort margin also indicate that the second event probably initiated at ca. 11.3 kyr BP (Klotsko et al., 2019). The timing of the second flood coincides with the PBO, thus it has been proposed that the second flood may have triggered the PBO (Fisher et al., 2002; Klotsko et al., 2019). As a large amount of freshwater from the Baltic Ice Lake entered the Arctic marginally predating the PBO (Boden et al., 1997), Klotsko et al. (2019) regarded the second flood injection as a tipping point for sufficient weakening of the AMOC during the PBO. Despite the field data indicate a second flood, direct evidence for freshwater input is still missing from the marine records. The $\delta^{18}O$ record of Core JPC15 shows minimum values only during the YD flood, whereas values were even higher than the 2‰ baseline during the second event (Keigwin et al., 2018) (Fig. 3.7i). A similar case was described for a piston core from the Mackenzie Trough (Schell et al., 2008), where a coarse-layered unit was dated to 11.5 to 11.3 kyr BP while the very positive oxygen isotope values (~2.7-3.5‰) argued against the hypothesis of an outburst from proglacial lakes. So far, the only freshwater evidence is found in Core P189AR-P45 (see Fig. 3.1 for location), showing a drop of $\delta^{18}O$ values at ca. 11.5 kyr BP (Andrews and Dunhill, 2004). However, since the age-depth model of this core is not well constrained, the timing of the freshwater signal might be shifted to the YD period when improving the age model. In comparison to the YD flood, biomarker records also show slight differences during the second event (Fig. 3.7g-h). Moderate values of $F_{C32\ 1,15}$ during the second event indicate relatively stable flow regimes and smaller discharge than the YD flood (Fig. 3.7g). Otherwise extremely high flow velocity would limit C_{32} 1,15-diol production. Accumulation of b-GDGTs was also much smaller than during the YD (Fig. 3.7h), and seems to have different sources. This evidence gives rise to the question whether the high sediment flux was caused by a flood or whether it was controlled by other processes.

In this context, one should keep in mind that the second event also coincided with global meltwater pulse 1b (MWP 1b). Recent studies in the Okhotsk Sea and Pacific Beringia provided direct evidence of coastal erosion induced by the rapid sea-level rise (Meyer et al., 2019; Winterfeld et al., 2018). In these records, two distinct

maxima of terrigenous material were observed within the rapid sea-level rise at ca. 14 and 11 kyr BP (MWP 1a and 1b). In the Kara Sea, high terrigenous sediment fluxes characterized by significantly increased C/N ratios and refractory organic matter were recorded at about 11 kyr BP and also related to increased coastal erosion due to the post-glacial flooding of the shelf sea (Stein et al., 2003; Stein and Fahl, 2004). In the Labrador Sea, a high-sedimentation layer containing increased detrital carbonates was dated to ca. 11.5-11.3 kyr BP (Pearce et al., 2015). Although the authors related it to "Heinrich event 0", almost simultaneous signals widely found in the Arctic may support the interpretation of sea-level rise induced coastal erosion. It is therefore possible that the high sediment flux during the second event was partially caused by coastal erosion and subsequent deposition of the eroded terrigenous material.

Although field data indicate a second flood during the early Holocene, marine evidence suggests that the high sediment flux could be caused by a meltwater flood and/or shelf flooding induced coastal erosion. Further work, e.g., comprehensive proxy reconstruction of freshwater discharge and paleo-salinity (cf., Sachs et al., 2018b) as well as carbon source constraint (cf., Winterfeld et al., 2018), is hence needed to distinguish different processes.

3.4 Methods

Chronology

Radiocarbon dates of Core ARA04C/37 and JPC15 are consistent during the last deglaciation (Fig. 3.4). A red vertical line is placed close to the onset of the magnetic susceptibility rise (Fig. 3.5a-b), and the almost same ^{14}C ages from both cores at the vertical line suggest a good age constraint of the onset of magnetic susceptibility change. ^{14}C dates from the two cores are highly consistent below 400 centimeters below seafloor (cmbsf) (Fig. 3.4a). However, age offsets are enlarged from near 350 cmbsf towards the core-top (Fig. 3.4a), indicating a weakened correlation between Core ARA04C/37 and JPC15. Therefore, we established the age-depth model for core ARA04C/37 by including 6 AMS^{14}C dates from Core JPC15 below 400 cmbsf (Supplementary Table 3.1). Paired dating shows a mean difference of around 200 years between planktic and benthic foraminifera (Supplementary Table 3.2). Considerable ventilation allows mixed species (planktic and benthic) being used for age constraints. As discussed in detail by Keigwin et al. (2018), ΔR was defined as 200±100 years in YD and 0±100 in the Holocene and B/A in the age model. The age-depth model was developed using the "Bacon" software of Blaauw and Christeny, (2011). Bulk sediments of the top cm of the core were analyzed by gamma spectrometry (HPGe planar detector). Based on excess ^{210}Pb in the uppermost centimeters and detectable anthropogenic ^{137}Cs in the top sample, surface sediments were identified to be modern, therefore the core-top was fixed to 0 kyr BP. Between 450 and 500 cmbsf (unit 1), ^{14}C dates are constant (mean ^{14}C age of 11160 years) and are indicative for event 1 (Fig. 3.4a). Although the onset of event 1 is better constrained, because there is no clear termination of event 1 shown in magnetic susceptibility, the range of unit 1 is less constrained. This might lead to an over- or underestimate of sedimentation rate. Similarly, despite that magnetic susceptibility in both cores shows generally synchronous changes between 375 and 420 cmbsf (Fig. 3.5a-b),

enlarged age offsets indicate a weaker correlation between the two cores (Fig. 3.4a; Supplementary Table 3.1). Therefore, we define the unit 2 (event 2) mainly based on four constant ^{14}C dates (mean ^{14}C age of 9750 years) between 295 and 375 cmbsf, with poor constraints in both onset and termination of the event. The second high-sedimentation unit (295-375 cmbsf) may be thicker than shown by the four dates, therefore we kept the four dates for more precise age model constraints, even though the last date of the plateau is not strictly increasing (Fig. 3.4). A "boundary" function was applied in the two units which may have experienced distinctively high sedimentation rates (cf., Blaauw and Christen, 2013). All the ^{14}C ages were transformed into calendar ages following the Marine13 curve (Reimer et al., 2013).

Bulk parameters

For organic geochemical analyses, sediment samples were freeze-dried, ground and homogenized. Total organic carbon (TOC) contents were determined by a Carbon-Sulfur Analyser (CS-125, Leco) after decarbonization with hydrochloric acids. Total carbon (TC) contents were analyzed by a Carbon-Nitrogen-Sulfur Analyser (Elementar III, Vario), and used for calculation of carbonate contents ($CaCO_3$=(TC-TOC) × 8.333). Carbon isotope composition of organic matter ($\delta^{13}C_{org}$) was analyzed by means of a Thermo Delta V Isotope Ratio Mass Spectrometer connected to a Thermo Flash 2000 CHNS/OH Elemental Analyzer employing continuous flow, performed at the Korea Polar Research Institute. $\delta^{13}C_{org}$ values are given in per mil notation relative to Vienna Pee Dee Belemnite International Standard. Reference gases were calibrated relative to Indiana University Acetanilide#1, USGS40, Urea and Thermo Soil standards. For a randomly selected set of samples duplicate analyses were carried out to determine the analytical error. Analytical precision is within 0.2‰.

Biomarker analyses

Freeze-dried sediments (5 g) were ultrasonically extracted with DCM:MeOH (2:1, v/v), and internal standards (0.076 µg 7-hexylnonadecane (7-HND) and 10.7 µg 5α-androstan-3β-ol (androstanol)) were added prior to analytical treatment. Total lipid extracts were concentrated and separated via open column chromatography with silica gel (6 mm i.d.*4.5 cm). The lipids were eluted by 5 ml *n*-hexane for hydrocarbon fraction, followed by 9 ml ethyl acetate:hexane (1:4, v/v) for sterol fraction (containing diols). The sterol fraction was further derivatized with 200 µl bis-trimethylsilyl-trifluoracet-amide (BSTFA) (60 °C, 2h). The composition of the hydrocarbons, sterols, and diols was analyzed by gas chromatography (GC)-mass spectrometry (MS) (Agilent 7890GC-Agilent 5977 A). Compounds were identified by comparison of GC retention times with published mass spectra (Belt et al., 2007; Boon et al., 1979; Brown and Belt, 2016; Rampen et al., 2012; Versteegh et al., 1997; Volkman, 1986).

For quantification of the HBIs, their molecular ions (*m/z* 350 for IP_{25}, *m/z* 348 for HBI II, and *m/z* 346 for HBI III) were used in relation to the fragment ion *m/z* 266 (internal standard 7-HND). The sterols, brassicasterol (24-methylcholesta-5,22E-dien-3β-ol), campesterol (24-methylcholest-5-en-3β-ol), β-sitosterol (24-ethylcholest-5-en-3β-ol), and dinosterol (4α,23,24R-trimethyl-5α-cholest-22E-en-3β-ol) were quantified as

trimethylsilyl ethers. Their molecular ions *m/z* 470, *m/z* 472, *m/z* 486, and *m/z* 500 were used in relation to the molecular ion *m/z* 348 of androstanol. External calibration curves (cf., Fahl and Stein, 2012) were applied and specific response factors were calculated for these ions. For quantification of the relative abundance of the diols, the fragment ions *m/z* 313.3 (C_{28} 1,13-diol, C_{30} 1,15-diol) and 341.3 (C_{30} 1,13-diol, C_{32} 1,15-diol) were used.

Reconstruction of sea-ice concentrations (PIP_{25}) followed Müller et al. (2011) (Eq. 1):

$$PIP_{25} = [IP_{25}] / ([IP_{25}] + [\text{Phytoplankton biomarker}]*c) \quad (1)$$

with balance factor c=mean IP_{25} concentration/mean phytoplankton biomarker concentration.

Due to a presumed terrestrial origin of brassicasterol in this region (see results), the calculation of PIP_{25} was based on the pelagic algal biomarkers dinosterol.

The tri-unsaturated HBI biomarkers (triene, Z- and E-isomer) are commonly found in marine sediment. Based on studies in the Barents Sea, HBI-III (Z) producers favor nutrient-rich and stratified upper water column at the ice-edge (Belt et al., 2015). For simplification, the term "HBI-III" is used in the main text, representing the "HBI-III (Z)". The relationship between the relative proportions of HBI-III (Z) and HBI-III (E) and spring chl *a* in surface sediment from the western Barents Sea suggests the potential of a novel HBI proxy (HBI TR_{25}) indicating the spring phytoplankton bloom (Belt et al., 2019) (Eq. 2).

$$\text{HBI } TR_{25} = [\text{Z-triene}] / ([\text{Z-triene}] + [\text{E-triene}]) \quad (2)$$

$F_{C32\ 1,15}$ (fractional abundances of C_{32} 1,15-diol) indicative for aquatic riverine input was calculated based on Eq. (3) (Lattaud et al., 2017b):

$$F_{C32\ 1,15} = [C_{32}\ 1,15] / ([C_{32}\ 1,15] + [C_{30}\ 1,15] + [C_{30}\ 1,13] + [C_{28}\ 1,13]) \quad (3)$$

For the GDGT analyses, 5 g sediment was ultrasonically extracted with DCM:MeOH (2:1, v/v), and internal standard (C_{46}-GDGT, 1 µg per sample) was added prior to analytical treatment. The GDGT fraction was separated from other fractions via open column chromatography and eluted with 5 ml DCM:MeOH (1:1, v/v), dried and re-dissolved in hexane:isopropanol (99:1, v/v), then filtered via a polytetrafluoroethylene (PTEE) filter with a pore size of 0.45 µm. Compound identification and quantification have been carried out by a high-performance liquid chromatography/atmospheric pressure chemical ionization-mass spectrometry (HPLC/APCI-MS) according to the method described by Meyer et al. (2019). The MS-detector was set for SIM of the following (M+H)+ ions: *m/z* 1300.3 (OH-GDGT-0), 1298.3 (OH-GDGT-1), 1296.3 (OH-GDGT-2), 1050 (GDGT-IIIa/IIIa'), 1036 (GDGT-IIa/IIa'), 1022 (GDGT-Ia), and 744 (C_{46} standard), with a dwell time of 57 ms per ion.

Calculation of ring index of hydroxylated tetraethers (RI-OH') and its derived SST follows Lü et al. (2015) (Eq. 4, 5):

$$RI\text{-}OH' = ([OH\text{-}GDGT\text{-}1] + 2*[OH\text{-}GDGT\text{-}2]) / ([OH\text{-}GDGT\text{-}0] + [OH\text{-}GDGT\text{-}1] + [OH\text{-}GDGT\text{-}2]) \quad (4)$$

$$RI\text{-}OH' = 0.0382 * SST + 0.1 \quad (5)$$

Accumulation rates

Accumulation rates of bulk sediment, bulk organic carbon, $CaCO_3$, and biomarkers are calculated by using the following equations (cf., Stein and Macdonald, 2004):

$$BulkAR = SR * (WBD-1.026*PO) \quad (6)$$

$$TOCAR = BulkAR * TOC \quad (7)$$

$$CaCO_3AR = BulkAR * CaCO_3$$

$$BMAR = BulkAR * BM$$

BulkAR = bulk sediment accumulation rate (g cm^{-2} kyr^{-1});

SR = sedimentation rate (cm kyr^{-1});

WBD = wet bulk density (g cm^{-3});

PO = porosity (%);

TOCAR = total organic carbon accumulation rate (g cm^{-2} kyr^{-1});

$CaCO_3AR$ = carbonate accumulation rate (g cm^{-2} kyr^{-1});

BMAR = biomarker accumulation rate (μg cm^{-2} kyr^{-1});

BM = biomarker concentration (μg g^{-1} Sed).

Acknowledgements

We gratefully thank the professional support of the captain and crew of RV Araon on the expedition ARA04C. We thank Shizhu Wang for generating ice sheet maps. Thanks to Simon Belt (University of Plymouth/UK) for providing the 7-HND standard for IP_{25} quantification. We acknowledge support by the Open Access Publication Funds of Alfred Wegener Institute Helmholtz Centre for Polar and Marine Research (AWI) and China Scholarship Council for financial support. This research is also supported by the Basic Core Technology Development Program for the Oceans and the Polar Regions (NRF-2015M1A5A1037243) from the National Research Foundation of Korea funded by the Ministry of Science and ICT.

3.5 Supplementary Information

Supplementary Figures

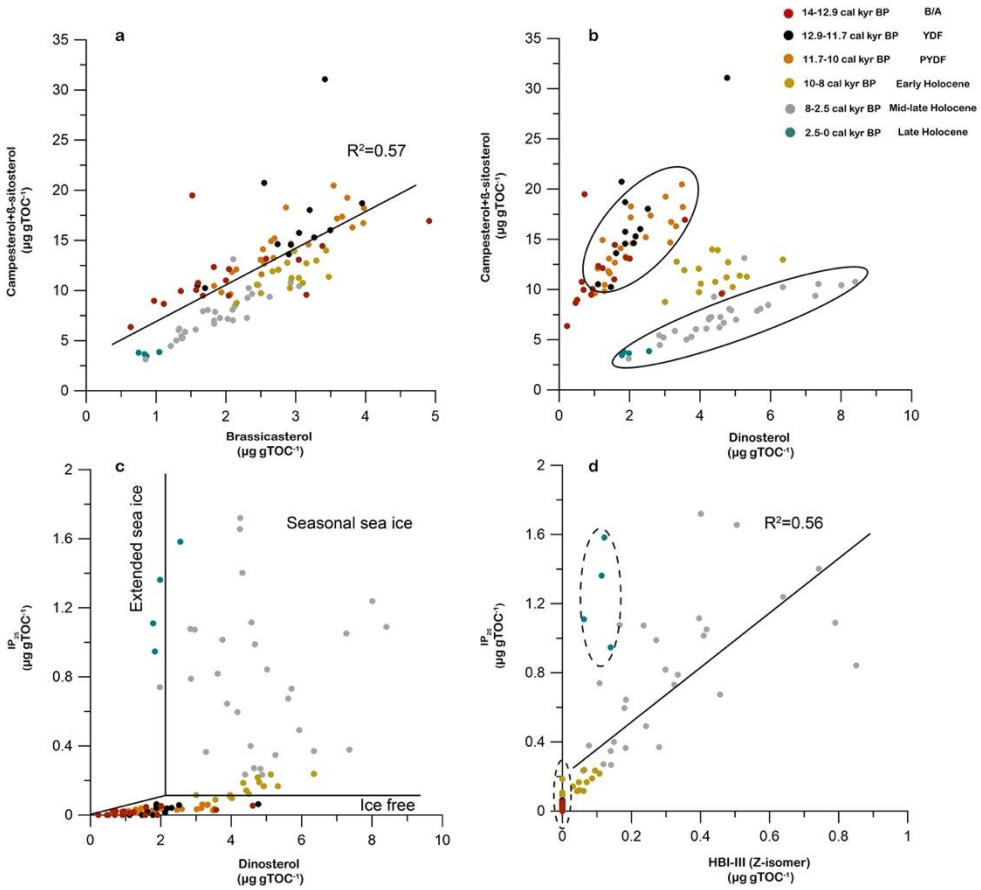

Supplementary Figure 3.1 Correlation between biomarkers. a terrigenous biomarkers (campesterol and β-sitosterol) versus brassicasterol, **b** terrigenous biomarkers versus dinosterol, **c** IP_{25} versus dinosterol, **d** IP_{25} versus HBI-III (Z-isomer). Ellipses in (**b**) highlight samples showing linear relationship between terrestrial sterols and dinosterol. Ellipses in (**d**) highlight samples from extended sea-ice conditions and HBI-III free conditions which may lower the R^2.

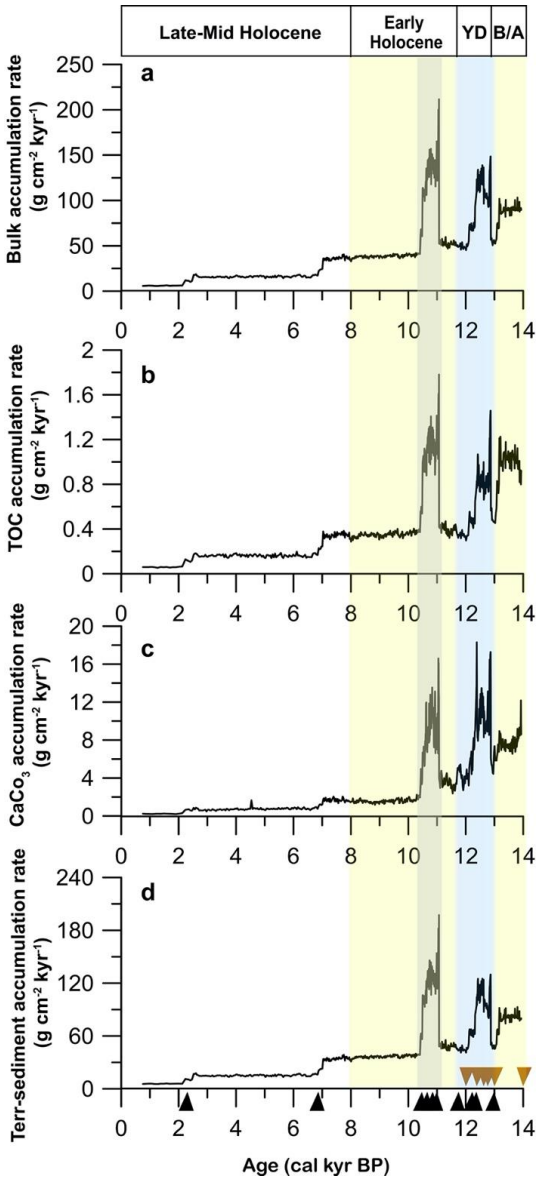

Supplementary Figure 3.2 Accumulation rate of Core ARA04C/37. a bulk accumualtion rate, **b** total organic carbon (TOC) accumulation rate, **c** carbonate ($CaCO_3$=(TC-TOC)×8.333) accumulation rate, **d** terrigenous-sediment accumulation rate (=bulk-TOC-$CaCO_3$).

Supplementary Tables

Supplementary Table 3.1 Chronology of Core ARA04C/37* and additional dates adopted from Core JPC15 (Keigwin et al., 2018)[*]

	Lab ID	Depth (cm)	Species	AMS ^{14}C age (year)	ΔR	Calibrated age** (cal year BP)	Model age*** (cal year BP)
ARA04C/37	AWI-2104.1.1	22	mixed	2738±73	0±100	2469±157	2351±316
	AWI-2261.1.1	132	mixed	6588±86	0±100	7093±149	6942±297
	AWI-2105.1.1	296	planktic	9735±103	0±100	10648±198	10440±205
	AWI-2106.1.1	315	planktic	9782±94	0±100	10711±187	10617±185
	AWI-2107.1.1	349	planktic	9812±99	0±100	10750±189	10859±177
	AWI-2108.1.1	375	planktic	9561±101	0±100	10538±184	11047±177
	AWI-2109.1.1	417	planktic	10450±110	0±100	11615±267	11775±247
	AWI-2110.1.1	445	planktic	10846±102	0±100	12295±213	12260±183
	AWI-2111.1.1	454	mixed	11195±103	200±100	12482±181	12365±162
	AWI-2112.1.1	479[a]	planktic	10434±104			
	AWI-2113.1.1	500[a]	mixed	10861±106			
	AWI-2114.1.1	516	planktic	11652±106	0±100	13121±156	13005±171[b]
JPC15	NOSAMS-134017	430	*Nps*	10800±35	0±100	12262±185	12032±227[b]
	NOSAMS-110672	450	*Nps*	11050±45	200±100	12323±179	12327±166[b]
	NOSAMS-131596	480	*Nps*	11100±30	200±100	12392±160	12586±140[b]
	NOSAMS-123914	500	*Nps*	11300±35	200±100	12621±87	12779±147[b]
	NOSAMS-131597	520	*Nps*	11750±35	0±100	13226±103	13093±180[b]
	NOSAMS-110673	600	*Nps*	12250±60	0±100	13707±142	13997±236[b]

AMS^{14}C dating of Core ARA04C/37 have been carried out at the Alfred Wegener Institute Bremerhaven using the Mini Carbon Dating System (MICADAS).

**calibrated ages (median probability) with 1σ uncertainty, using Calib 7.1 (Stuiver et al., 2020) and based on Marine13 (Reimer et al., 2013).

***model ages (mean) with default 95% confidence ranges based on Bayesian model (Bacon) (Blaauw and Christeny, 2011) and Marine13 (Reimer et al., 2013) in this study

[a]outliers excluded in the age-depth model

[b]recalibrated model ages by Bayesian model (Bacon) (Blaauw and Christeny, 2011) in this study

Supplementary Table 3.2 Paired AMS^{14}C dating of planktic and benthic foraminifera of Core ARA04C/37* and Core JPC15 (Keigwin et al., 2018)

Sediment core	Lab ID	Depth (cm)	Species	AMS ^{14}C age (year)
ARA04C/37	AWI-2105.1.1	296	planktic	9735±103
	AWI-2105.2.1	296	benthic	9717±101
	AWI-2106.1.1	315	planktic	9782±94
	AWI-2106.2.1	315	benthic	9905±100
	AWI-2107.1.1	349	planktic	9812±99
	AWI-2107.2.1	349	benthic	10035±98
	AWI-2108.1.1	375	planktic	9561±101
	AWI-2108.2.1	375	benthic	10244±107
	AWI-2109.1.1	417	planktic	10450±110
	AWI-2109.2.1	417	benthic	10466±107
	AWI-2110.1.1	445	planktic	10846±102
	AWI-2110.2.1	445	benthic	10906±102
	AWI-2114.1.1	516	planktic	11652±106
	AWI-2114.1.1	516	benthic	12021±110
JPC15	NOSAMS-110669	50	*Nps*	5300±30
	NOSAMS-113087	50	*C.neoteretis*	5020±20
	NOSAMS-110670	274	*Nps*	9830±55
	NOSAMS-113088	274	*C.neoteretis*	10100±30
	NOSAMS-110671	350	*Nps*	10200±45
	NOSAMS-113089	350	*C.neoteretis*	10200±30
	NOSAMS-110672	450	*Nps*	11050±45
	NOSAMS-113090	450	*C.neoteretis*	11200±30

* AMS^{14}C dating of Core ARA04C/37 have been carried out at the Alfred Wegener Institute Bremerhaven using the Mini Carbon Dating System (MICADAS).

Supplementary Table 3.3 Key reference cores from the southern Beaufort Sea

Core/site	Latitude (N)	Longitude (W)	Reference
ARA04C/37	70.63°	139.37°	this study
JPC15	71.10°	135.14°	Keigwin et al. (2018)
750	71.20°	134.06°	Scott et al. (2009)
PS72/291-2	71.27°	137.18°	Sachs et al. (2018b)
P189AR-P45	70.55°	141.87°	Andrews and Dunhill (2004)

4. Deglacial exhumation of petrogenic carbon and mobilization of thawed permafrost in the Canadian Arctic and their impact on the carbon cycle

Junjie Wu[1], Gesine Mollenhauer[1,2], Ruediger Stein[1,2], Peter Köhler[1], Jens Hefter[1], Kirsten Fahl[1], Hendrik Grotheer[1], Bingbing Wei[3], Seung-Il Nam[4]

[1]Alfred Wegener Institute Helmholtz Centre for Polar and Marine Research, Am Alten Hafen 26, Bremerhaven 27568, Germany

[2]MARUM—Center for Marine Environmental Sciences and Faculty of Geosciences, University of Bremen, Bremen 28359, Germany

[3]State Key Laboratory of Marine Geology, Tongji University, Shanghai 200092, China

[4]Korea Polar Research Institute, 26 Songdomirae-ro, Yeonsu-gu, Incheon 21990, Republic of Korea

Abstract

Emerging evidence has suggested that ancient terrestrial organic carbon is a significant contributor to deglacial CO_2 rise, but the carbon sources and processes of carbon release remain unresolved. Here, we present novel direct evidence from the Canadian Beaufort Sea for substantial re mobilization of ancient terrestrial carbon during the last deglaciation following the retreat of the Laurentide Ice Sheet and as a consequence of coastal erosion of ancient permafrost deposits. We use radiocarbon dating of bulk organic carbon and terrigenous compounds in concert with multiple thermal maturity proxies as evidence of largely enhanced ancient terrigenous carbon fluxes between 14.5 and 10 kyr BP. We propose that glacial-retreat-induced physical erosion was responsible for the enhanced supply of petrogenic organic carbon and the subsequent oxidation. Remobilization of permafrost carbon at ca. 14 and 11 kyr BP has been attributed to coastal erosion during the rapid sea-level rises. Assessment of carbon release from the two processes indicates that ice-sheet retreat played an important role in contributing terrestrial organic carbon to the deglacial CO_2 rise.

4.1 Introduction

The identification of Earth System processes that have contributed to atmospheric pCO_2 variability since the Last Glacial Maximum (LGM) remains one of the grand challenges in climate science. During the transition from the LGM to the Holocene, atmospheric CO_2 concentrations rose by about 75 ppm while the $\Delta^{14}C$ values of CO_2 declined (Marcott et al., 2014; Monnin et al., 2001; Reimer et al., 2020). It is consensus that the increase in pCO_2 is largely driven by changes in Southern Ocean ventilation, making the region a source of aged carbon to the atmosphere (Anderson and Burckle, 2009). However, the oceanic CO_2 release alone cannot account for the full amplitude of CO_2 rise, or the rapid rise that occurred at 16.4 kyr BP, 14.6 kyr BP, and 11.5 kyr BP, or the stable carbon isotopic anomaly. Thus, both the terrestrial and marine carbon sources have been invoked to collectively explain the CO_2 variations (Bauska et al., 2016; Sigman et al., 2010). A growing number of recent studies have investigated in detail the old terrestrial carbon reservoirs containing organic matter depleted in ^{13}C and ^{14}C. For instance, some initial evidence suggests that flooded and/or thawed permafrost may have contributed substantial amounts of ancient carbon to the deglacial rapid CO_2 rise (Köhler et al., 2014; Martens et al., 2020; Meyer et al., 2019; Winterfeld et al., 2018).

Ice sheets are one of the disregarded components to explain the CO_2 variations, and research in the past decade has refreshed our view of ice sheets as an "inert component". Wadham et al. (2019) has recently assessed the active role of ice sheets which have the potential to impact the carbon cycle by direct and indirect ways, i.e., microbial respiration of organic matter beneath ice sheets (primarily discussed as CH_4 release) and fertilization of ecosystems by nutrient-rich glacial meltwaters. More recently, the oxidation of petrogenic organic carbon (OC_{petro}; defined as mature or immature OC that is derived from sedimentary rocks and depleted in radiocarbon) associated with ice-sheet retreat receives growing attention, and the process has been hypothesized to be a significant CO_2 source during the last deglaciation (Blattmann, 2021).

Modern observations have described OC_{petro} oxidative weathering as a supply-limited process, and rock erosion rate controls its oxidation fluxes (Hilton et al., 2014; Horan et al., 2017). High OC_{petro} supply is found in glaciated regions today, where glacial denudation of bedrocks might be a significant contributor. In the southern Alps of New Zealand, the OC_{petro} oxidative weathering fluxes in glacier-dominated watersheds (up to 50 tC km^{-2} yr^{-1}) are 2-3 times higher than those in less-glaciated watersheds (Horan et al., 2017). Along the southeast Alaskan coast, the mass accumulation rates (MARs) of OC_{petro} in glaciated fjords are significantly higher than those in non-glaciated fjords (Cui et al., 2016). Notably, initial evidence of OC_{petro} mobilization during the ice sheet retreat has been seen in a sediment record of accumulation of aged terrigenous organic matter obtained from the Bering Sea (Meyer et al., 2019). The above lines of evidence thus support a scenario of rather substantial OC_{petro} mobilization and oxidation during the ice-sheet retreat (the last deglaciation).

North America was largely covered by the Laurentide Ice Sheet (LIS) during the LGM (Dalton et al., 2020; Dyke, 2004). According to the characteristics of the underlying bedrocks, North America can be subdivided into the OC_{petro}-rich western Canadian bedrocks and the OC_{petro}-poor Canadian Shield. As the LIS retreated from west to east, it first exposed the OC_{petro}-rich western Canadian bedrocks during the deglaciation (Copard

et al., 2007), including shales, coal, and oil sands within the deglaciated terrains (Blattmann, 2021; Campeau et al., 2020, and references therein). Because the exposure of these OC_{petro}-rich bedrocks coincided with the deglacial CO_2 rise, Blattmann (2021) hypothesized that exhumation of bedrocks and the subsequent oxidation of rock-derived OC_{petro} following the LIS retreat from western Canada may have acted as a significant carbon source to the atmospheric CO_2 rise. However, dedicated studies of this process are still restricted in numbers and regions, and more work is required to test this hypothesis. Studying marine sediment cores archiving land-derived OC has the potential to provide insight into the relationship between OC_{petro} mobilization and glacial retreat during the last deglaciation.

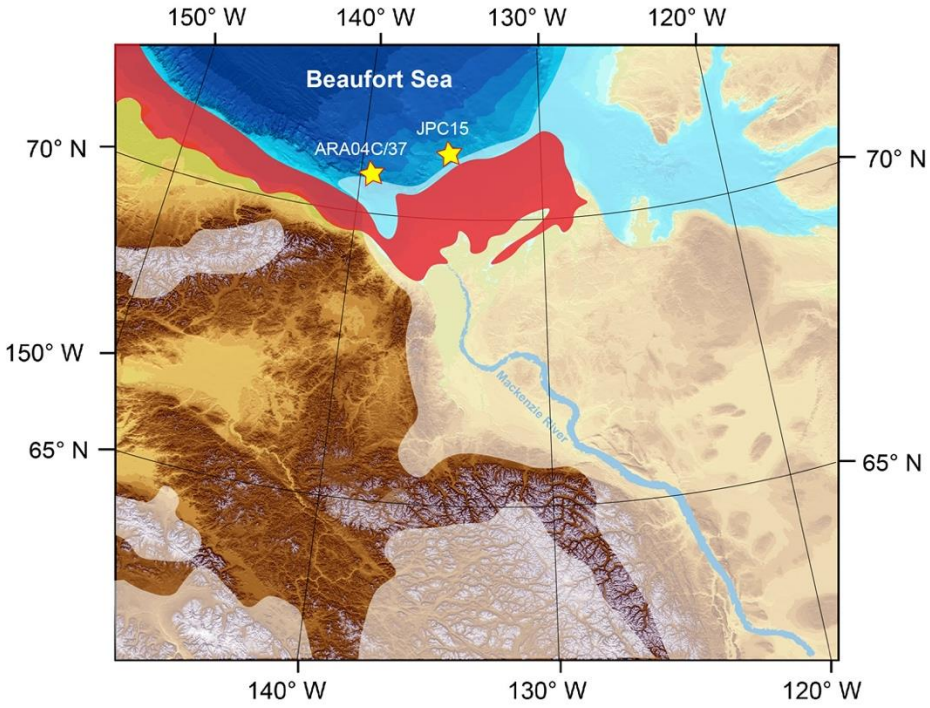

Figure 4.1 Paleoenvironment and core locations in the Canadian Beaufort Sea. Core locations of ARA04C/37 and JPC15 in this study are indicated by yellow stars, and the Mackenzie River is outlined by a blue line. The red area between the paleo coast and the present coastline has been flooded since the Last Glacial Maximum (ca. 21 kyr BP), according to the global ICE-6G_C model (Peltier et al., 2015). The white transparent areas indicate the Laurentide Ice Sheet extent during the Last Glacial Maximum (Dalton et al., 2020).

Our study area in the Canadian Beaufort Sea (Fig. 4.1) is ideally located to elucidate both OC_{petro} mobilization in the past and the process of coastal erosion of OC-rich permafrost. So far, all studies on permafrost carbon remobilization have been carried out along the Eurasian continental margins including the slope and shelf of the Laptev Sea, the shelves of the East Siberian Sea, the Chukchi Sea, and the continental slopes of the Bering Sea, the North Pacific, and the Okhotsk Sea (Keskitalo et al., 2017; Martens et al., 2020, 2019; Meyer et al., 2019; Tesi et al., 2016; Winterfeld et al., 2018). With the possible exception of the Bering Sea, the continental areas in the hinterland of these regions remained largely unglaciated during the LGM. A complex combination

of processes during the last deglaciation including water runoff, shelf flooding, and permafrost thawing in the interior makes it difficult to unambiguously determine the first-order controlling mechanisms of permafrost mobilization in these regions, i.e., via hinterland permafrost thawing or by flooding of continental shelves. In contrast to the ice-sheet-free situations, the LIS in North America hindered both the development of vegetation and carbon-rich permafrost deposits along the Mackenzie River basin. This unique feature avoids signals from the hinterland permafrost thawing and thus makes it an ideal region to study the process of coastal erosion.

Here, we use radiocarbon and biomarker analyses of the well-dated core ARA04C/37 from the Canadian Beaufort Sea (Fig. 4.1; 70°38.0212'N, 139°22.0749'W; 1173 m), spanning the last 14 kyrs (Wu et al., 2020). To extend the records in the Bølling/Allerød (B/A) interval, samples from the nearby core JPC15 (Fig. 4.1; 71°06.222'N, 135°08.129'W; 690 m) were also analyzed. Ancient OC may include pre-aged terrestrial biospheric organic carbon ($OC_{terr\text{-}bio}$) and radiocarbon-free OC_{petro}. To qualitatively estimate the contributions from OC_{petro}, thermal maturity of bulk OC was assessed by multiple proxies derived from biomarkers and pyrolysis, as thermal mature OC certainly has a source from OC_{petro}. Radiocarbon dating of bulk OC and terrigenous compounds was performed to further characterize the OC and to attribute it to OC_{petro} and $OC_{terr\text{-}bio}$ sources (source apportionment based on the ^{13}C and $\Delta^{14}C$ values). We demonstrate that ice-sheet retreat has caused substantial OC_{petro} mobilization during the last deglaciation with OC_{petro} MARs being 9-23 times higher than today, and the rapid sea-level rise most likely caused two events of coastal erosion at ca. 14 and 11 cal. kyr BP. Based on our findings, we further estimated the carbon release from OC_{petro} oxidation during the deglaciation and assessed the impacts of oxidized OC_{petro} and flooded permafrost on atmospheric CO_2 variations by using the global carbon cycle model BICYCLE. Model simulation suggests that the two processes additively have a long-term effect of an increase in atmospheric CO_2 of 12 ppm and a decrease in $\Delta^{14}C$-CO_2 of 12 permil.

4.2 Results

4.2.1 Glacial retreat mobilized substantial amounts of petrogenic OC

The Mackenzie River today is the largest river in the Canadian Arctic with a water discharge of 316 $km^3\ yr^{-1}$ and a sediment flux of 124-128 Mt yr^{-1} (Holmes et al., 2002). In the records of core ARA04C/37, hydrogen index (HI) and oxygen index (OI) derived from Rock-Eval pyrolysis indicate a predominantly terrestrial OC source throughout the deglaciation (defined until 10 cal. kyr BP in this study) and the Holocene (Supplementary Fig. 4.1), which is in agreement with the low values of stable carbon isotopes of the bulk OC ($\delta^{13}C_{org}$) between –28‰ and –26‰ (Fig. 4.2d) (Wu et al., 2020). Strongly influenced by the Mackenzie River input, the OC in marine sediments of this region is predominantly terrigenous.

The OC in the modern Mackenzie River basin contains a large fraction of OC_{petro} (Goñi et al., 2005; Hilton et al., 2015), and our records demonstrate an even increased OC_{petro} input in the past. Multiple proxies, i.e., carbon preference index of high molecular weight (HMW) *n*-alkane (CPI_{alk}), fractional abundance of "biological" homohopane to its diagenetic isomers (fββ), and temperature at which pyrolysis yields the maximum of

hydrocarbons (T_{max}), are used as indicators for carbon thermal maturity (see methods). The very low values of CPI_{alk} and fββ, as well as high T_{max} values all suggest significant contributions from OC_{petro} in this region (Fig. 4.2e-g). Besides, these proxies show distinct changes at the onset of the Younger Dryas (YD), suggesting that the so-called YD flood via the Mackenzie River (Keigwin et al., 2018; Wu et al., 2020) has enhanced the OC_{petro} mobilization.

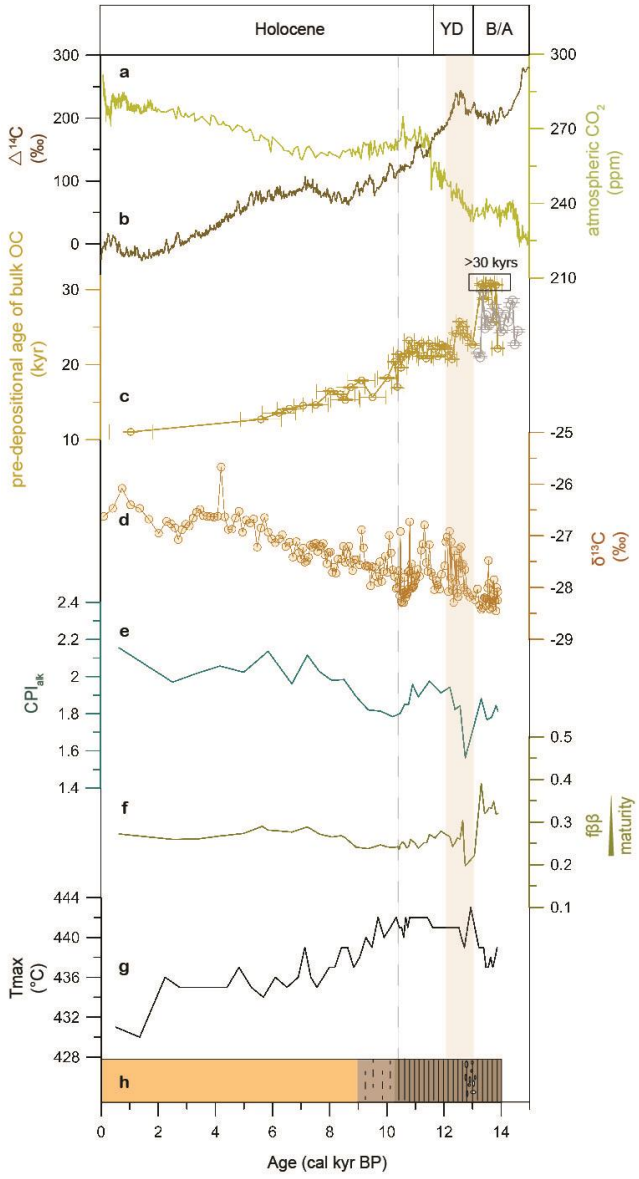

Figure 4.2 Characteristics of bulk OC in the Canadian Beaufort Sea. a atmospheric CO_2 concentrations (Köhler et al., 2017); **b** radiocarbon content reconstructed in IntCal13 (Reimer et al., 2013); **c** pre-depositional age of bulk OC, brownish yellow for core ARA04C/37 and gray for core JPC15; **d** $\delta^{13}C_{org}$ values in core ARA04C/37 (Wu et al., 2020); **e-g** thermal maturity proxies CPI_{alk}, fββ, and T_{max} from core ARA04C/37 (see methods for more details); **h** lithology (according to Supplementary Figure 4.2), brownish black section indicates finely laminated sediments and orange section indicate bioturbated silty clay. The light brownish section with dashed lines represents the transition characterized by weakly laminated sediments.

Radiocarbon dating of bulk OC is used to characterize the carbon age at the time of deposition (pre-depositional age). The pre-depositional ages of bulk OC were oldest between 14.5-10 cal. kyr BP while values decreased throughout the Holocene (Fig. 4.2c). We note that some samples from the late B/A interval show a low ^{14}C content close to the background, and the pre-depositional ages of bulk OC in these samples are reported as minimum ages (>30 kyrs). The carbon ages suggest that the terrestrial carbon delivered into the Canadian Beaufort Sea during the last deglaciation was much older compared to the Holocene input. When compared to the mean age of modern Mackenzie River POC (6.6±1.2 kyrs) (Grotheer et al., 2020, and references therein), the differences are even larger. The very old bulk OC during the last deglaciation was most likely attributed to a larger contribution of OC_{petro}. This is supported by OC thermal maturity and $\delta^{13}C_{org}$ values which were close to the $\delta^{13}C$ values of OC_{petro} (–28.6±0.5‰) in rocks in the river basin (Johnston et al., 2012) (Fig. 4.2d).

The interval of enhanced OC_{petro} contribution (14.5-10 cal. kyr BP) coincides with finely laminated sediments found in the core (Fig. 4.2c and Fig. 4.2h, Supplementary Fig. 4.2), which implies higher OC_{petro} MARs during the last deglaciation. The increased OC_{petro} MARs most likely resulted from enhanced OC_{petro} supply and the possibly increased burial efficiency. Glacial erosion and the glacial retreat induced isostatic uplift may have increased the physical erosion of rocks, resulting in strongly enhanced OC_{petro} supply. Besides, the ice sheet, which entrained abraded material from the underlying rocks including ancient kerogen deposits during the glaciation, may have released OC_{petro} upon melting. On the other hand, factors such as shorter pathways from glacier to the ocean, high sedimentation rates, and adsorption onto mineral surfaces may have protected OC_{petro} from oxidation and increased the burial efficiency.

4.2.2 Coastal erosion mobilized ancient permafrost carbon

During the last deglaciation, the TOC MARs show three distinct peaks (Wu et al., 2020) (Fig. 4.3d), and only the middle one can be explained by the YD flood (Wu et al., 2020). Although field work suggests a post-YD flood originating from the proglacial lakes McMurray, Meadow, and Churchill between 11.7-9.3 cal. kyr BP (Fisher et al., 2009; Murton et al., 2010), an unambiguous meltwater flood signal has not been identified in marine records yet. For instance, core JPC15 only documented the YD freshening in the Canadian Beaufort Sea in its $\delta^{18}O$ record while during the putative post-YD flood values are even higher than the 2‰ baseline (Keigwin et al., 2018) (Fig. 4.3a). In records of core ARA04C/37, the terrestrial biomarkers branched glycerol dialkyl glycerol tetraethers (b-GDGTs, most probably derived from proglacial lakes) and the diol proxy ($F_{C32\ 1,15}$, indicative for running water) peaked during the YD flood, whereas no such clear signals were found during the post-YD flood (Fig. 4.3c-d), suggesting a less catastrophic post-YD flood (Wu et al., 2020). Therefore, the increase in TOC MARs at ca. 11 cal. kyr BP cannot be fully explained by a post-YD flood. To better constrain the carbon sources which contributed to high TOC MARs at ca. 14 and 11 cal. kyr BP, more information about terrestrial carbon is needed.

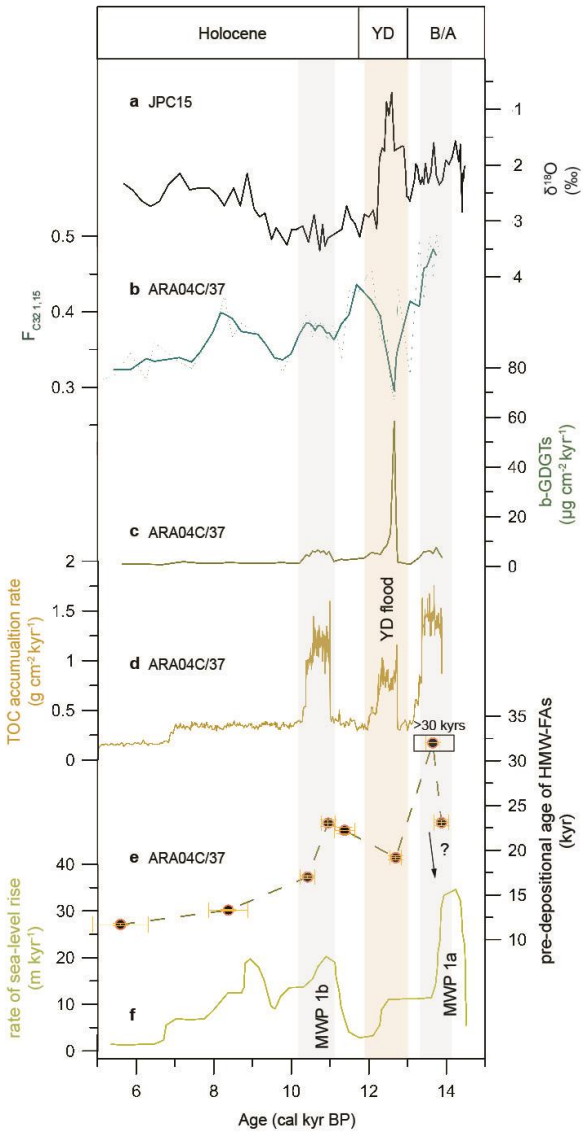

Figure 4.3 Coastal erosion and Younger Dryas flood event. a $\delta^{18}O$ values of *Neogloboquadrina pachyderma* in core JPC15 (Keigwin et al., 2018); **b-c** $F_{C32\ 1,15}$ (fractional abundance of C_{32} 1,15-diol) and mass accumulation rate of b-GDGTs in core ARA04C/37 (Wu et al., 2020); **d** mass accumulation rate of TOC (Wu et al., 2020); **e** pre-depositional age of HMW-FAs; **f** rate of sea-level rise (Lambeck et al., 2014).

As the high molecular weight fatty acids (HMW-FAs) are synthesized by terrestrial higher plants and are expected to be largely absent in mature petrogenic materials, the HMW-FAs are commonly taken to represent $OC_{terr\text{-}bio}$ (Drenzek et al., 2007; Eglinton et al., 2021; Galy and Eglinton, 2011; Hein et al., 2020; Kusch et al., 2021; Tao et al., 2015). The pre-depositional ages of HMW-FAs were much older between 14.5-10 cal. kyr BP, and values decreased during the Holocene (Fig. 4.3e, Supplementary Table 4.1). The pre-depositional ages of HMW-FAs during the deglacial exhibit large age differences with the modern $OC_{terr\text{-}bio}$ (5.8±0.8 kyrs) in the Mackenzie River basin (Hilton et al., 2015). This is attributed to the restricted vegetation, which was limited

by the LIS during the last deglaciation. Less vegetation has resulted in less contributions of freshly produced young carbon, leading to older ages of bulk OC. It also implies that the composition of $OC_{terr\text{-}bio}$ during the last deglaciation was different from the modern one.

The pre-depositional ages of HMW-FA were not uniformly old during the entire deglaciation. The occurrences of particularly old HMW-FAs coincide well with the sharply enhanced TOC MARs at 14 and 11 cal. kyr BP (Fig. 4.3d-e). As permafrost formation along the Mackenzie River basin was restricted by ice sheet, the very old HMW-FAs and rapidly increased TOC MARs were unlikely caused by hinterland permafrost thawing. Rather, the two events co-occur with the global melt water pulses (MWP) 1a and 1b (Fig. 4.3d-f). indicating that the old HMW-FAs were most likely released by coastal erosion (induced by rapid sea-level rise) of permafrost and/or immature ancient OC-rich deposits. The first erosion event occurred during the B/A at ca. 13.9-13.4 cal. kyr BP, slightly after MWP 1a (Fig. 4.3e and Fig. 4.3f). The small apparent delay of this event is probably due to dating uncertainties caused by a lack of AMS ^{14}C dates at the base of core ARA04C/37 (see methods).

Although the distinct increases in TOC MARs can be linked to rapid coastal erosion events during the MWP 1a and 1b, the parameters of bulk OC did not show significant changes (Fig. 4.2). This suggests that, despite the strong erosion processes, the bulk OC was still dominated by thermally mature OC_{petro} while the mobilized ancient $OC_{terr\text{-}bio}$ accounted for relatively small contributions. The overwhelming OC_{petro} input can be attributed to 1) continuously high OC_{petro} supply from the hinterland, and 2) significant contributions from the eroded coastal deposits containing also OC_{petro} debris (Bröder et al., 2021).

4.3 Discussion

The enhancement of OC_{petro} MARs during the last deglaciation can be assessed by estimating the relative contributions of OC_{petro} to bulk OC. A three end-member mixing model based on a Monte Carlo simulation was used to apportion the relative contributions of OC_{petro}, $OC_{terr\text{-}bio}$, and marine biospheric carbon ($OC_{marine\text{-}bio}$) (Fig. 4.4b). The δ^{13}C values of these end members are taken from published data (Hilton et al., 2015; Vonk et al., 2014, and references therein) (see methods). As OC_{petro} is radiocarbon free, the Δ^{14}C of the OC_{petro} end member was defined as −1000‰. The Δ^{14}C of the $OC_{marine\text{-}bio}$ end member depends on the marine reservoir ages (R), thus the R-converted Δ^{14}C were used as end member values. Values of R in the Canadian Beaufort Sea have been discussed in detail in Keigwin et al. (2018) (see methods). According to our HMW-FA record, the radiocarbon composition of $OC_{terr\text{-}bio}$ during the last deglaciation was different from today and the $OC_{terr\text{-}bio}$ was much older in the past. Thus, the respective $\Delta^{14}C_{ini}$ (radiocarbon content at the time of deposition) values of HMW-FAs were taken to represent the $OC_{terr\text{-}bio}$ end-members for each period (see methods).

OC_{petro} was estimated to contribute between ~60-80% of TOC during the last deglaciation and its relative contribution decreased to ~20-40% in the late Holocene (Fig. 4.4, Supplementary Table 4.1). The OC_{petro} fraction estimated for the late Holocene is close to the modern observations at the Mackenzie River delta, where OC_{petro} accounts for ~10%-30% of total POC (Hilton et al., 2015). In general, the fractions of OC_{petro}

during the last deglaciation were 1.5- to 3.8-fold higher than those in the late Holocene (Supplementary Table 4.1). As the TOC accumulation rates during the deglaciation (~0.38 g cm^{-2} kyr^{-1}) were 6 times higher than those in the late Holocene (~0.06 g cm^{-2} kyr^{-1}), we thus conclude that the OC_{petro} MARs were 9-23 (or 16±7) times higher during the last deglaciation compared to the late Holocene.

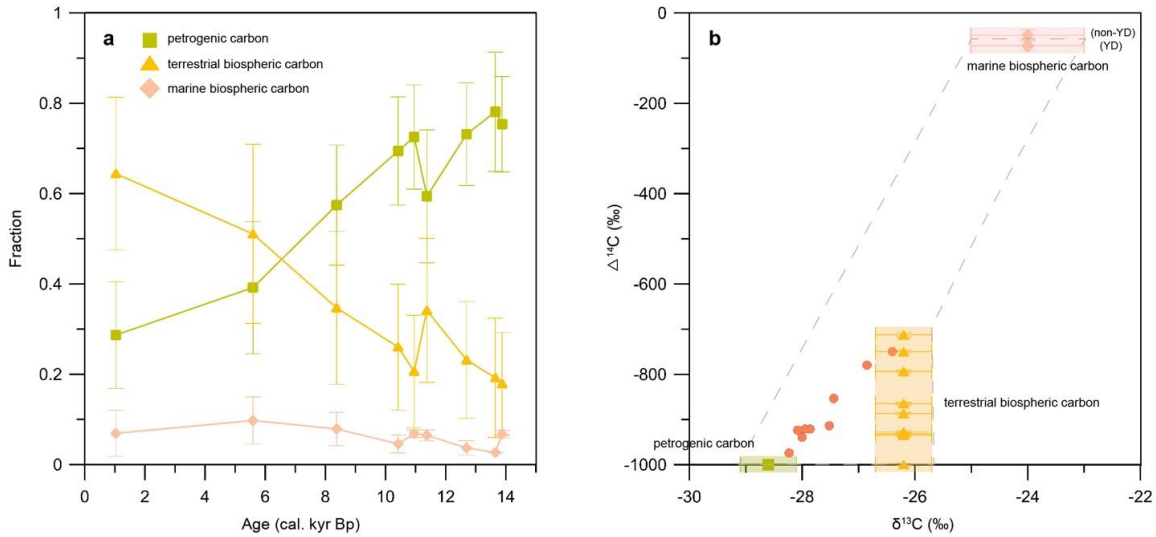

Figure 4.4 Dual-isotope mixing model and source apportionments. a OC fractions from different carbon sources; **b** dual-isotope mixing model as well as $\delta^{13}C$ and $\Delta^{14}C$ ini values of end members (marine biospheric carbon, terrestrial biospheric carbon, and petrogenic organic carbon) (see methods). The red dots indicate measured values of bulk OC for samples.

Enhanced OC_{petro} MARs during the last deglaciation reflect strong physical erosion caused by glacial retreat. Modern observations suggest that ~10%-90% of the exhumed OC_{petro} are oxidized, percentages varying in different regions, whereas the OC_{petro} buried in river/marine sediments are unoxidized and may be chemically and physically resilient (Hilton and West, 2020, and references therein). If we assume a constant burial efficiency in our records, the increases in OC_{petro} MARs can indicate increases in OC_{petro} supply/physical erosion, and further reflect the increases in OC_{petro} oxidation fluxes.

In the Mackenzie River basin, the modern OC_{petro} oxidation fluxes are estimated to be around 0.45±0.19 tC km^{-2} yr^{-1} for the entire Mackenzie River basin and 0.89±0.32 tC km^{-2} yr^{-1} for its main tributaries (Peel, Arctic Red, and Liard Rivers) (Horan et al., 2019). The OC_{petro} oxidation flux for the entire basin is moderate in comparison to its tributaries. This can be attributed to the fact the only 53.9% of the basin is on shales whereas the tributaries drain through the mountain regions that are dominated by shales (Amiotte Suchet et al., 2003). By assuming a constant burial efficiency, the OC_{petro} MARs suggest that the potential/maximum oxidation fluxes on land may have also increased up by 9-23 (or 16±7) times during the last deglaciation, i.e., 7.2±4.4 tC km^{-2} yr^{-1} for the entire basin and 14.2±8.1 tC km^{-2} yr^{-1} for the main tributaries.

One should keep in mind that physical erosion was not the only factor responsible for the increases in OC_{petro} MARs. On a larger spatial scale, the global TOC MARs during the LGM were 147±18% of the Holocene, and

then gradually decreased to the Holocene level (Kandasamy and Nath, 2016). It may indicate more efficient OC transfer from the sea surface to sea floor and better preservation in marine sediment during the LGM and the last deglaciation. In the study area, the meltwater-induced high discharge and shorter pathway from glacier to ocean may have further shortened the transport time and thus increased the OC burial efficiency. Besides, adsorption on the surface of eroded minerals might be another important process to transport and protect OC_{petro} from oxidation. Because the OC_{petro} burial efficiency might have been increased during the last deglaciation via multiple processes, the estimated OC_{petro} oxidation fluxes must therefore be regarded as an upper limit.

On the other hand, the extremely high OC_{petro} MARs were a primary response to the enhanced exhumation of rocks during glacial retreat, and there are reasons that we can expect even larger oxidation fluxes than we predicted. For instance, glacial grinding/erosion may have supplied more fine-grained sediments with highly reactive surface areas (Anderson, 2005), which can promote the OC_{petro} oxidative weathering even at the same rate of OC_{petro} supply. Besides, the enhanced OC_{petro} MARs in our records may only reflect part of the exhumed OC_{petro}. Not all of the exhumed OC_{petro} was transported to the ocean, and much of the glacially eroded material may have been deposited on land (e.g., moraines). Thus, the exhumation of OC_{petro} might be stronger than reflected in the marine sediment records.

The carbon release of OC_{petro} oxidation (J_{carbon}) from western Canada during the last deglaciation can be estimated based on the exposed area ($A_{exposure}$), exposure time ($T_{exposure}$), and oxidative weathering fluxes ($F_{oxidation}$) using the equation from Blattmann (2021):

$$J_{carbon} = A_{exposure} \times T_{exposure} \times F_{oxidation} \quad \text{(Eq. 1)}$$

As OC_{petro} has a primary source from shales, $A_{exposure}$ here is defined as areas of shales exposed by glacial retreat. Our estimate of $A_{exposure}$ is based on the distribution of shales and the history of ice-sheet retreat in North America (Amiotte Suchet et al., 2003; Peltier et al., 2015) (Fig. 4.5a; 180°W-75°W, 45°N-90°N), in steps of 500 years. We assume that the newly exposed shales had a maximum $F_{oxidation}$ (14.2±8.1 tC km^{-2} yr^{-1}) and this flux decreased over time to the modern $F_{oxidation}$ (0.89±0.32 tC km^{-2} yr^{-1}). Because the long-term weathering rates of OC_{petro} are poorly constrained, we assume that weathering rates decrease with increasing substrate age in a similar manner as in silicate weathering (i.e., $F_{oxidation} = F_0 \times t^{-0.71}$) (Taylor and Blum, 1995; Vance et al., 2009). By defining the substrate ages (t) of 5 kyrs, 10 kyrs, and 15 kyrs for modern $F_{oxidation}$ (~1 tC km^{-2} yr^{-1}), the possible long-term $F_{oxidation}$ are shown in Figure 4.5b. The predicted $F_{oxidation}$ for freshly exposed shales (substrate age <200 years) are within the range estimated by our marine records. J_{carbon} is calculated in steps of 100 years and has been integrated over all time steps. The annual carbon release over time is shown in Figure 4.5c and the cumulative carbon release has been estimated as of 84.3±30.4 PgC.

Beside exhumation and oxidation of OC_{petro} during the last deglaciation, evidence for coastal erosion of permafrost occurring in well-defined pulses is also contained in our records. Within dating uncertainties, the release of ancient carbon recorded in our core were broadly coeval across the North Pacific and Arctic Ocean (Meyer et al., 2019; Winterfeld et al., 2018), with a distinct maximum in accumulation in the PreBoreal

(MWP1b) and a maximum at or around MWP1a (Fig. 4.3). Because inland permafrost formation was restricted in the Mackenzie River basin, our records hence confirm that coastal erosion induced by rapid sea-level rise was a major process of aged permafrost carbon release (Winterfeld et al., 2018).

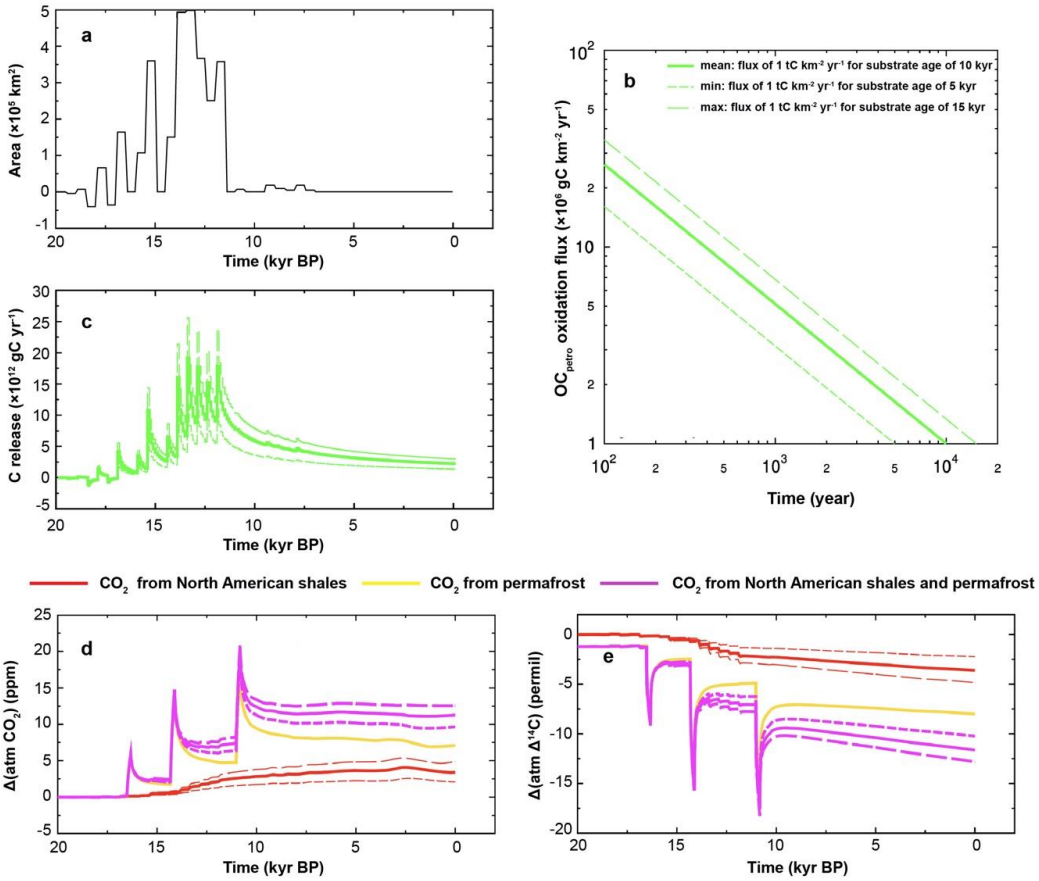

Figure 4.5 Carbon release from OC_{petro} oxidation and simulated impacts on atmospheric CO_2 using the global carbon cycle model BICYCLE. a areas of ice-sheet retreat on shales calculated in steps of 500 years (Amiotte Suchet et al., 2003; Peltier et al., 2015); **b** assumed long-term OC_{petro} oxidation fluxes in North America; **c** carbon release from OC_{petro} oxidation, short-term peaks are attributed to the J_{carbon} calculated in steps of 100 years for every 500-year exposed areas; **d** simulated anomalies in atmospheric CO_2 levels; **e** simulated anomalies in atmospheric $\Delta^{14}C$.

Remobilized ancient permafrost carbon has been proposed to be highly bioavailable. A recent study mimics coastal permafrost erosion by incubating permafrost with and without seawater for the duration of one Arctic open-water season (Tanski et al., 2019). The authors demonstrate that substantial amounts of OC are quickly re-mineralized in all incubations, and the CO_2 production is even higher when seawater is added, indicating potentially significant CO_2 emissions from erosion of permafrost onshore and within the nearshore waters. Estimates from Herschel Basin, a shelf basin in the Beaufort Sea, suggest that ~40% of the eroded permafrost carbon from adjacent Herschel Island is buried locally in the basin (Grotheer et al., 2020), where it may,

however, be further degraded. Another study based on OC concentrations of thawed samples from eroded bluffs estimates that ~66% of the OC contained in Yedoma deposits is released as CO_2 in one thawing season prior to reaching a water body downslope (Vonk et al., 2012). Accordingly, the eroded permafrost carbon may have a significant impact on deglacial rapid CO_2 rises.

The two processes of carbon release, i.e., exhumation of OC_{petro} and erosion of permafrost deposits are both related to ice-sheet retreat. Ice-sheet retreat directly led to erosion, exposure, and oxidation of OC_{petro} which released carbon of 84.3±30.4 PgC. At the same time, reduction in ice volume resulted in sea-level rise leading to remobilization of permafrost carbon by coastal erosion/shelf flooding. Deglacial carbon release from flooded permafrost from the Arctic shelves is estimated to amount to 85 PgC (Winterfeld et al., 2018), and our findings confirm that the carbon has been released in pulses. In order to assess the impacts of the ice-sheet retreat via the combined processes mentioned above on atmospheric CO_2 variations, the global carbon cycle model BICYCLE has been employed for a simulation. Carbon release from OC_{petro} is based on the carbon release rates in Figure 4.5c, whereas permafrost carbon release follows the simulation in Winterfeld et al. (2018) with pulsed release of 34 PgC at 11.5 and 14.6 kyr BP and 17 PgC at 16.5 kyr BP. All carbon is released as CO_2 and simulated to directly enter the atmosphere.

Results show that the two processes additively simulated three peaks which are dominated by the signal resulting from the rapid release of permafrost carbon. These events include the first CO_2 peak of 6 ppm at 16.5 kyr BP and two more CO_2 peaks at 14.6 and 11.5 kyr BP, which are similar in amplitude of 12 ppm each (Fig. 4.5d). Decrease in $\Delta^{14}C$ has been simulated to amount to 9 permil at 16.5 kyr BP and about 12 permil at 14.6 kyr BP and 11.5 kyr BP (Fig. 4.5e). Due to the addition of OC_{petro} release, the simulation results in twice the CO_2 anomalies as estimated by Winterfeld et al. (2018). On a longer-term scale, the atmospheric CO_2 increased by 12 ppm and a $\Delta^{14}C$-CO_2 decreased by 12 permil (Fig. 4.5d and Fig. 4.5e).

Our study provides evidence for enhanced OC_{petro} exhumation and rapid events of coastal erosion during the last deglaciation. Model simulation shows that carbon release from these processes had significant contributions to the atmospheric CO_2 rise. It thus suggests that old terrestrial carbon reservoirs acted as an important contributor to the deglacial CO_2 rise and ice-sheet retreat has played a crucial role in mobilizing these aged/ancient terrestrial OC. Our findings underscore the view of ice sheets playing an active role in the global carbon cycle. Hence more work is needed to investigate the relationship between glacial retreat and carbon release.

4.4 Methods

Core location and sediment chronology

Gravity core ARA04C/37 was collected during the Araon Cruise ARA04C (Jin, 2013) at the Beaufort Sea continental slope, with a recovery of 595 cm (Fig. 4.1). The age-depth model of core ARA04C/37 has been established by Wu et al. (2020) based on accelerator mass spectrometry (AMS) ^{14}C dating on calcareous foraminifera and, in the uppermost centimeters, excess ^{210}Pb. In this study, we update the age-depth model by

dating on planktic foraminifera from the B/A interval, adding two new AMS ^{14}C dates to the age-depth model (Supplementary Table 4.2). Unfortunately, the base of core ARA04C/37 could not be dated due to lack of planktic foraminifera, therefore the age model from Wu et al. (2020), which is based on correlation of magnetic susceptibility data between ARA04C/37 and nearby core JPC15 (Fig. 4.1), is adopted without further modification for the depths below 530 cm. Because the most up-to-date calibration curve Marine20 is intended for marine radiocarbon samples from non-polar regions (Heaton et al., 2020), all ^{14}C ages were transformed into calendar ages using the calibration curve Marine13 (Reimer et al., 2013).

Core JPC15 was obtained at the continental slope east of Mackenzie River (Fig. 4.1). Samples from the B/A interval were analyzed for this study. More information and chronology of sediment core JPC15 please refer to Keigwin et al. (2018).

Rock-Eval pyrolysis

Rock-Eval pyrolysis was performed on bulk sediment samples according to Espitalie et al. (1977). Hydrogen and oxygen contents of the samples, measured as hydrocarbon-type compound and carbon dioxide yields respectively, were normalized to organic carbon and displayed as hydrogen index (mgHC/gC) and oxygen index ($mgCO_2$/gC). In a van Krevelen-type diagram, a classification illustrating carbon types is possible (cf., Meyers and Teranes, 2002). Furthermore, the temperature at which pyrolysis yields the maximum of hydrocarbons (T_{max}), can be used as an indicator of thermal maturity of the kerogen. Immature organic matter has T_{max} values of less than 435 °C.

Biomarker analyses and thermal maturity indicators

Freeze-dried sediments (~5 g) were extracted with DCM:MeOH (2:1, v/v), and an internal standard (Squalane, 2.4 ug/sample) was added prior to analytical treatment. Total lipid extracts were concentrated and separated into a hydrocarbon fraction (containing *n*-alkanes and hopanes) and an alcohol fraction via an open column chromatography with silica gel (6 mm i.d.*4.5 cm). Hydrocarbon fractions were eluted with 5 ml *n*-hexane, followed by alcohol fraction elution with 9 ml ethyl acetate:hexane (1:4, v/v).

The *n*-alkanes were analyzed using a gas chromatograph (GC, Agilent 7890A) coupled to a flame ionization detector (GC-FID). Homohopanes were analyzed with an Agilent 6850 gas chromatograph coupled to an Agilent 5975C VL MSD quadrupole mass spectrometer operating in electron impact ionization (70 eV) and full-scan (*m/z* 50-600) mode.

The *n*-alkanes were identified with external standards and the carbon preference index of *n*-alkanes (CPI_{alk}) was calculated as following (Eq. 2):

$$CPI_{alk} = \frac{1}{2} * \left(\frac{C23+C25+C27+C29+C31}{C22+C24+C26+C28+C30} + \frac{C23+C25+C27+C29+C31}{C24+C26+C28+C30+C32} \right) \quad \text{(Eq. 2)}$$

CPI_{alk} >3 is indicative for significant contributions of fresh OC from immature deposits, whereas CPI_{alk} close to 1 is indicative for a dominance of thermally mature OC (Meyer et al., 2019, and references therein). Because CPI_{alk} may also vary with OC degradation state (Bröder et al., 2016; Vonk et al., 2010), a combination with the relative abundances of homohopane isomers (fββ) can further indicate contributions from thermally mature OC.

Homohopane isomers (C_{31}) were identified by relative retention times and mass-spectra (cf., Meyer et al., 2019). The relative abundance of the "biogenic isomer" 17β,21β(H) 22R (C_{31}ββR) to the "diagenetic isomers" 17β,21α(H) 22R (C_{31}βαR), 17β,21α(H) 22S (C_{31}βαS), 17α,21β(H) 22R (C_{31}αβR), and 17α,21β(H) 22S (C_{31}αβS) is described as Eq. 3 (cf., Meyer et al., 2019):

$$fββ = \frac{C31ββR}{C31ββR+C31αβS+C31αβR+C31βαS+C31βαR} \text{ (Eq. 3)}$$

Values of 1 indicate the absence of "diagenetic isomers", whereas values of 0 indicate the absence of "biogenic isomer".

Radiocarbon analyses of bulk OC and HMW-FAs

Radiocarbon dating was performed following methods described in Mollenhauer et al. (2021). Briefly, according to the respective TOC contents, sediment samples containing approximately 1 mg OC were weighed into silver capsules and were acidified with 6 N hydrochloric acid (HCl) to completely remove the inorganic carbon. Acid evaporation was conducted on a hot plate at 60 °C and the dried samples were then stored in an oven (60 °C) until the analysis. Samples including the silver capsules were packed into tin capsules and combusted individually via an Elementar vario ISOTOPE EA (Elemental Analyzer). Oxidized carbon (CO_2) was directly graphitized by the Ionplus AGE3 system (Automated Graphitization System, Wacker et al., 2010). Radiocarbon contents of samples were analyzed using the Ionplus MICADAS dating system (Synal et al., 2007; Wacker et al., 2010a).

For compound-specific (HMW-FAs) radiocarbon dating, sediment samples (~50-70 g) were extracted with DCM:MeOH (9:1, v/v) using a Soxhlet for over 48 hours. The total extracts were hydrolyzed with potassium hydroxide (KOH, 0.1 M) in MeOH:H_2O (9:1, v/v), at 80 °C for 2 hours. The neutral lipids were extracted with *n*-hexane and the *n*-alkanoic acids were then extracted with DCM after adjusting the pH to a value of around 2 by addition of 37% HCl. The extracted *n*-alkanoic acids were methylated with 37% HCl and MeOH with a known ^{14}C-signature in a nitrogen atmosphere at 80 °C for over 12 hours. The fatty acid methyl esters (FAMEs) were extracted with *n*-hexane and subsequently separated from polar compounds by silica gel chromatography. FAMEs with chain lengths >C_{24} were purified by preparative capillary gas chromatography (PC-GC; Eglinton et al., 1996) using an Agilent 6890N GC equipped with a Gerstel Cooled Injection System (GIS) and connected to a Gerstel preparative fraction collector (Kusch et al., 2010). The GC was equipped with a Restek Rxi-XLB fused silica capillary column (30 m, 0.53 mm i.d., 0.5 µm film thickness). All samples were injected stepwise

with 5 µL per injection. Afterwards, the purified individual FAMEs were transferred into tin capsules and packed. Samples were combusted via the Elementar vario ISOTOPE EA (Elemental Analyzer) and the isotopic ratios ($^{14}C/^{12}C$) of produced CO_2 were determined via the directly connected Accelerator Mass Spectrometry (AMS), the MICADAS system, which is equipped with a gas-ion source.

Radiocarbon contents of the samples were analyzed along with reference standards (oxalic acid II; NIST 4990c) and blanks (phthalic anhydride; Sigma-Aldrich 320064) and in-house reference sediments. Blank correction and standard normalization were performed via the BATS software (Wacker et al., 2010b). All results are reported as fraction modern carbon ($F^{14}C$).

Blank assessment and corrections

Compound-specific samples analyzed for radiocarbon are sensitive to contamination during processing (procedure blank), for example, the carbon introduced via column bleed and carry-over as well as from the tin capsules. Blank correction of compound-specific samples therefore requires careful determination of $F^{14}C_{blank}$ ($F^{14}C$ of the blank) and the size of blank (m_{blank}). For this purpose, radiocarbon analyses of in-house reference samples from ^{14}C-free Messel Shale ($F^{14}C_{OC} = 0$) and modern apple peel ($F^{14}C_{OC} = 1.029 \pm 0.001$) processed in the same way as the compound-specific samples were conducted to determine the $F^{14}C$ and mass of blank, following the method of Sun et al. (2020). All radiocarbon data were corrected for the procedural blank and, to remove the contribution of methyl group during the derivatization process, a methyl-correction was further performed through isotopic mass balance. Uncertainties were fully propagated.

Pre-depositional ages of OC

The pre-depositional age of OC can be derived from the initial radiocarbon content (radiocarbon content prior to the OC deposition to marine sediment) which has been calculated based on the following equation (cf., Schefuß et al., 2016):

$$\Delta^{14}C_{inital} = (F^{14}C\ e^{\lambda t} - 1) \times 1000‰ \quad \text{(Eq. 4)}$$

$F^{14}C$ is the measured fraction modern carbon, and for compound-specific samples the blank- and methanol-corrected $F^{14}C$ values are used. λ is the decay constant of radiocarbon, and t is the time since deposition (according to the core chronology).

The radiocarbon content of the past atmosphere differed from the modern atmosphere, and thus the atmospheric radiocarbon content at the time of deposition ($\Delta^{14}C_{atm}$) have been taken from the atmospheric $\Delta^{14}C$ record of IntCal13 (to keep in consistent with Marine13) (Reimer et al., 2013). The apparent conventional ^{14}C age (pre-depositional age) thus has been calculated by the following equation (cf., Schefuß et al., 2016):

$$\text{pre-depositional age} = -8033 \times \ln[(1 + \Delta^{14}C_{inital}/1000)/(1 + (\Delta^{14}C_{atm}/1000)] \quad \text{(Eq. 5)}$$

Mixing model and source apportionment of OC

The three end-member mixing model based on $\delta^{13}C_{org}$ and $\Delta^{14}C$ was used to estimate the relative fractions of $OC_{marine\text{-}bio}$ ($f_{marine\text{-}bio}$), $OC_{terr\text{-}bio}$ ($f_{terr\text{-}bio}$) and OC_{petro} (f_{petro}). A Monte Carlo simulation was used to calculate the fractions according to the model written as:

$$\Delta^{14}C_{bulk} = f_{marine\text{-}bio} \times \Delta^{14}C_{marine\text{-}bio} + f_{terr\text{-}bio} \times \Delta^{14}C_{terr\text{-}bio} + f_{petro} \times \Delta^{14}C_{petro} \quad \text{(Eq. 6)}$$

$$\delta^{13}C_{bulk} = f_{marine\text{-}bio} \times \delta^{13}C_{marine\text{-}bio} + f_{terr\text{-}bio} \times \delta^{13}C_{terr\text{-}bio} + f_{petro} \times \delta^{13}C_{petro} \quad \text{(Eq. 7)}$$

$$1 = f_{marine\text{-}bio} + f_{terr\text{-}bio} + f_{petro} \quad \text{(Eq. 8)}$$

The values of $\Delta^{14}C_{bulk}$ and $\delta^{13}C_{bulk}$ were measured from bulk OC. The $\delta^{13}C$ and $\Delta^{14}C$ values of each end member are defined as follows. The $\Delta^{14}C_{marine\text{-}bio}$ is converted from the marine reservoir ages (−72.5±11.6‰ for YD and −49.2±11.9‰ for non-YD) (Wu et al., 2020), as Keigwin et al. (2018) discussed in detail that marine reservoir ages were 405±100 during the B/A and Holocene, and were 605±100 during the YD. The $\delta^{13}C_{marine\text{-}bio}$ is defined as −24.0±1.0‰ (Vonk et al., 2014) since no data from local phytoplankton are available. The $\Delta^{14}C_{terr\text{-}bio}$ is represented by the respective $\triangle^{14}C_{ini}$ values of HMW-FAs for each sample, while the $\delta^{13}C_{terr\text{-}bio}$ (−26.2±0.5‰) is taken from the published data from vegetation and soil in the Mackenzie River basin (Bird et al., 2002). We define the $\Delta^{14}C_{petro}$ as −1000‰, and the $\delta^{13}C_{petro}$ (−28.6±0.5‰) is derived from measurements of bedrocks in the river basin (Johnston et al., 2012).

Acknowledgements

We gratefully thank the professional support of the captain and crew of RV Araon on the expedition ARA04C in 2013. We thank Lloyd Keigwin for providing sediment samples from core JPC15. Thanks to Walter Luttmer for conducting the Rock-Eval pyrolysis. Thanks to Vera Meyer for support during the laboratory work. Furthermore, we thank Torben Gentz, Elizabeth Bonk, and Maylin Malter for the radiocarbon analyses. We acknowledge the China Scholarship Council for financial support.

4.5 Supplementary Information

Supplementary Figures

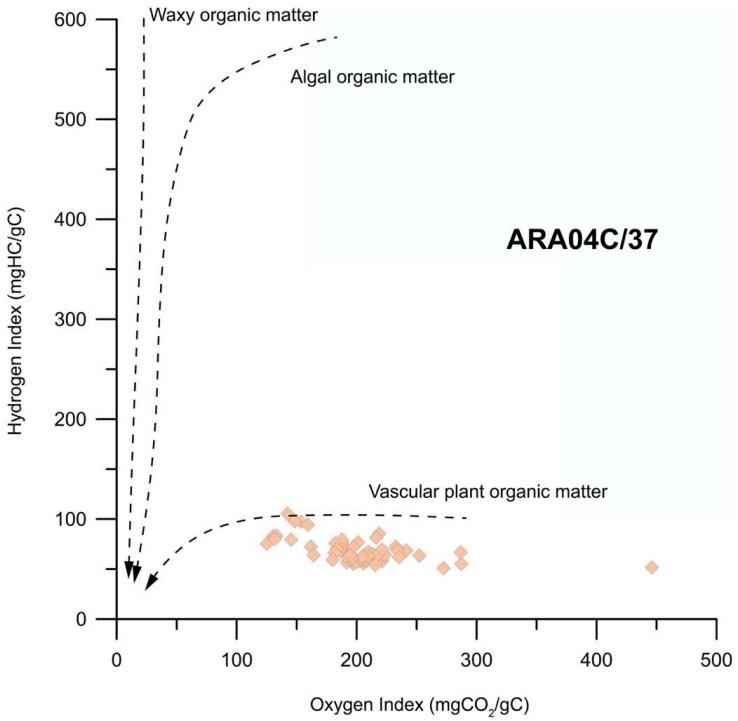

Supplementary Figure 4.1 Carbon sources based on pyrolysis. The pseudo van Krevelen-type diagram shows hydrogen index and oxygen index for bulk OC. The dashed lines illustrate difference carbon sources.

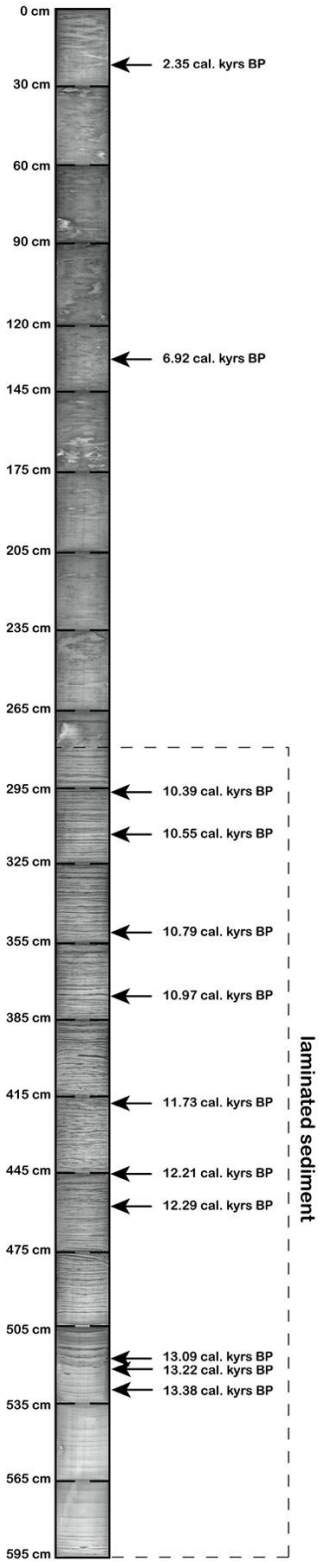

Supplementary Figure 4.2 Lithology of core ARA04C/37. X-ray digital radiograph shows lithology (bioturbation and lamination) of core ARA04C/37.

Supplementary Tables

Supplementary Table 4.1 Apportionment of different carbon sources.

Depth (cm)	Age (cal. kyr BP)	Marine biospheric carbon (mean±s.d.)	Terrestrial biospheric carbon (mean±s.d.)	Petrogenic organic carbon (mean±s.d.)
9	1.036	0.07±0.05	0.64±0.17	0.29±0.12
99	5.592	0.10±0.05	0.51±0.20	0.39±0.15
199	8.374	0.08±0.04	0.35±0.17	0.57±0.13
299	10.420	0.05±0.02	0.26±0.14	0.69±0.12
372	10.952	0.07±0.01	0.21±0.12	0.73±0.12
399	11.376	0.06±0.01	0.34±0.16	0.59±0.15
499.5	12.695	0.04±0.02	0.23±0.13	0.73±0.11
564	13.653	0.03±0.00	0.19±0.13	0.78±0.13
593	13.877	0.07±0.01	0.18±0.11	0.75±0.11

Supplementary Table 4.2 AMS^{14}C dates of core ARA04C/37

Lab ID	Depth (cm)	Species	AMS^{14}C age (year)	ΔR	Calibrated age* (cal. year BP)	Model age** (cal. year BP)
6472.1.2	521	planktic	11756±101	0±100	13233±140	13220±123
6474.1.2	530	planktic	12095±104	0±100	13553±154	13381±157

AMS^{14}C dating of the core ARA04C/37 has been carried out at the Alfred Wegener Institute Bremerhaven using the Mini Carbon Dating System (MICADAS).

*Calibrated ages with 1σ uncertainty, using Calib 7.1 (Stuiver et al., 2020) and based on calibration curve Marine13 (Reimer et al., 2013).

**model ages with default 95% confidence ranges based on Bayesian model (Bacon) (Blaauw and Christeny, 2011) and Marine13 in this study (Reimer et al., 2013).

5. Lipid hydrogen isotopes and freshwater discharge in the Younger Dryas and Holocene Beaufort Sea, Arctic Ocean

Junjie Wu[1], Ruediger Stein[1,2], Julian Sachs[3], Matthew Wolhowe[3], Kirsten Fahl[1]

[1]Alfred Wegener Institute Helmholtz Centre for Polar and Marine Research, Am Alten Hafen 26, 27568, Bremerhaven, Germany

[2]MARUM – Center for Marine Environmental Sciences and Faculty of Geosciences, University of Bremen, P.O. Box 330440, 28359, Bremen, Germany

[3]School of Oceanography, University of Washington, Box 351355, Seattle, WA, 98195, USA

Abstract

Identification of the origin, timing, pathway, and magnitude of the Younger Dryas flood is of significance to improve our understanding and model simulation of abrupt climate changes during the transition from the Last Glacial Maximum to the Holocene. Analyses of hydrogen isotopic composition (δ^2H) of a variety of lipids were performed in a sediment core from the Canadian Beaufort Sea off the Mackenzie River for paleo-hydrological reconstruction. The δ^2H values of short-chain fatty acids show trendless variations throughout the entire records, attributed to the addition of microbially-produced short-chain fatty acids. Synchronous reduction in δ^2H values of leaf wax lipids and dinosterol at the onset of the Younger Dryas (~13.0 cal. kyr BP) most likely indicates a catastrophic meltwater outburst from the proglacial lakes which superimposed on a long-term decay of the Laurentide Ice Sheet. Based on a predicted relationship between δ^2H_{dino} and salinity, a salinity depression of ~24 in surface water has been estimated during the Younger Dryas flood. Salinity has increased since the mid-late Holocene (8-0 cal. kyr BP), likely resulting from a decreased Mackenzie River discharge. It implies a drier climate in the Mackenzie River basin during the mid-late Holocene.

5.1 Introduction

Since the Last Glacial Maximum (ca. 26-19 cal. kyr BP), orbital forcing has likely induced climate warming and ice-sheet decay. During this period of deglaciation, substantial amounts of meltwater flooded into the oceans that may have triggered or modulated the rate and timing of climate change by regulating the freshwater budget and oceanic circulation (Fisher et al., 2002; Peltier et al., 2006; Tarasov and Peltier, 2005). The Atlantic Meridional Overturning Circulation (AMOC) weakening seems to have followed the reduction of the Northern Hemisphere ice-sheet volume (Zhu et al., 2014). Lohmann et al. (2020) further point out that changes in the AMOC sensitively depend on where the deglacial meltwater is injected into the ocean. In the Northern Hemisphere, the Laurentide Ice Sheet (LIS) (Fig. 5.1a) has supplied large amounts of freshwater into the ocean during the last deglaciation (Dalton et al., 2020; Dyke, 2004). An episode characterized by a significant reduction of the AMOC during the so-called Younger Dryas (YD) Cooling Event has been related to an outburst of the LIS meltwater, likely originated from the proglacial Lake Agassiz (Fig. 5.1a; Broecker et al., 1989; McManus et al., 2004; Murton et al., 2010).

Previous studies attempting to evaluate the impact of the YD flood focused on its pathways. As the freshwater discharge via the Mississippi River into the Gulf of Mexico ended abruptly at ca. 13 cal. kyr BP (Williams et al., 2012), the shift of meltwater outlet has been under a debate, i.e., whether it drained first into the Arctic Ocean and then into the Atlantic Ocean or whether it drained directly into the Atlantic Ocean (Broecker et al., 1989; Leydet et al., 2018; Peltier et al., 2006). Recently, reconstructions based on $\delta^{18}O$ of foraminifera and specific biomarker proxies have identified freshening in the Canadian Beaufort Sea, coinciding with the onset of the YD (Keigwin et al., 2018; Wu et al., 2020). That means, this YD freshwater event is represented in a distinct $\delta^{18}O$ minimum of planktic foraminifera (Fig. 5.2a), a prominent minimum in the $F_{C32\ 1,15}$ index (fractional abundance of C_{32} 1,15-diol) indicative for running water (Fig. 5.2b; cf., Lattaud et al., 2017a, 2017b), and short-lived peak values in the flux rates of terrigenous sterols and branched glycerol dialkyl glycerol tetraethers (b-GDGTs) (Fig. 5.2c and Fig. 5.2d). Although freshening has been found in the Arctic Ocean, there is still a missing connection between terrestrial and marine records. The Lake Agassiz is characterized by a large lake-level drop during the YD, and this meltwater outburst is expected to be the freshwater source triggering YD cooling (Breckenridge, 2015; Murton et al., 2010). However, field evidence (e.g., ice margins and shorelines) suggests that Lake Agassiz did not drain to any northwestern outlet before 10.8-10.1 cal. kyr BP (Fisher et al., 2009; Fisher and Lowell, 2012). It thus rises concerns whether the YD freshening in the Canadian Beaufort Sea was caused by enhanced LIS melting alone or by an outburst. In addition, the YD-aged freshening is found not only in the Canadian Beaufort Sea but also in the Northeast Pacific (Praetorius et al., 2020, and references therein). From these, freshwater might have been transported into the Arctic Ocean and then into the North Atlantic deep-water formation regions if the Bering Strait opened at the beginning of the YD. Therefore, a better evaluation of the influence of the YD freshening needs constraints on its timing, magnitude, and origin of the water source.

So far, the approach widely used to reconstruct hydrological changes in surface water in the Arctic Ocean is primarily based on the $\delta^{18}O$ and $\delta^{13}C$ of planktic foraminifera (Poore et al., 1999; Spielhagen et al., 2005; Stein et al., 1994a, 1994b) and sediment proxies (Not and Hillaire-Marcel, 2012). However, dissolution of microfossil limits the proxy application in some of the Arctic regions. Unlike the foraminiferal $\delta^{18}O/\delta^{13}C$ proxy, the hydrogen isotopic composition of lipid biomarkers (δ^2H_{lipid}) can be widely used to reconstruct hydrological changes in both aquatic and terrestrial settings (Ladd et al., 2021; Maloney et al., 2019; Nelson and Sachs, 2014; Sachs and Schwab, 2011). In particular in the marine setting, the δ^2H_{lipid} of marine algae biomarkers is largely determined by their growth water (δ^2H_{water}) used for photosynthesis and the salinity influencing the $^2H/^1H$ fractionation from water to lipids. In this context, the δ^2H_{lipid} records can be used to reflect the hydrological changes, such as the sea surface salinity (Nelson and Sachs, 2016; Sachs and Schwab, 2011; Schouten et al., 2006).

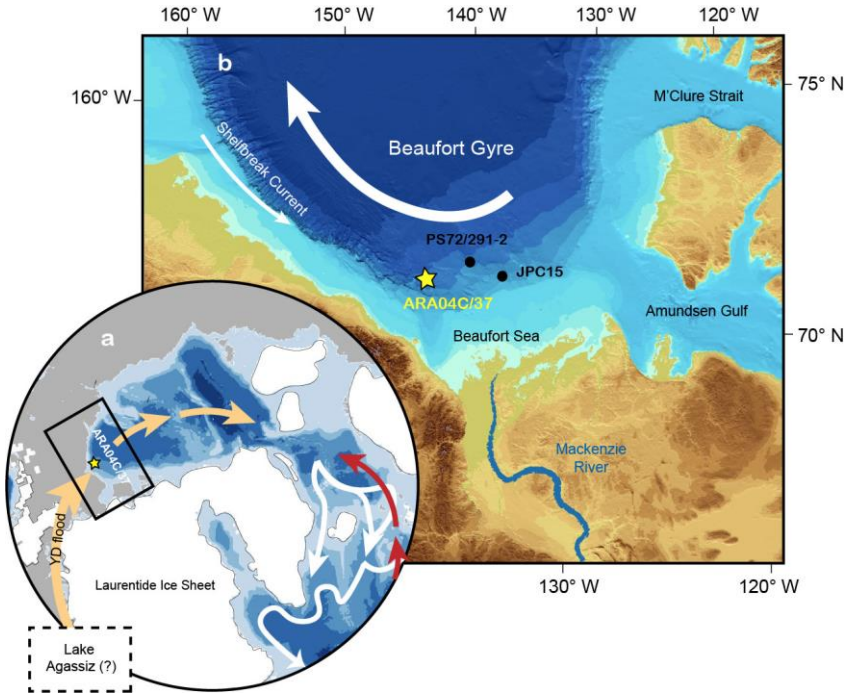

Figure 5.1 (**a**) Northern Hemisphere ice-sheet extent at 13 kyr BP (Peltier et al., 2015). Orange arrows represent the possible pathway of the Younger Dryas flood. Red and white arrows represent the warm Atlantic inflow to the Nordic Sea and the main bottom currents. (**b**) Regional map the of study area, the Canadian Beaufort Sea. Location of core ARA04C/37 is indicated by yellow star and other sediment cores discussed in the text are indicated by black circles. White arrows show the surface water circulation in the southern Beaufort Sea.

A pilot work to apply the hydrogen isotope approach in the Arctic Ocean, i.e., the Laptev and Beaufort Seas characterized by great salinity gradients resulted from large runoff by the Lena River and the Mackenzie River respectively, has been carried out by Sachs et al. (2018). Ideally, marine algae biomarkers (e.g., brassicasterol and dinosterol) with specific sources are of advantage to study the relationship between δ^2H_{lipid} and freshwater discharge/salinity of the marine realm. In the studied coastal seas, however, concentrations of these biomarkers

were too low for δ^2H studies due to the predominance of terrestrial input and the limited amount of sediment material available for the study. Thus, Sachs et al. (2018) assessed the hydrogen isotopic composition of palmitic acid ($\delta^2H_{C16:0}$) in surface sediments from the Laptev Sea and Kara Sea. The authors demonstrated that, based on $\delta^{13}C$ and $\Delta^{14}C$ values of $nC_{16:0}$ fatty acids (FA), the palmitic acid likely has a predominant source from the marine primary productivity there. Besides, the $\delta^2H_{C16:0}$ changes systematically follow the surface salinity gradients, highlighting its sensitivity as an indicator for past surface-water hydrographic changes in the Arctic Ocean (Sachs et al., 2018).

In this study, we analyzed a variety of δ^2H_{lipid} from the core ARA04C/37 (Fig. 5.1b), which can be sorted into three groups, i.e., algal lipids, leaf wax lipids, and generic FAs. For the algal lipids, we measured δ^2H from sterols (brassicasterol, $\delta^2H_{brassica}$; dinosterol, δ^2H_{dino}) extracted and concentrated using large-sized samples of 50-70 g of sediment. For the leaf wax lipids, we measured δ^2H from long-chain FAs ($nC_{28:0}$ FA, $\delta^2H_{C28:0}$; $nC_{30:0}$ FA, $\delta^2H_{C30:0}$). We finally analyzed δ^2H from generic FAs ($nC_{16:0}$ FA, $\delta^2H_{C16:0}$; and $nC_{18:0}$ FA, $\delta^2H_{C18:0}$). The aim of this still low-resolution study is to obtain further ground truth data for the δ^2H approach as salinity proxy and to use these data for reconstructing past hydrological changes in the Canadian Arctic region, with particular interest into the YD flood event. Certainly, a high-resolution study has to follow to fully approve the δ^2H approach for reconstructing Arctic Ocean past salinity changes.

5.2. Material and Methods

Core location and sediment chronology

The location of core ARA04C/37 is shown in Fig. 5.1b. The sediment core was recovered during the 2013 Araon Cruise ARA04C (Jin, 2013) from the Canadian Beaufort Sea continental slope (70°38.0212′N, 139° 22.0749′W; 1173 m). The core has a total recovery of 595 cm, which consists of two units. Unit 1 (0-280 cmbsf) is characterized by bioturbated silty clay whereas Unit 2 (280-595 cmbsf) is characterized by finely laminated sediments, i.e., silty clay/clayey silt alternations. The transition from Unit 2 to Unit 1 is characterized by a weakly laminated section (Wu et al., 2021).

The chronology of core ARA04/37 has been constrained by accelerator mass spectrometry (AMS) ^{14}C dating on calcareous foraminifera, and excess ^{210}Pb in the uppermost centimeters. The age-depth model has been established based on the calibration curve Marine13 (Reimer et al., 2013; Wu et al., 2021, 2020). Using magnetic susceptibility, core ARA04C/37 can be correlated very well with core JPC15, especially for the interval of 280-520 cmbsf. Thus, the age-depth model included six AMS^{14}C dates from core JPC15 (Keigwin et al., 2018) to have better age constraints on deglacial events. For more details we refer to Wu et al. (2021, 2020).

Biomarker lipids extraction and purification

For FAs, freeze-dried sediments (~4 g) were extracted with an Accelerated Solvent Extractor using DCM:MeOH (9:1, v/v) at 1000 psi and 100 °C for three 10-min cycles. The total extracts were saponified with

10 ml 1N KOH in MeOH and 1 ml H_2O at 70 °C for ~12 hours, neutralized with 2 ml 6N HCl and 10 ml H_2O, phase separated into 10 ml *n*-hexane three times, the combined *n*-hexane fractions washed with an additional 10 ml H_2O, and passed through ~2 g of Na_2SO_4. FAs were collected off a 0.5 g aminopropyl-functionalized silica gel (Supelco) column in 8 ml of 4% (v/v) acetic acid in diethyl ether after removing neutral compounds with 8 ml of DCM:isopropyl alcohol (3:1, v/v).

The acid fractions were methyl esterified overnight at 60 °C in 1 ml of dry *n*-hexane and 2 ml of 10% acetyl chloride in dry MeOH. Samples were cooled, then phase-partitioned with 2 ml of *n*-hexane (3×) and 2 ml H_2O. The combined *n*-hexane fractions were passed through ~2 g of Na_2SO_4. The hydrogen isoptopic composition of the methanol derivitization reagent was previously determined by derivitization of phthalic acid of known composition, provided by Arndt Schimmelmann of Indiana University.

For neutral lipids extraction (targeting on brassicasteol and dinosterol), large amounts of sediments (~50-70 g) were extracted using a Soxhlet with DCM:MeOH (9:1, v/v) for over 48 hours. The total extracts were hydrolyzed with potassium hydroxide (KOH, 0.1 M) in MeOH:H_2O (9:1, v/v) at 80 °C for 2 hours, followed by liquid-liquid extraction with *n*-hexane. The lipids extracted into the *n*-hexane were further separated on 1.0 g 5% H_2O deactivated silica gel 60 (40-63 μm, BDH Chemicals). The first fraction containing hydrocarbons was eluted with 10 ml *n*-hexane. The second fraction containing ketones was eluted with 6 ml DCM:hexane (1:1, v/v). The third fraction containing alcohols (sterols) was eluted with 8 ml ethyl acetate:hexane (1:4, v/v). The alcohol fractions were divided into 5 approximately equal aliquots (for HPLC loading, see below) and each was acetylated in 40 μl pyridine and 40 μl acetic anhydride, with a known isotopic composition, at 70°C for 0.5 hour. The hydrogen isoptopic composition of the acetic anhydride was previously determined by derivitization of a phloroglucanol working standard, and comparison to the same working standard derivitized with acetic anhydride of known composition, provided by Arndt Schimmelmann of Indiana University.

Dinosterol and brassicasterol were then isolated from each aliquot using a preparative HPLC (Agilent 1100) following the methods of Nelson and Sachs (2013). Briefly, each aliquot was injected into a 4.6 × 250 mm, 5-micron Agilent XDB-C18 column in 30 ul of DCM:MeOH (2:1, v/v). The eluent was acetonitrile:MeOH (95:5, v/v), which was maintained for 10 minutes, then transitioned to acetonitrile:ethyl acetate:MeOH (85:10:5, v/v/v) over 10 minutes, maintained for 45 minutes, transitioned to 100% ethyl acetate over 10 minutes, and maintained for 10 minutes. Flow rate was constant at 1.5 ml min^{-1} and the column was maintained at 30 °C. Fractions containing brassicaterol and dinosterol were collected between 29.5-33.5 and 50.5-55.5 minutes, respectively. Sterol fractions were characterized via GC-FID and GC-MS, along with 1-minute-long collection windows before and after each sterol fraction to ensure quantitative recovery of the HPLC chromatographic peak. After characterization, the sterol isolates from parallel aliquots were recombined (per sterol).

Hydrogen isotope analyses of lipids

δ^2H_{lipid} values were measured by a gas-chromatography isotope-ratio mass spectrometry (GC-IRMS) via a modification of the procedures outlined in Nelson and Sachs (2013). Briefly, gas chromatography was conducted using a Thermo Trace GC Ultra equipped with a GC-TC (pyrolysis) interface. Samples (~175 ng of

the target compound per 2 ul injection) in toluene were injected into the 320 °C inlet in splitless mode, with a 1.1 ml/min helium carrier flow through a VF-17ms column (60 m × 0.25 mm × 0.25 μm). For sterols (as acetates), the oven temperature was held at 130 °C for the 2-min splitless time, increased to 220 °C at 20 °C /min, increased to 325 °C at 2 °C/min, and held for 15 min. For FAs (as methyl esters), the oven temperature was held at 130 °C for the 2-min splitless time, increased to 320 °C at 4 °C/min, and held for 28 min. The pyrolysis interface was operated at 1410 °C, and the sample hydrogen admitted to a Thermo Delta V Plus isotope ratio mass spectrometer via open split. External standards of known isotopic composition (*n*-alkanes; Arndt Schimmelmann of Indiana University) were injected throughout each sample sequence and used to correct lipid data for drift and offsets with sample size and retention time. For details of external standards and correction please refer to Sachs et al. (2016) and Nelson and Sachs (2014). Samples were analyzed in triplicate, and derivitization-corrected compositions determined via mass balance.

5.3 Results and Discussion

5.3.1 δ^2H_{lipid} for reconstructing hydrological changes in the Beaufort Sea region

During the YD period, the $\delta^{18}O$ record of foraminifera as well as multiple terrestrial biomarker records, determined in sediment cores from the area off the Mackenzie River, documented freshening in the Canadian Beaufort Sea, and, especially the latter ones, imply a possible outburst from proglacial lakes draining through the Mackenzie River into the Arctic Ocean (Fig. 5.2a-2d; Keigwin et al., 2018; Wu et al., 2020). Thus, these data are ideal to test the potential of δ^2H_{lipid} being an indicator for hydrographic changes in both marine and terrestrial environments, and to show whether or how the δ^2H_{lipid} from the different biomarkers reflect the YD freshwater discharge.

In records of core ARA04C/37, the δ^2H of short-chain FAs ($\delta^2H_{C16:0}$ and $\delta^2H_{C18:0}$) show trendless variations throughout the entire record, with full ranges of 13‰ ($\delta^2H_{C16:0}$) and 9‰ ($\delta^2H_{C18:0}$) respectively (Fig. 5.2g, Table 5.1). The δ^2H of both algal lipids ($\delta^2H_{brassica}$ and δ^2H_{dino}) were low between 14-10 cal. kyr BP while values increased throughout the Holocene (Fig. 5.2e). Of these two kinds of algal lipids, the δ^2H_{dino} exhibits a distinctive decrease during the YD. The long-chain FAs $\delta^2H_{C28:0}$ and $\delta^2H_{C30:0}$ show similar trends, characterized by reduced values during the YD and increased values afterwards (Fig. 5.2f). The $\delta^2H_{C28:0}$ increased throughout the Holocene while the increase of $\delta^2H_{C30:0}$ suspended from the mid Holocene.

As the short-chain FAs can be produced by many organisms (e.g., marine and terrestrial, autotrophic and heterotrophic) (Desvilettes et al., 1997; Persson and Vrede, 2006; Sánchez-Machado et al., 2004; Volkman et al., 1989), they are not the best OC source indicators. Based on multiple lines of evidence (δ^2H, $\delta^{13}C$ and $\Delta^{14}C$), Sachs et al. (2018) assumed marine algae being the primary producer of $nC_{16:0}$ FA in surface sediments from the Kara and Laptev Seas. The authors compared $\delta^2H_{C16:0}$ from these surface sediments with measured salinities in these regions and proposed its use as a proxy for salinity in the Arctic Ocean. The δ^2H of short-chain FAs in core ARA04C/37, however, does not show any trend throughout the entire records, and a non-covariation is found between the two compounds ($\delta^2H_{C16:0}$ and $\delta^2H_{C18:0}$) (Fig. 5.2g).

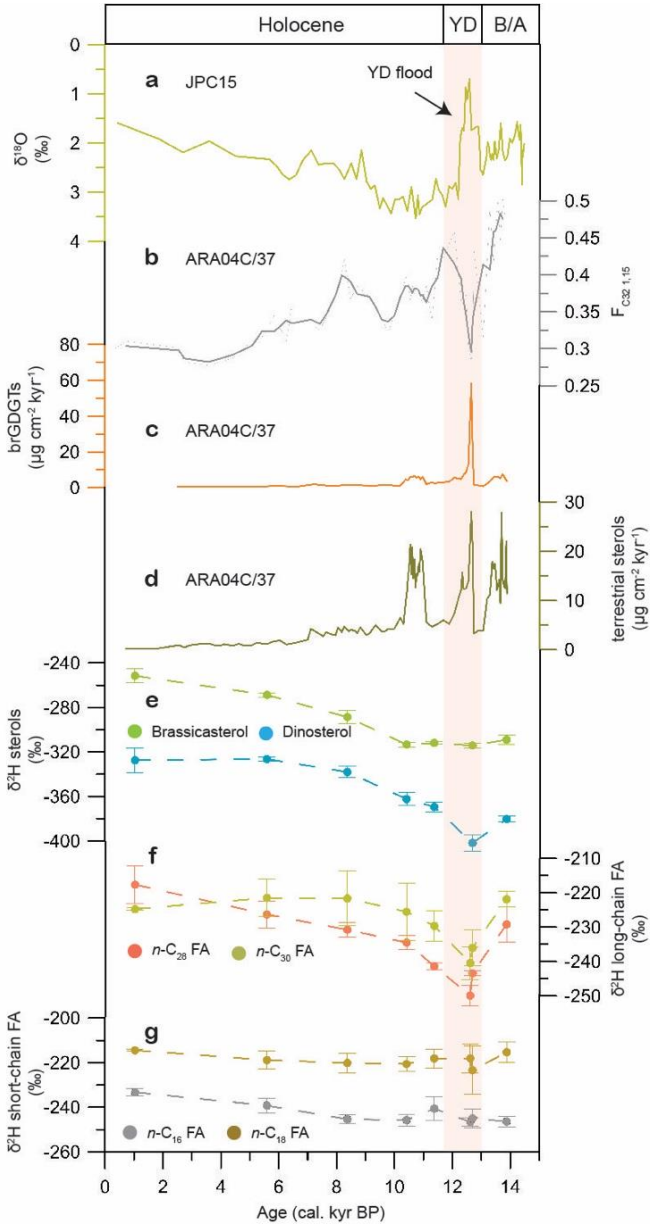

Figure 5.2 Younger Dryas flood signals are shown in records (**a**)-(**d**) from core JPC15 (Keigwin et al., 2018) and core ARA04C/37 (Wu et al., 2020). (**a**) $\delta^{18}O$ values of *Neogloboquadrina pachyderma*; (**b**) $F_{C32\ 1,15}$, fractional abundance of C_{32} 1,15-diol; (**c**) mass accumulation rate of b-GDGTs; (**d**) mass accumulation rate of campesterol and β-sitosterol. δ^2H values analyzed in this study are shown for (**e**) brassicasterol and dinosterol, (**f**) long-chain FAs, and (**g**) short-chain FAs.

The missing YD signal in the short-chain FAs may be explained by the additions of short-chain FAs from microbial activities, which may have preferentially produced short-chain FAs with substantially different δ^2H signatures. It is thus possible that the YD freshwater signal captured by marine-source short-chain FAs has been masked by a mixture of microbial-source signal. This explanation is supported by the conventional

radiocarbon ages of these short-chain FAs which are between 2500 ^{14}C years and 4400 ^{14}C years, much younger than the respective depositional ages (Table 5.1). Heterotrophic bacteria would be feeding on organic matter that was presumably about the same age as the depositional age of the sediment. Therefore, the relatively constant ^{14}C ages of microbially-produced $C_{16:0}$-FAs in the sediment indicates that microbes probably have used more recent CO_2 and H_2O to synthesize the short-chain FAs. Such a process may have occurred even during the sample storage.

Table 5.1 Hydrogen isotope data and conventional radiocarbon ages for nC$_{16:0}$ FAs.

Depth (cm)	compound	Age of deposition (cal. kyr BP)	δ^2H±SD (‰)	Conventional radiocarbon age (^{14}C years)
9	nC$_{16:0}$ FA	1.036	−233.3±1.6	2508±77
99	nC$_{16:0}$ FA	5.592	−239.3±3.2	4428±82
199	nC$_{16:0}$ FA	8.374	−245.4±1.8	4339±90
299	nC$_{16:0}$ FA	10.420	−245.8±2.6	3749±82
399	nC$_{16:0}$ FA	11.376	−240.6±5.2	3477±82
499.5	nC$_{16:0}$ FA	12.695	−245.0±4.3	3372±75
593	nC$_{16:0}$ FA	13.877	−246.4±2.3	3820±86

Brassicasterol and dinosterol are especially produced by marine pelagic algae (Fahl and Stein, 1999; Volkman, 1986) and thus often used as indicators for marine primary productivity. In this context, $\delta^2H_{brassica}$ and δ^2H_{dino} in core ARA04C/37 can be used to reflect hydrographic changes in the marine setting. As δ^2H_{water} in the marine setting may have a mixture signal from the seawater and highly ^{2}H-depleted meltwater from the LIS during the last deglaciation. The relative contributions of meltwater discharge would modulate the δ^2H_{water} and further the $\delta^2H_{brassica}/\delta^2H_{dino}$. During the LIS melting, the enhanced meltwater may have led to a reduction in δ^2H_{water}, resulting in lower values of $\delta^2H_{brassica}$ and δ^2H_{dino} (Fig. 5.2e; Table 5.2). Besides, lower salinity caused by the meltwater discharge may have resulted in larger ^{2}H/^{1}H fractionation during lipid synthesis (M'boule et al., 2014; Maloney et al., 2016; Nelson and Sachs, 2014; Sachs et al., 2016; Sachs and Schwab, 2011; Schouten et al., 2006), also contributing to a reduction in $\delta^2H_{brassica}$ and δ^2H_{dino}. In particular, δ^2H_{dino} exhibits a distinctive peak during the YD, likely resulted from further enhanced meltwater discharge (YD flood) (Fig. 5.2e).

The differences in δ^2H values between brassicasterol and dinosterol may be related to the depth habitat of their producers. Dinoflagellate has been identified mainly in surface water while diatom can be found in both surface water and sub-surface water in the Beaufort Sea (Coupel et al., 2015). During the peak runoff season, freshwater could trigger a strong halocline in the upper few meters of water. It may lead to large differences in the salinity and δ^2H_{water} that phytoplankton has experienced, depending on very small differences in depth habitat. As surface water is characterized by lower salinity and more depleted δ^2H_{water}, δ^2H_{dino} therefore exhibits lower values in comparison to $\delta^2H_{brassica}$ (Fig. 5.2e).

Table 5.2 Hydrogen isotope data for phytoplankton sterols and long-chain FAs.

Depth (cm)	Depositional age (cal. kyr BP)	δ^2H_{dino}±SD (‰)	$\delta^2H_{brassica}$±SD (‰)	$\delta^2H_{C28:0}$±SD (‰)	$\delta^2H_{C30:0}$±SD (‰)
9	1.036	−327.4±11.0	−251.6±6.1	−217.7±5.5	−224.7±0.3
99	5.592	−326.4±2.0	−268.8±1.9	−226.3±3.9	−221.5±5.4
199	8.374	−338.1±5.2	−288.7±5.8	−230.8±2.1	−221.7±8.0
299	10.420	−362.3±5.7	−313.4±2.3	−234.5±2.1	−225.5±8.3
399	11.376	−369.4±4.4	−311.9±1.3	−241.4±0.9	−229.6±4.4
491	12.618			−249.9±2.9	−240.5±4.8
499.5	12.695	−401.9±7.1	−314.2±2.3	−243.4±0.7	−236.0±5.2
593	13.877	−380.3±2.5	−309.0±4.3	−229.2±5.1	−221.9±2.2

Long-chain FAs are primarily produced by higher plant leaf wax, and their hydrogen isotopic compositions (δ^2H_{wax}) can be affected by many processes, e.g., changes in δ^2H_{water}, biosynthetic pathway, and vegetation types (Sachse et al., 2012). Among these factors, the δ^2H_{wax} displays a strong positive correlation with mean annual precipitation globally (Ladd et al., 2021; Liu and An, 2019; McFarlin et al., 2019). Hence, the δ^2H_{wax} has been increasingly used to reconstruct the hydroclimate (Hein et al., 2020; Sachs et al., 2018b). During the last deglaciation, the soil δ^2H_{water} within the Mackenzie River basin was not only influenced by the local precipitation but also the LIS meltwater. Therefore, the distinct reduction in δ^2H_{wax} during the YD was most likely resulted from the increased YD flood discharge which has reduced the soil δ^2H_{water}. However, the leaf wax lipids archived in our core probably have two different terrestrial sources, i.e., derived from the Mackenzie River basin and eroded from the coastal permafrost (Wu et al., 2021). Hence, the interpretation of δ^2H_{wax} in our records is more difficult as discussed in the following subchapters.

5.3.2 Cooccurrence of YD flood signal in terrestrial and marine biomarkers

The δ^2H_{wax} values had a significant reduction at ca. 13 cal. kyr BP coinciding with the YD flood, however, interpretation of δ^2H_{wax} in this region needs more caution. Application of δ^2H_{wax} in a sediment core from the high latitude has to consider the soil carbon turnover time. A global compilation suggests that the ^{14}C ages of terrestrial biomarkers increase (become older) with latitude, which are related to the climate control (Eglinton et al., 2021). Besides, the feature of permafrost soil in the high latitude can significantly increase the residence time of leaf wax lipids in terrestrial reservoirs. It thus implies that the leaf wax lipids archived in marine sediments may encounter multiple potential intermediate storage pools before deposition. In a more detailed study, Wu et al. (2021) estimated the pre-depositional ages (^{14}C ages at time of deposition) of long-chain FAs ($nC_{26:0}$+$nC_{28:0}$ FA) from the same core ARA04C/37, which were more than ca. 19,000 years during the last deglaciation (Fig. 5.3). These authors proposed that the long-chain FAs in core ARA04C/37 have significant sources from permafrost soil via deglacial coastal erosion. Due to the complex carbon sources and the very old carbon ages of long-chain FAs, the δ^2H_{wax} in core ARA04C/37 therefore cannot be used to reconstruct

paleoclimate evolution. Despite the limitation of δ^2H_{wax} to reconstruct the deglacial-Holocene paleoclimate evolution, the δ^2H_{wax} may have ability to capture large changes in δ^2H_{water}, for instance, caused by a flood event.

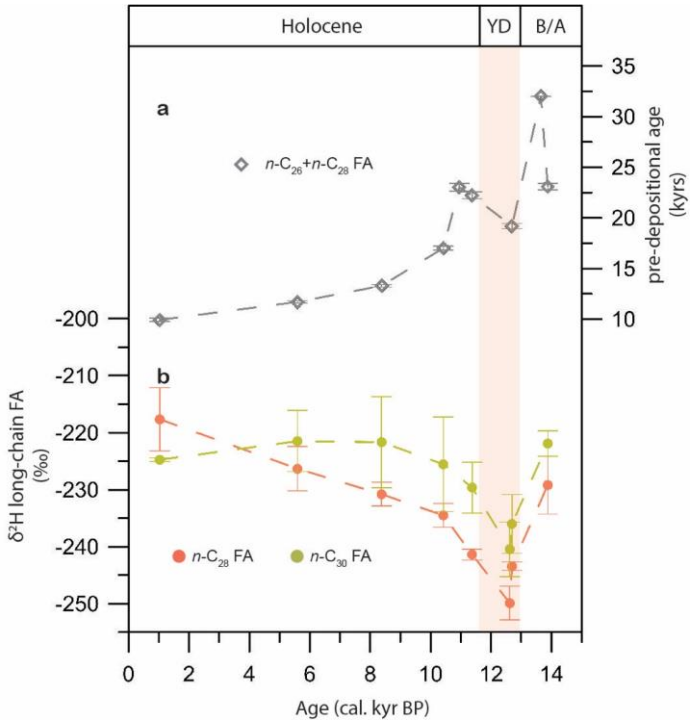

Figure 5.3 (**a**) pre-depositional age of long-chain FAs (*n*C26:0+*n*C28:0 FA) (Wu et al., 2021). (**b**) δ^2H values of long-chain FAs (*n*C28:0 and *n*C30:0 FA).

By using the radiocarbon "bomb-spike" as a tracer, a recent study determined the down-core radiocarbon content of higher plant leaf wax lipids (long-chain FAs) in the Bengal Fan (French et al., 2018). The authors demonstrated that each terrestrial homologue must have at least two constituents, i.e., a fast-cycling component and a slow-cycling component. Model estimates suggest that nearly 80% of the leaf wax lipids in the Bengal Fan has an average age of 1,000-1,200 years while the remainder has an average age of 15 years (French et al., 2018). A similar work encompassing materials from the Cariaco Basin, Saanich Inlet, and Mackenzie Delta, has been later carried out by Vonk et al. (2019). Particularly, the estimate from the Mackenzie Delta indicates that the fast-cycling component (younger than 50 years) of leaf wax lipids may account for 58% in this region. These numbers are given by model estimates based on modern observations, and the percentage may change over times. In our case of very old long-chain FAs (Fig. 5.3a), the contribution from a fast-cycling component might have been smaller during the last deglaciation. Nevertheless, these studies indicate that the fast-cycling component has the potential to capture transient signals if the changes are large enough.

During the YD, the pre-depositional age of long-chain FAs in core ARA04C/37 was old but at least 3,000 years younger than during other periods of the deglaciation (Fig. 5.3a). In addition to long-chain FAs from the

permafrost soil, the erosive YD flood may have eroded more young carbon from topsoil via strengthened river-bank erosion, and resulted in a younger average age of long-chain FAs (Wu et al., 2021). Compared to other periods of the deglaciation, the YD interval may have increased contributions from the fast-cycling components. We therefore propose that the δ^2H_{wax} reduction recorded in the YD interval was attributed to a flood event. Because the slow-cycling component may have diluted the isotopic signals of the YD flood, we believe that the flood signal captured by fast-cycling components should be originally much larger.

Synchronous reduction of δ^2H_{wax} and δ^2H_{dino} (Fig. 5.2e and Fig. 5.2f) at the onset of the YD further constrains the freshwater sources. Our YD freshwater signal recorded in δ^2H_{wax} provides direct evidence that the YD-age freshening in the Beaufort Sea has significant water sources from the Mackenzie River. Another concern about the YD freshwater source is whether it was caused by enhanced LIS melting at the end of B/A interstadial or whether it was originated from proglacial Lake Agassiz (Wu et al., 2020). In particular, our results show distinctly sharp decreases of δ^2H_{wax} (6‰ in nC$_{28:0}$ FA and 4‰ in nC$_{30:0}$ FA) at the beginning of the YD (Fig. 5.3b; Table 5.2), whose original reduction may be even larger. Therefore, the δ^2H_{wax} reduction most likely reflects a meltwater outburst from the proglacial lakes which superimposed on a long-term decay of the LIS.

5.3.3 δ^2H-based salinity reconstruction for the YD flood: problems and perspectives

Salinity reconstructions based on the δ^2H_{dino}-salinity calibration can give an idea of the magnitude of the YD flood and provide further information for model simulations. However, due to the lack of region-specific salinity calibration for δ^2H_{dino}, such estimate can only be achieved by a predicted δ^2H_{dino}-salinity relationship. As the δ^2H_{dino} values are largely determined by the salinity-related δ^2H_{water} and the salinity-influenced fractionation factor ($\alpha_{dino\text{-}water}$=($\delta^2H_{dino}$+1000)/($\delta^2H_{water}$+1000)), the predicted δ^2H_{dino}-salinity relationship thus is established by the δ^2H_{water}-salinity and α-salinity relationships.

A global compilation of the $\alpha_{dino\text{-}water}$-salinity relationships, spanning salinities from 0 to 117 ppt, demonstrated a δ^2H_{dino} decrease of 0.7-1‰ per unit increase in salinity (Nelson and Sachs, 2014). Therefore, the $\alpha_{dino\text{-}water}$-salinity relationship is expressed in this study as:

$$\alpha_{dino\text{-}water} = 0.0007*S + 0.688 \quad (1)$$

where S is the sea surface salinity.

The δ^2H_{water}-salinity relationship is established based on the database of $\delta^{18}O_{water}$ and salinity in the Arctic Ocean (Schmidt et al., 1999), and the δ^2H_{water} can be derived from the global seawater relationship δ^2H_{water} = 7.23* $\delta^{18}O_{water}$ -1.54 (Craig and Gordon, 1965). However, due to the insufficient datasets especially in the low salinity conditions, the δ^2H_{water}-salinity relationship is less constrained in the Canadian Arctic (Fig. 5.4a). Since the pilot study successfully applied the eastern and central Arctic salinity calibration into the Canadian Arctic (Sachs et al., 2018), a similar δ^2H_{water}-salinity relationship can be expected between the western and eastern

Arctic. Hence, the δ^2H_{water}-salinity relationship in the eastern and central Arctic (Fig. 5.4b) is adopted for predicting δ^2H_{dino} in the Canadian Arctic. The δ^2H_{dino} is predicted based on the equation:

$$0.0007*S + 0.688 = (\delta^2H_{dino} + 1000) / (\delta^2H_{water} + 1000) \quad (2)$$

The predicted δ^2H_{dino} values are plotted with salinity (Fig. 5.4c), which can be expressed as:

$$\delta^2H_{dino} = 3.08*S - 397.61 \quad (3)$$

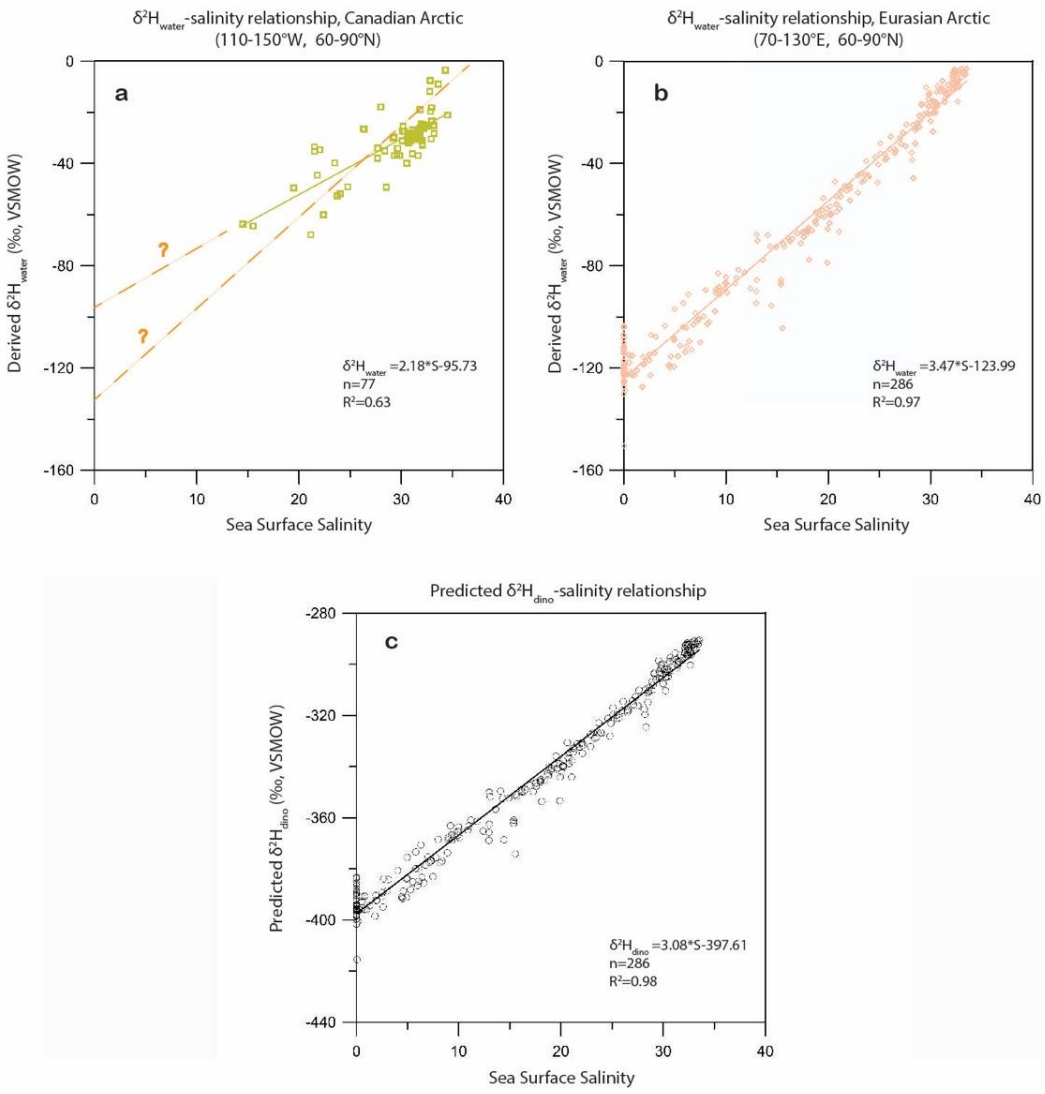

Figure 5.4 (**a**)-(**b**) Derived relationship of δ^2H_{water} vs. salinity in the Canadian Arctic (110-150 °W, 60-90 °N) and the Eurasian Arctic (70-130 °E, 60-90 °N). δ^2H_{water} data are derived from $\delta^{18}O$ values in surface water (0-10 m) (Schmidt et al., 1999). (**c**) Predicted relationship of δ^2H_{dino} vs. salinity for the Canadian Beaufort Sea, based on the relationship of δ^2H_{water} vs. salinity from the Eurasian Arctic.

Based on the predicted δ^2H_{dino}-salinity relationship (Eq. 3), the uppermost sample (δ^2H_{dino} = −327.4‰) from the late Holocene corresponds to a salinity of 22.8, which is close to the modern annual salinity of 24.8. The modern annual salinity is derived from the World Ocean Atlas 2013 (https://www.nodc.noaa.gov/OC5/woa13/). To estimate the relative changes in salinity, the Eq. 3 can be expressed as:

$$\Delta\delta^2H_{dino} = 3.08*\Delta S \quad (4)$$

where the $\Delta\delta^2H_{dino}$ and ΔS are the relative changes in δ^2H_{dino} and salinity between any two samples.

According to the Eq. 4, the salinity depression during the YD (compared to the modern/late Holocene) can be estimated as ~24, which is composed of ~20.5 from the YD to the early Holocene and of ~3.5 during the Holocene (Fig. 5.5). This salinity depression is much larger than the previous estimate of 8 from core PS72-291-2 (Sachs et al., 2018). If the Eq. 4 is valid during the deglaciation, such large depression in salinity may imply an almost complete freshwater environment over the core site when the peak YD flood occurred. However, one should keep in mind that the δ^2H_{water}-salinity relationship may change over times, particularly for the period of deglaciation. During the deglaciation, the colder climate and possibly more ^2H-depleted meltwater may have resulted in lower freshwater δ^2H end-member values and increased the slope in Eq.4, deriving in a smaller ΔS. Due to these uncertainties, it cannot be concluded yet whether the YD flood has caused a short completely freshwater dominated environment. A better salinity estimate needs further work to improve the regional calibration and corrections of possible deglacial effects. Nevertheless, compared to the salinity reconstruction from the short-chain FAs (Sachs et al., 2018), the δ^2H_{dino} record in core ARA04C/37 suggests a substantial salinity depression during the YD flood, which is much larger than we ever estimated.

5.3.4 Decreased Mackenzie River discharge during the mid-late Holocene

Both δ^2H_{dino} and $\delta^2H_{brassica}$ were more ^2H-depleted during the deglaciation and the early Holocene while values rebounded throughout the mid-late Holocene (Fig. 5.5b and Fig. 5.5c). It indicates a two-phase evolution of the past hydrology. During the deglaciation and the early Holocene, reduced δ^2H_{dino} and $\delta^2H_{brassica}$ most likely reflect the impact of LIS meltwater in the Mackenzie River basin and the Canadian Beaufort Sea. As the LIS retreated to its eastern sector during the early Holocene (Fig. 5.5a; Dalton et al., 2020; Dyke, 2004), the Hudson Strait has become the major outlet of LIS meltwater (Carlson et al., 2008; Jennings et al., 2015), while the meltwater influence on the Mackenzie River basin and the Canadian Beaufort Sea may have diminished (between ca. 10-8 cal. kyr BP). This is in agreement with a weakly laminated section in core ARA04C/37 (Fig. 5.5). In this context, the local precipitation and evaporation seem to have replaced meltwater as a more important role in hydrological changes since the middle Holocene.

During the mid-late Holocene (ca. 8-0 cal. kyr BP), salinity reconstruction based on δ^2H_{dino} suggests an increase of ~3.5 (Fig. 5.5b), which is similar to the estimate from core PS72/291-2 (Sachs et al., 2018). The increased δ^2H_{dino} and $\delta^2H_{brassica}$ most likely reflects a decreased Mackenzie River discharge that can be attributed to a

drier climate in the Arctic region. Less precipitation and/or more evaporation in the Mackenzie River basin may have resulted in more ^{2}H-concentrated freshwater. Besides, less runoff would result in higher salinity in the marine setting, and cause less $^{2}H/^{1}H$ fractionation during lipid synthesis (M'boule et al., 2014; Maloney et al., 2016; Sachs et al., 2016; Schouten et al., 2006; Weiss et al., 2017). The two factors additively induced increases in $\delta^{2}H_{dino}$ and $\delta^{2}H_{brassica}$.

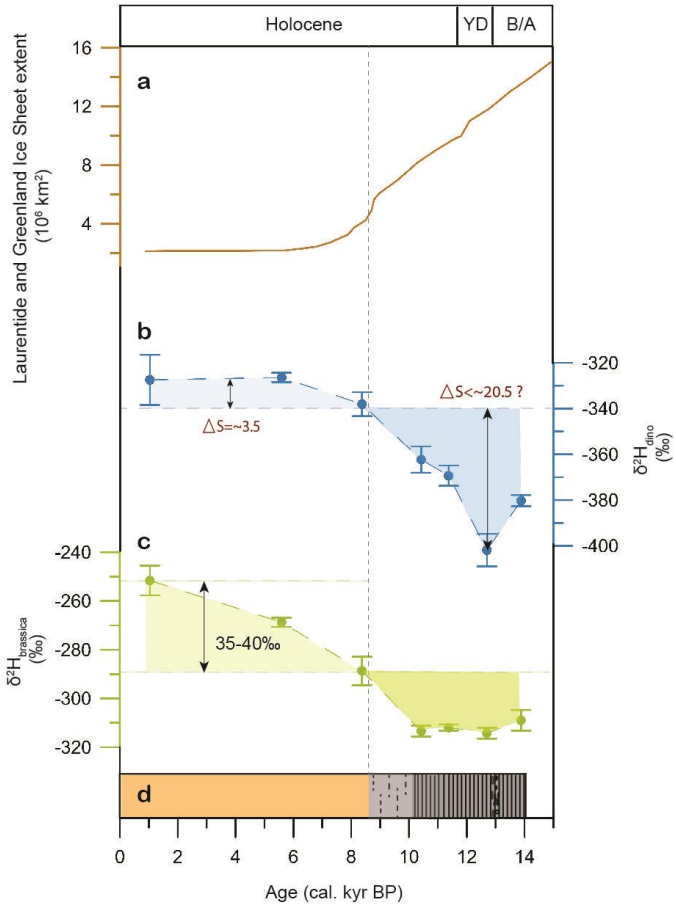

Figure 5.5 (**a**) The area of the Laurentide Ice Sheet and the Greenland Ice Sheet, data from Dalton et al. (2020). (**b**)-(**c**) $\delta^{2}H$ values of dinosterol and brassicaterol in core ARA04C/37. ΔS are the relative changes in the estimated salinity.

The drier climate is supported by model simulations. Model reconstructions suggested that the reduced Northeast-Pacific temperatures resulted in less atmospheric moisture transport into the Mackenzie drainage domain, which caused a moderate runoff decline of approximately 4-5% during the mid-late Holocene (Wagner et al., 2011). Another possible cause of drier climate may be related to the southward shift of westerly jet-stream. The Arctic cooling has increased the temperature gradient between the Equator and the pole since the middle Holocene (Routson et al., 2019). Such changes may have impacted the pressure gradient and shifted the westerly jet-stream southward (Xu et al., 2020). Proxy reconstruction and modeling of the Holocene rainfall patterns in China also support a gradually southward shift of the westerly jet-stream since the middle Holocene

(Herzschuh et al., 2019). Such hypothesis in the North America Arctic realm, however, needs higher resolution record and more comparison with other hydroclimate records.

5.4 Conclusion

In order to reconstruct paleo-hydrological changes, we analyzed a variety of δ^2H_{lipid} from the sediment core ARA04C/37, including the algal lipids, leaf wax lipids, and generic (short-chain) FAs. The records reflect hydrological changes in the Canadian Arctic, spanning the last 14 kyrs.

(1) The short-chain FAs show trendless variations in the entire records, and the YD flood signal is missing in these records. It might be attributed to substantially different δ^2H values of microbially-produced short-chain FAs, which have masked the YD flood signal. This explanation is supported by the relatively constant conventional radiocarbon ages of these short-chain FAs (2500-4400 ^{14}C years), that are much younger than the respective depositional ages. This indicates that the short-chain FAs have a different carbon source in comparison to other lipids, further implying a possibly different source of hydrogen.

(2) The cooccurrence of the strong YD freshwater signals (ca. 13.0 cal. kyr BP) in leaf wax lipid and marine phytoplankton sterol further constrains the freshwater source from proglacial lakes rather than solely enhanced LIS melting. Paleo-salinity reconstruction based on a predicted relationship between δ^2H_{dino} and salinity suggests a salinity depression of ~24 in surface water during the YD flood, which is larger than previous estimate (salinity depression of ~8) using δ^2H values of short-chain FAs.

(3) Values of δ^2H_{dino} and $\delta^2H_{brassica}$ have increased during the mid-late Holocene (8-0 cal. kyr BP), implying a decreased Mackenzie River discharge. As meltwater impact from the LIS has already diminished in the early Holocene, the decreased Mackenzie River discharge most likely resulted from a drier climate in the Canadian Arctic in the mid-late Holocene. Less moisture source from the Northeast Pacific and the southward shift of westerly jet-stream might be the cause of the drier climate.

Acknowledgements

We gratefully thank the professional support of the captain and crew of RV Araon on the expedition ARA04C in 2013. We thank Seung-Il Nam for providing the study material, and thanks to Jens Hefter for technical support during the laboratory work. We acknowledge the China Scholarship Council for financial support.

6. Conclusion and outlook

6.1 Conclusion

Within this thesis, one of the major objectives was to reconstruct the deglacial-Holocene sea-ice variability in the Canadian Beaufort Sea and decipher its controlling mechanisms. In addition, as the deglacial ice-sheet retreat was known to be driven by orbital forcing and the LIS is one of the most well-described ice sheets in the Northern Hemisphere, this region provides a great chance to learn the processes related to ice-sheet retreat and to assess their impacts on the climate system, including the ancient terrestrial OC mobilization and the meltwater release. To achieve this, biomarker analyses and compound-specific isotope analyses were carried out in sediment core ARA04C/37 from the Canadian Beaufort Sea off the Mackenzie River. Sea-ice biomarker IP_{25}, in combination with open-water phytoplankton biomarkers, was analyzed for a semiquantitative reconstruction of sea ice in this region. Besides, radiocarbon dating of OC and hydrogen isotope analyses of specific compounds were conducted to reconstruct the terrestrial OC mobilization and meltwater release, respectively.

Sea-ice variability in the Canadian Beaufort Sea since the last deglaciation has been described in chapter 3. During the deglaciation and early Holocene (14-8 kyr BP), the minimum concentrations of IP_{25} and low PIP_{25} point to nearly ice-free conditions. During the mid-late Holocene (8-0 kyr BP), elevated IP_{25} and PIP_{25} values reveal an evolution from dominantly ice-free conditions ($PIP_{25} < 0.2$) to extended sea-ice conditions ($PIP_{25} > 0.8$), following the decreasing summer insolation. As sea-ice expanded during the Holocene, the distinctive peaks in HBI-III suggest that the core site was first proximal to a MIZ situation during the cold seasons at ca. 5.6 kyr BP, and then the MIZ during warm seasons may have existed over the core site at ca. 3.5 kyr BP. These findings imply that summer insolation was probably the primary control on the sea-ice variability in the Canadian Beaufort Sea.

The relationship between glacial retreat and terrestrial OC mobilization during the deglaciation has been described in chapter 4. During the deglaciation, the enhanced terrestrial OC fluxes had a dominant source of ancient rock-derived OC (OC_{petro}), due to the glacial-retreat-induced physical erosion of bedrocks. This process had been estimated to release 84.3±30.4 PgC to the atmosphere. Besides, the increased carbon ages of $OC_{terr-bio}$ during the MWP 1a and 1b indicate strong coastal erosion triggered by rapid sea-level rise. The identification of this process is of significance to evaluate the impact of carbon release from the broad flooded permafrost of the Arctic shelves, which confirms that the carbon has been released in pulses. Model simulation suggests that the two processes additively have a long-term effect of an increase in atmospheric CO_2 of 12 ppm and a decrease in $\Delta^{14}C$-CO_2 of 12 permil. Ice-sheet retreat as a consequence of increased solar insolation played an active role in mobilizing and contributing the ancient terrestrial OC to the deglacial CO_2 rise.

Paleo hydrological changes in the Canadian Beaufort Sea have been reconstructed (chapter 5). The marine algal lipids brassicasterol and dinosterol show relatively low δ^2H values during the major phase of LIS melting (14-8 kyr BP), suggesting a significant impact of meltwater discharge in this region. Within this period, an

even stronger decrease in δ^2H_{dino} occurred at the onset of the YD (13 kyr BP). Based on a predicted relationship between δ^2H_{dino} and sea surface salinity, a salinity depression of ~24 has been reconstructed for this event. The extremely strong freshening during the YD most likely resulted from a catastrophic outburst from proglacial lakes (e.g., Lake Agassiz). The flood pathway via the Mackenzie River outlet is supported by the synchronously decreased δ^2H_{wax} values. During the mid-late Holocene (8-0 kyr BP), values of $\delta^2H_{brassica}$ and δ^2H_{dino} have increased, indicating less freshwater discharge from the Mackenzie River. As the impact of LIS meltwater has already diminished in the early Holocene, the decreased river discharge during the mid-late Holocene was most likely attributed to a drier climate in the river basin. Less moisture source from the Northeast Pacific and the southward shift of westerly jet-stream might be the cause of the drier climate.

The findings collectively describe a scenario that orbital forcing has reduced both sea-ice and ice-sheet extent in the Canadian Arctic region during the last deglaciation, and the ice-sheet retreat subsequently acted on the climate system in two ways. First, it mobilized OC_{petro} and permafrost carbon in direct and indirect ways and contributed to the deglacial CO_2 rise. Second, ice-sheet retreat may have opened the northwestern outlet of Lake Agassiz and released meltwater into the Arctic Ocean, and further to its outflow into the North Atlantic Ocean near the deep-water source area of the AMOC. This may have triggered the severe YD cooling. In summary, our study demonstrates the sensitivities of cryosphere components and their impact on climate change during the last deglaciation.

6.2 Outlook

The study of this thesis has reconstructed the history of sea ice, terrestrial OC input, and meltwater discharge in the Canadian Arctic region which complements the picture of Arctic change during the last deglaciation. However, this work still leaves challenges and opportunities for future studies.

Regarding the sea-ice reconstruction, the urgent need is to get more longer records in the Arctic Ocean. Although there are growing numbers of sea-ice records in recent years, the high-resolution sea-ice records covering the last deglaciation are still limited in numbers and regions, and thus more records are needed to better serve for models. In addition, the MIZ indicator HBI-III might be a promising biomarker to improve our reconstructions. Future work needs to verify its seasonality and feasibility as an indicator for MIZ. It may help to further outline the position of summer/winter sea-ice margin in the past and provide more constraints for sea-ice modeling.

The relationship between glacial retreat and OC_{petro} mobilization would be another promising research topic. Our study only estimated OC_{petro} release in western Canada, and estimates of OC_{petro} release in other ice-covered regions may help to evaluate the process and its impact on the climate system. Although in other regions (except western Canada), the distribution of shales (Copard et al., 2007) show few areas that were covered by ice sheets during the LGM, this process is still worth studying. A study from the Northeast Greenland continental shelf, where is expected to lack OC_{petro}, shows increased TOC content but extremely low concentrations of all biomarkers during the glacial retreat (Syring et al., 2020a). It most likely implies a

strong OC_{petro} input in this period, and this might be attributed to active paraglacial conditions and strong glacial erosion. Therefore, it is interesting to see what type of carbon dominated in these ice-covered regions and to assess their impact.

The occurrence of coastal erosion during the rapid sea-level rise has been identified in our records. However, model simulation suggests that the rate of sea-level rise is only one of the factors controlling coastal erosion (Barnhart et al., 2014; Overeem et al., 2011). Besides, the sea-ice condition and water temperature can also exert control on this process. Therefore, future studies may further investigate the influence of sea ice and water temperature on coastal erosion. Study areas can be chosen in regions characterized by strong sea-ice variability and in regions influenced by warm Atlantic Water.

Our study of low-resolution paleo-hydrology reconstruction in the Canadian Beaufort Sea leaves uncertainties. Certainly, a high-resolution study should follow to approve our promising results. Paleo-salinity reconstruction in our study is based on a predicted relationship between δ^2H_{dino} and salinity, therefore more surface sediment analyses are needed to provide better regional calibrations. Besides, the indication of δ^2H_{wax} in high latitude is of interest to discuss. Local empirical calibrations have established relationships between δ^2H_{wax} and δ^2H_p (precipitation), and recent compilation has placed these local calibrations in a global context (Liu and An, 2019; McFarlin et al., 2019). However, another global compilation of ^{14}C ages of leaf wax lipids suggests that the residence time of these lipids is controlled by climate and it increases (becomes older) with latitude (Eglinton et al., 2021). In addition, the permafrost in high latitudes can also increase the residence time. As the production of leaf wax lipids may be much earlier than their deposition, it raises concerns whether δ^2H_{wax} can be used for paleo-hydrology reconstruction in high latitude. More paired analyses of ^{14}C and δ^2H in leaf wax lipid may be necessary to answer these questions.

7. Reference

Aagaard, K., Carmack, E.C., 1989. The role of sea ice and other fresh water in the Arctic circulation. J. Geophys. Res. 94, 14485–14498.

Ackley, S.F., Sullivan, C.W., 1994. Physical controls on the development and characteristics of Antarctic sea ice biological communities-a review and synthesis. Deep. Res. Part I Oceanogr. Res. Pap. 41, 1583–1604.

Alley, R.B., Andrews, J.T., Brigham-Grette, J., Clarke, G.K.C., Cuffey, K.M., Fitzpatrick, J.J., Funder, S., Marshall, S.J., Miller, G.H., Mitrovica, J.X., Muhs, D.R., Otto-Bliesner, B.L., Polyak, L., White, J.W.C., 2010. History of the Greenland Ice Sheet: paleoclimatic insights. Quat. Sci. Rev. 29, 1728–1756.

Amante, C., Eakins, B.W., 2009. ETOPO1 1 Arc-Minute Global Relief Model: Procedures, Data Sources and Analysis. NOAA Tech. Memo. NESDIS NGDC-24 19.

Amiotte Suchet, P., Probst, J.-L., Ludwig, W., 2003. Worldwide distribution of continental rock lithology: Implications for the atmospheric/soil CO2 uptake by continental weathering and alkalinity river transport to the oceans. Global Biogeochem. Cycles 17, 1038.

Anderson, B.E., Burckle, L.H., 2009. Wind-Driven Upwelling in the Southern Ocean and the Deglacial Rise in Atmospheric CO2. Science. 323, 1443–1448.

Anderson, S.P., 2005. Glaciers show direct linkage between erosion rate and chemical weathering fluxes. Geomorphology 67, 147–157.

Andrews, J.T., Dunhill, G., 2004. Early to mid-Holocene Atlantic water influx and deglacial meltwater events, Beaufort Sea slope, Arctic Ocean. Quat. Res. 61, 14–21.

Bagniewski, W., Meissner, K.J., Menviel, L., 2017. Exploring the oxygen isotope fingerprint of Dansgaard-Oeschger variability and Heinrich events. Quat. Sci. Rev. 159, 1–14.

Barber, D.C., Dyke, A., Hillaire-Marcel, C., Jennings, A.E., Andrews, J.T., Kerwin, M.W., Bilodeau, G., McNeely, R., Southon, J., Morehead, M.D., Gagnon, J.M., 1999. Forcing of the cold event of 8,200 years ago by catastrophic drainage of Laurentide lakes. Nature 400, 344–348.

Bard, E., Hamelin, B., Delanghe-sabatier, D., 2010. Deglacial Meltwater Pulse 1B and Younger Dryas Sea Levels Revisited with Boreholes at Tahiti. Science. 327, 1235–1237.

Bareiss, J., Görgen, K., 2005. Spatial and temporal variability of sea ice in the Laptev Sea: Analyses and review of satellite passive-microwave data and model results, 1979 to 2002. Glob. Planet. Change 48, 28–54.

Barker, S., Knorr, G., 2021. Millennial scale feedbacks determine the shape and rapidity of glacial termination. Nat. Commun. 12, 1–12.

Barnhart, K.R., Anderson, R.S., Overeem, I., Wobus, C., Clow, G.D., Urban, F.E., 2014. Modeling erosion of ice-rich permafrost bluffs along the Alaskan Beaufort Sea coast. J. Geophys. Res. Earth Surf. 119, 1155–1179.

Batchelor, C.L., Margold, M., Krapp, M., Murton, D.K., Dalton, A.S., Gibbard, P.L., Stokes, C.R., Murton, J.B., Manica, A., 2019. The configuration of Northern Hemisphere ice sheets through the Quaternary. Nat. Commun. 10, 1–10.

Bauska, T.K., Baggenstos, D., Brook, E.J., Mix, A.C., Marcott, S.A., Petrenko, V. V., Schaefer, H., Severinghaus, J.P., Lee, J.E., Thiemens, M.H., 2016. Carbon isotopes characterize rapid changes in atmospheric carbon dioxide during the last deglaciation. Proc. Natl. Acad. Sci. U. S. A. 113, 3465–3470.

Belchansky, G.I., Douglas, D.C., 2002. Seasonal comparisons of sea ice concentration estimates derived from SSM/I, OKEAN, and RADARSAT data. Remote Sens. Environ. 81, 67–81.

Belt, S.T., Cabedo-Sanz, P., Smik, L., Navarro-Rodriguez, A., Berben, S.M.P., Knies, J., Husum, K., 2015. Identification of paleo Arctic winter sea ice limits and the marginal ice zone: Optimised biomarker-based reconstructions of late Quaternary Arctic sea ice. Earth Planet. Sci. Lett. 431, 127–139.

Belt, S.T., Massé, G., Rowland, S.J., Poulin, M., Michel, C., LeBlanc, B., 2007. A novel chemical fossil of palaeo sea ice: IP25. Org. Geochem. 38, 16–27.

Belt, S.T., Smik, L., Köseoglu, D., Knies, J., Husum, K., 2019. A novel biomarker-based proxy for the spring phytoplankton bloom in Arctic and sub-arctic settings – HBI T25. Earth Planet. Sci. Lett. 523, 115703.

Bird, M., Santrùcková, H., Lloyd, J., Lawson, E., 2002. The isotopic composition of soil organic carbon on a north-south transect in western Canada. Eur. J. Soil Sci. 53, 393–403.

Biskaborn, B.K., Smith, S.L., Noetzli, J., Matthes, H., Vieira, G., Streletskiy, D.A., Schoeneich, P., Romanovsky, V.E., Lewkowicz, A.G., Abramov, A., Allard, M., Boike, J., Cable, W.L., Christiansen, H.H., Delaloye, R., Diekmann, B., Drozdov, D., Etzelmüller, B., Grosse, G., Guglielmin, M., Ingeman-Nielsen, T., Isaksen, K., Ishikawa, M., Johansson, M., Johannsson, H., Joo, A., Kaverin, D., Kholodov, A., Konstantinov, P., Kröger, T., Lambiel, C., Lanckman, J.P., Luo, D., Malkova, G., Meiklejohn, I., Moskalenko, N., Oliva, M., Phillips, M., Ramos, M., Sannel, A.B.K., Sergeev, D., Seybold, C., Skryabin, P., Vasiliev, A., Wu, Q., Yoshikawa, K., Zheleznyak, M., Lantuit, H., 2019. Permafrost is warming at a global scale. Nat. Commun. 10, 1–11.

Blaauw, M., Christen, J.A., 2013. Bacon manual – v2.3.3.

Blaauw, M., Christeny, J.A., 2011. Flexible paleoclimate age-depth models using an autoregressive gamma process. Bayesian Anal. 6, 457–474.

Blaga, C.I., Reichart, G.J., Schouten, S., Lotter, A.F., Werne, J.P., Kosten, S., Mazzeo, N., Lacerot, G., Sinninghe Damsté, J.S., 2010. Branched glycerol dialkyl glycerol tetraethers in lake sediments: Can they be used as temperature and pH proxies? Org. Geochem. 41, 1225–1234.

Blattmann, T., 2021. Ideas and perspectives: Emerging contours of a dynamic exogenous kerogen cycle. Biogeosciences Discuss. in review.

Boden, P., Fairbanks, G., Wright, D., Burckle, H., 1997. High-resolution stable isotope records from southwest Sweden : The drainage of the Baltic Ice Lake and Younger Dryas ice margin oscillations. Paleoceanography 12, 39–49.

Bond, G.C., Lotti, R., 1995. Iceberg discharges into the North Atlantic on millennial time scales during the last glaciation. Science. 267, 1005–1010.

Boon, J.J., Rijpstra, W.I.C., De Lange, F., De Leeuw, J.W., Yoshioka, M., Shimizu, Y., 1979. Black Sea sterol-A molecular fossil for dinoflagellate blooms. Nature 277, 125–127.

Bouchez, J., Beyssac, O., Galy, V., Gaillardet, J., France-Lanord, C., Maurice, L., Moreira-Turcq, P., 2010. Oxidation of petrogenic organic carbon in the Amazon floodplain as a source of atmospheric CO2. Geology 38, 255–258.

Bova, S., Rosenthal, Y., Liu, Z., Godad, S.P., Yan, M., 2021. Seasonal origin of the thermal maxima at the Holocene and the last interglacial. Nature 589, 548–553.

Breckenridge, A., 2015. The Tintah-Campbell gap and implications for glacial Lake Agassiz drainage during the Younger Dryas cold interval. Quat. Sci. Rev. 117, 124–134.

Bröder, L., Keskitalo, K., Zolkos, S., Shakil, S., Tank, S.E., Kokelj, S. V., Tesi, T., Dongen, B.E. van, Haghipour, N., Eglinton, T.I., Vonk, J.E., 2021. Preferential export of permafrost-derived organic matter as retrogressive thaw slumping intensifies. Environ. Res. Lett. 10, 1–16.

Bröder, L., Tesi, T., Andersson, A., Eglinton, T.I., Semiletov, I.P., Dudarev, O. V., Roos, P., Gustafsson, Ö., 2016. Historical records of organic matter supply and degradation status in the East Siberian Sea. Org. Geochem. 91, 16–30.

Broecker, W.S., 2006. Was the Younger Dryas triggered by a flood? Science. 312, 1146–1148.

Broecker, W.S., Kennett, J.P., Flower, B.P., Teller, J.T., Trumbore, S., Bonani, G., Wolfli, W., 1989. Routing of meltwater from the Laurentide Ice Sheet during the Younger Dryas cold episode. Nature 341, 318–321.

Broecker, W.S., Peteet, D.M., Rind, D., 1985. Does the ocean-atmosphere system have more than one stable mode of operation? Nature 315, 21–26.

Brown, T.A., Belt, S.T., 2016. Novel tri- and tetra-unsaturated highly branched isoprenoid (HBI) alkenes from the marine diatom Pleurosigma intermedium. Org. Geochem. 91, 120–122.

Brown, T.A., Belt, S.T., Philippe, B., Mundy, C.J., Massé, G., Poulin, M., Gosselin, M., 2011. Temporal and vertical variations of lipid biomarkers during a bottom ice diatom bloom in the Canadian Beaufort Sea: Further evidence for the use of the IP25biomarker as a proxy for spring Arctic sea ice. Polar Biol. 34, 1857–1868.

Brown, T.A., Belt, S.T., Tatarek, A., Mundy, C.J., 2014. Source identification of the Arctic sea ice proxy IP 25. Nat. Commun. 5, 4197.

Campeau, A., Soerensen, A., Martma, T., Åkerblom, S., Zdanowicz, C., 2020. Controls on the 14 C-content of dissolved and particulate organic carbon mobilized across the Mackenzie River basin, Canada. Global Biogeochem. Cycles 34, e2020GB006671.

Carlson, A.E., Legrande, A.N., Oppo, D.W., Came, R.E., Schmidt, G.A., Anslow, F.S., Licciardi, J.M., Obbink, E.A., 2008. Rapid early Holocene deglaciation of the Laurentide ice sheet. Nat. Geosci. 1, 620–624.

Carmack, E., Robie Macdonald, W., Steve, J., 2004. Phytoplankton productivity on the Canadian Shelf of the Beaufort Sea. Mar. Ecol. Prog. Ser. 277, 37–50.

Carmack, E.C., Yamamoto-Kawai, M., Haine, T.W.N., Bacon, S., Bluhm, B.A., Lique, C., Melling, H., Polyakov, I. V., Straneo, F., Timmermans, M.L., Williams, W.J., 2016. Freshwater and its role in the Arctic Marine System: Sources, disposition, storage, export, and physical and biogeochemical consequences in the Arctic and global oceans. J. Geophys. Res. G Biogeosciences 121, 675–717.

Cerling, T.E., Harris, J.M., MacFadden, B.J., Leakey, M.G., Quade, J., Eisenmann, V., Ehieringer, J.R., 1997. Global vegetation change through the Miocene/Pliocene boundary. Nature 389, 153–158.

Clark, P.U., Dyke, A.S., Shakun, J.D., Carlson, A.E., Clark, J., Wohlfarth, B., Mitrovica, J.X., Hostetler, S.W., McCabe, A.M., 2009. The Last Glacial Maximum. Science. 325, 710–714.

Collins, L.G., Allen, C.S., Pike, J., Hodgson, D.A., Weckström, K., Massé, G., 2013. Evaluating highly branched isoprenoid (HBI) biomarkers as a novel Antarctic sea-ice proxy in deep ocean glacial age sediments. Quat. Sci. Rev. 79, 87–98.

Comiso, J.C., Meier, W.N., Gersten, R., 2017. Variability and trends in the Arctic Sea ice cover: Results from different techniques. J. Geophys. Res. Ocean. 122, 6883–6900.

Copard, Y., Amiotte-Suchet, P., Di-Giovanni, C., 2007. Storage and release of fossil organic carbon related to weathering of sedimentary rocks. Earth Planet. Sci. Lett. 258, 345–357.

Copard, Y., Di-Giovanni, C., Martaud, T., Albéric, P., Olivier, J.E., 2006. Using Rock-Eval 6 pyrolysis for tracking fossil organic carbon in modern environments: Implications for the roles of erosion and weathering. Earth Surf. Process. Landforms 31, 135–153.

Coupel, P., Matsuoka, A., Ruiz-Pino, D., Gosselin, M., Marie, D., Tremblay, J.E., Babin, M., 2015. Pigment signatures of phytoplankton communities in the Beaufort Sea. Biogeosciences 12, 991–1006.

Craig, H., Gordon, L.I., 1965. Deuterium and oxygen 18 variations in the ocean and the marine atmosphere.

Cremer, H., 1999. Distribution patterns of diatom surface sediment assemblages in the Laptev Sea (Arctic Ocean). Mar. Micropaleontol. 38, 39–67.

Cui, X., Bianchi, T.S., Jaeger, J.M., Smith, R.W., 2016. Biospheric and petrogenic organic carbon flux along southeast Alaska. Earth Planet. Sci. Lett. 452, 238–246.

Dai, A., Luo, D., Song, M., Liu, J., 2019. Arctic amplification is caused by sea-ice loss under increasing CO2. Nat. Commun. 10, 1–13.

Dalton, A.S., Margold, M., Stokes, C.R., Tarasov, L., Dyke, A.S., Adams, R.S., Allard, S., Arends, H.E., Atkinson, N., Attig, J.W., Barnett, P.J., Barnett, R.L., Batterson, M., Bernatchez, P., Borns, H.W., Breckenridge, A., Briner, J.P., Brouard, E., Campbell, J.E., Carlson, A.E., Clague, J.J., Curry, B.B., Daigneault, R.A., Dubé-Loubert, H., Easterbrook, D.J., Franzi, D.A., Friedrich, H.G., Funder, S., Gauthier, M.S., Gowan, A.S., Harris, K.L., Hétu, B., Hooyer, T.S., Jennings, C.E., Johnson, M.D., Kehew, A.E., Kelley, S.E., Kerr, D., King, E.L., Kjeldsen, K.K., Knaeble, A.R., Lajeunesse, P., Lakeman, T.R., Lamothe, M., Larson, P., Lavoie, M., Loope, H.M., Lowell, T. V., Lusardi, B.A., Manz, L., McMartin, I., Nixon, F.C., Occhietti, S., Parkhill, M.A., Piper, D.J.W., Pronk, A.G., Richard, P.J.H., Ridge, J.C., Ross, M., Roy, M., Seaman, A., Shaw, J., Stea, R.R., Teller, J.T., Thompson, W.B., Thorleifson, L.H., Utting, D.J., Veillette, J.J., Ward, B.C., Weddle, T.K., Wright, H.E., 2020. An updated radiocarbon-based ice margin chronology for the last deglaciation of the North American Ice Sheet Complex. Quat. Sci. Rev. 234, 106223.

de Bar, M.W., Dorhout, D.J.C., Hopmans, E.C., Rampen, S.W., Sinninghe Damsté, J.S., Schouten, S., 2016. Constraints on the application of long chain diol proxies in the Iberian Atlantic margin. Org. Geochem.

101, 184–195.

De Jonge, C., Stadnitskaia, A., Hopmans, E.C., Cherkashov, G., Fedotov, A., Sinninghe Damsté, J.S., 2014. In situ produced branched glycerol dialkyl glycerol tetraethers in suspended particulate matter from the Yenisei River, Eastern Siberia. Geochim. Cosmochim. Acta 125, 476–491.

Desvilettes, C., Bourdier, G., Amblard, C., Barth, B., 1997. Use of fatty acids for the assessment of zooplankton grazing on bacteria, protozoans and microalgae. Freshw. Biol. 38, 629–637.

Divine, D. V., Korsnes, R., Makshtas, A.P., 2004. Temporal and spatial variation of shore-fast ice in the Kara Sea. Cont. Shelf Res. 24, 1717–1736.

Douglas, P.M.J., Pagani, M., Eglinton, T.I., Brenner, M., Hodell, D.A., Curtis, J.H., Ma, K.F., Breckenridge, A., 2014. Pre-aged plant waxes in tropical lake sediments and their influence on the chronology of molecular paleoclimate proxy records. Geochim. Cosmochim. Acta 141, 346–364.

Drenzek, N.J., Hughen, K.A., Montlucecon, D.B., Southon, J.R., dos Santos, G.M., Druffel, E.R.M., Giosan, L., Eglinton, T.I., 2009. A new look at old carbon in active margin sediments. Geology 37, 239–242.

Drenzek, N.J., Montluçon, D.B., Yunker, M.B., Macdonald, R.W., Eglinton, T.I., 2007. Constraints on the origin of sedimentary organic carbon in the Beaufort Sea from coupled molecular 13C and 14C measurements. Mar. Chem. 103, 146–162.

Duk-Rodkin, A., Hughes, O.L., 1994. Tertiary-quaternary drainage of the Pre-glacial Mackenzie basin. Quat. Int. 22–23, 221–241.

Dyke, A.S., 2004. An outline of North American deglaciation with emphasis on central and northern Canada. Dev. Quat. Sci. 2, 373–424.

Dyke, A.S., Dale, J.E., McNeely, R.N., 1996. Marine molluscs as indicators of environmental change in glaciated North America and greenland during the last 18 000 Years. Geogr. Phys. Quat. 50, 125–184.

Dyke, A.S., Moore, A., Robertson, L., 2003. Deglaciation of North America: Thirty-two digital maps at 1:7,000,000 scale with accompanying digital chronolog- ical database and one poster (two sheets) with full map series. Geol. Surv. Can. Open File 1574. https://doi.org/10.4095/214399

Dyke, A.S., Savelle, J.M., 2001. Holocene History of the Bering Sea Bowhead Whale (Balaena Mysticetus) in Its Beaufort Sea Summer Grounds off Southwestern Victoria Island, Western Canadian Arctic. Quat. Res. 55, 371–379.

Dyonisius, M.N., Petrenko, V. V., Smith, A.M., Hua, Q., Yang, B., Schmitt, J., Beck, J., Seth, B., Bock, M., Hmiel, B., Vimont, I., Menking, J.A., Shackleton, S.A., Baggenstos, D., Bauska, T.K., Rhodes, R.H., Sperlich, P., Beaudette, R., Harth, C., Kalk, M., Brook, E.J., Fischer, H., Severinghaus, J.P., Weiss, R.F., 2020. Old carbon reservoirs were not important in the deglacial methane budget. Science. 367, 907–910.

Eglinton, T.I., Aluwihare, L.I., Bauer, J.E., Druffel, E.R.M., McNichol, A.P., 1996. Gas chromatographic isolation of individual compounds from complex matrices for radiocarbon dating. Anal. Chem. 68, 904–912.

Eglinton, T.I., Eglinton, G., 2008. Molecular proxies for paleoclimatology. Earth Planet. Sci. Lett. 275, 1–16.

Eglinton, T.I., Galy, V. V., Hemingway, J.D., Feng, X., Bao, H., Blattmann, T.M., Dickens, A.F., Gies, H.,

Giosan, L., Haghipour, N., Hou, P., Lupker, M., McIntyre, C.P., Montluçon, D.B., Peucker-Ehrenbrink, B., Ponton, C., Wacker, L., Schefuß, E., Schwab, M.S., Voss, B.M., Wu, Y., Zhao, M., 2021. Climate control on terrestrial biospheric carbon turnover. Proc. Natl. Acad. Sci. 118, e2011585118.

Ehlers, J., Gibbard, P.L., 2007. The extent and chronology of Cenozoic Global Glaciation. Quat. Int. 164–165, 6–20.

England, J.H., Furze, M.F.A., 2008. New evidence from the western Canadian Arctic Archipelago for the resubmergence of Bering Strait. Quat. Res. 70, 60–67.

Espitalie, J., Madec, M., Tissot, B., Mennig, J.J., Leplat, P., 1977. Source rock characterization method for petroleum exploration. Offshore Technology Conference. pp. 439–443.

Fagel, N., Not, C., Gueibe, J., Mattielli, N., Bazhenova, E., 2014. Late Quaternary evolution of sediment provenances in the Central Arctic Ocean: Mineral assemblage, trace element composition and Nd and Pb isotope fingerprints of detrital fraction from the Northern Mendeleev Ridge. Quat. Sci. Rev. 92, 140–154.

Fahl, K., Stein, R., 2012. Modern seasonal variability and deglacial/Holocene change of central Arctic Ocean sea-ice cover: New insights from biomarker proxy records. Earth Planet. Sci. Lett. 351, 123–133.

Fahl, K., Stein, R., 1999. Biomarkers as organic-carbon-source and environmental indicators in the late quaternary Arctic Ocean: Problems and perspectives. Mar. Chem. 63, 293–309.

Fahl, K., Stein, R., Gaye-Haake, B., Gebhardt, C., Kodina, L.A., Unger, D., Ittekkot, V., 2003. Biomarkers in surface sediments from Ob and Yenisei estuaries and southern Kara Sea: evidence for particulate organic carbon sources, pathways, and degradation. Siberian River Run-off in the Kara Sea: Characterisation, Quantification, Variability, and Environmental Significance. Elsevier, Amsterdam, pp. 329–348.

Fietz, S., Huguet, C., Rueda, G., Hambach, B., Rosell-Melé, A., 2013. Hydroxylated isoprenoidal GDGTs in the Nordic Seas. Mar. Chem. 152, 1–10.

Firestone, R.B., West, A., Kennett, J.P., Becker, L., Bunch, T.E., Revay, Z.S., Schultz, P.H., Belgya, T., Kennett, D.J., Erlandson, J.M., Dickenson, O.J., Goodyear, A.C., Harris, R.S., Howard, G.A., Kloosterman, J.B., Lechler, P., Mayewski, P.A., Montgomery, J., Poreda, R., Darrah, T., Que Hee, S.S., Smitha, A.R., Stich, A., Topping, W., Wittke, J.H., Wolbach, W.S., 2007. Evidence for an extraterrestrial impact 12,900 years ago that contributed to the megafaunal extinctions and the Younger Dryas cooling. Proc. Natl. Acad. Sci. U. S. A. 104, 16016–16021.

Fisher, T.G., Lowell, T. V., 2012. Testing northwest drainage from Lake Agassiz using extant ice margin and strandline data. Quat. Int. 260, 106–114.

Fisher, T.G., Smith, D.G., Andrews, J.T., 2002. Preboreal oscillation caused by a glacial Lake Agassiz flood. Quat. Sci. Rev. 21, 873–878.

Fisher, T.G., Waterson, N., Lowell, T. V., Hajdas, I., 2009. Deglaciation ages and meltwater routing in the Fort McMurray region, northeastern Alberta and northwestern Saskatchewan, Canada. Quat. Sci. Rev. 28, 1608–1624.

French, K.L., Hein, C.J., Haghipour, N., Wacker, L., Kudrass, H.R., Eglinton, T.I., Galy, V., 2018. Millennial soil retention of terrestrial organic matter deposited in the Bengal Fan. Sci. Rep. 8, 1–8.

Galy, V., Eglinton, T., 2011. Protracted storage of biospheric carbon in the Ganges-Brahmaputra basin. Nat. Geosci. 4, 843–847.

Gamboa, A., Montero-Serrano, J.-C., St-Onge, G., Rochon, A., Desiage, P.-A., 2017. Mineralogical, geochemical, and magnetic signatures of surface sediments from the Canadian Beaufort Shelf and Amundsen Gulf (Canadian Arctic). Geochemistry, Geophysics, Geosystems 18, 488–512.

Goñi, M.A., Yunker, M.B., Macdonald, R.W., Eglinton, T.I., 2005. The supply and preservation of ancient and modern components of organic carbon in the Canadian Beaufort Shelf of the Arctic Ocean. Mar. Chem. 93, 53–73.

Grotheer, H., Meyer, V., Riedel, T., Hefter, J., Gentz, T., Mollenhauer, G., Fritz, M., 2020. Burial and origin of permafrost derived carbon in the nearshore zone of the southern Canadian Beaufort Sea. Geophys. Res. Lett. 47, e2019GL085897.

Häggi, C., Schefuß, E., Sawakuchi, A.O., Chiessi, C.M., Mulitza, S., Bertassoli, D.J., Hefter, J., Zabel, M., Baker, P.A., Schouten, S., 2019. Modern and late Pleistocene particulate organic carbon transport by the Amazon River: Insights from long-chain alkyl diols. Geochim. Cosmochim. Acta 262, 1–19.

Harrison, S., Smith, D.E., Glasser, N.F., 2019. Late Quaternary meltwater pulses and sea level change. J. Quat. Sci. 34, 1–15.

Heaton, T.J., Köhler, P., Butzin, M., Bard, E., Reimer, R.W., Austin, W.E.N., Bronk Ramsey, C., Grootes, P.M., Hughen, K.A., Kromer, B., Reimer, P.J., Adkins, J., Burke, A., Cook, M.S., Olsen, J., Skinner, L.C., 2020. Marine20 - The Marine Radiocarbon Age Calibration Curve (0-55,000 cal BP). Radiocarbon 62, 779–820.

Hein, C.J., Usman, M., Eglinton, T.I., Haghipour, N., Galy, V. V., 2020. Millennial-scale hydroclimate control of tropical soil carbon storage. Nature 581, 63–66.

Hemingway, J.D., Hilton, R.G., Hovius, N., Eglinton, T.I., Haghipour, N., Wacker, L., Chen, M.C., Galy, V. V., 2018. Microbial oxidation of lithospheric organic carbon in rapidly eroding tropical mountain soils. Science. 360, 209–212.

Herzschuh, U., Cao, X., Laepple, T., Dallmeyer, A., Telford, R.J., Ni, J., Chen, F., Kong, Z., Liu, G., Liu, K.B., Liu, X., Stebich, M., Tang, L., Tian, F., Wang, Y., Wischnewski, J., Xu, Q., Yan, S., Yang, Z., Yu, G., Zhang, Y., Zhao, Y., Zheng, Z., 2019. Position and orientation of the westerly jet determined Holocene rainfall patterns in China. Nat. Commun. 10, 1–8.

Hill, J.C., Driscoll, N.W., 2008. Paleodrainage on the Chukchi shelf reveals sea level history and meltwater discharge. Mar. Geol. 254, 129–151.

Hilton, R.G., Gaillardet, J.Ô., Calmels, D., Birck, J.L., 2014. Geological respiration of a mountain belt revealed by the trace element rhenium. Earth Planet. Sci. Lett. 403, 27–36.

Hilton, R.G., Galy, V., Gaillardet, J., Dellinger, M., Bryant, C., O'Regan, M., Gröcke, D.R., Coxall, H., Bouchez, J., Calmels, D., 2015. Erosion of organic carbon in the Arctic as a geological carbon dioxide sink. Nature 524, 84–87.

Hilton, R.G., West, A.J., 2020. Mountains, erosion and the carbon cycle. Nat. Rev. Earth Environ. 1, 284–299.

Holmes, R.M., McClelland, J.W., Peterson, B.J., Shiklomanov, I.A., Shiklomanov, A.I., Zhulidov, A. V., Gordeev, V. V., Bobrovitskaya, N.N., 2002. A circumpolar perspective on fluvial sediment flux to the Arctic ocean. Global Biogeochem. Cycles 16, 1098.

Hopmans, E.C., Weijers, J.W.H., Schefuß, E., Herfort, L., Sinninghe Damsté, J.S., Schouten, S., 2004. A novel proxy for terrestrial organic matter in sediments based on branched and isoprenoid tetraether lipids. Earth Planet. Sci. Lett. 224, 107–116.

Horan, K., Hilton, R.G., Dellinger, M., Tipper, E., Galy, V., Calmels, D., Selby, D., Gaillardet, J., Ottley, C.J., Parsons, D.R., Burton, K.W., 2019. Carbon dioxide emissions by rock organic carbon oxidation and the net geochemical carbon budget of the Mackenzie River Basin. Am. J. Sci. 319, 473–499.

Horan, K., Hilton, R.G., Selby, D., Ottley, C.J., Gröcke, D.R., Hicks, M., Burton, K.W., 2017. Mountain glaciation drives rapid oxidation of rock-bound organic carbon. Sci. Adv. 3, e1701107.

Hörner, T., Stein, R., Fahl, K., Birgel, D., 2016. Post-glacial variability of sea ice cover, river run-off and biological production in the western Laptev Sea (Arctic Ocean) - A high-resolution biomarker study. Quat. Sci. Rev. 143, 133–149.

Hugelius, G., Strauss, J., Zubrzycki, S., Harden, J.W., Schuur, E.A.G., Ping, C.L., Schirrmeister, L., Grosse, G., Michaelson, G.J., Koven, C.D., O'Donnell, J.A., Elberling, B., Mishra, U., Camill, P., Yu, Z., Palmtag, J., Kuhry, P., 2014. Estimated stocks of circumpolar permafrost carbon with quantified uncertainty ranges and identified data gaps. Biogeosciences 11, 6573–6593.

Isaksson, E., Kohler, J., Pohjola, V., Moore, J., Igarashi, M., Karlofj, L., Martma, T., Meijer, H., Motoyama, H., Vaikm, R., Wal, R.S.W. Van De, 2005. Two ice-core δ18O records from Svalbard illustrating climate and sea-ice variability over the last 400 years. The Holocene 15, 501–509.

Jakobsson, M., Mayer, L., Coakley, B., Dowdeswell, J.A., Forbes, S., Fridman, B., Hodnesdal, H., Noormets, R., Pedersen, R., Rebesco, M., Schenke, H.W., Zarayskaya, Y., Accettella, D., Armstrong, A., Anderson, R.M., Bienhoff, P., Camerlenghi, A., Church, I., Edwards, M., Gardner, J. V., Hall, J.K., Hell, B., Hestvik, O., Kristoffersen, Y., Marcussen, C., Mohammad, R., Mosher, D., Nghiem, S. V., Pedrosa, M.T., Travaglini, P.G., Weatherall, P., 2012. The International Bathymetric Chart of the Arctic Ocean (IBCAO) Version 3.0. Geophys. Res. Lett. 39, L12609.

Jakobsson, M., Pearce, C., Cronin, T.M., Backman, J., Anderson, L.G., Barrientos, N., Björk, G., Coxall, H., Boer, A. De, Mayer, L.A., Mörth, C., Nilsson, J., Rattray, J.E., Stranne, C., Semiletov, I., Regan, M.O., 2017. Post-glacial flooding of the Bering Land Bridge dated to 11 cal ka BP based on new geophysical and sediment records. Clim. Past 13, 991–1005.

Jennings, A., Andrews, J., Pearce, C., Wilson, L., Ólfasdóttir, S., 2015. Detrital carbonate peaks on the Labrador shelf, a 13-7ka template for freshwater forcing from the Hudson Strait outlet of the Laurentide Ice Sheet into the subpolar gyre. Quat. Sci. Rev. 107, 62–80.

Jin, Y.K., 2013. ARA04C Cruise Report: Barrow, US - Beaufort Sea, CAN - Nome, US 6-24 September, 2013. Incheon.

Johnston, D.T., MacDonald, F.A., Gill, B.C., Hoffman, P.F., Schrag, D.P., 2012. Uncovering the neoproterozoic

carbon cycle. Nature 483, 320–323.

Kandasamy, S., Nath, B.N., 2016. Perspectives on the terrestrial organic matter transport and burial along the land-deep sea continuum: Caveats in our understanding of biogeochemical processes and future needs. Front. Mar. Sci. 3, 259.

Kaufman, D.S., Ager, T.A., Anderson, N.J., Anderson, P.M., Andrews, J.T., Bartlein, P.J., Brubaker, L.B., Coats, L.L., Cwynar, L.C., Duvall, M.L., Dyke, A.S., Edwards, M.E., Eisner, W.R., Gajewski, K., Geirsdóttir, A., Hu, F.S., Jennings, A.E., Kaplan, M.R., Kerwin, M.W., Lozhkin, A. V., MacDonald, G.M., Miller, G.H., Mock, C.J., Oswald, W.W., Otto-Bliesner, B.L., Porinchu, D.F., Rühland, K., Smol, J.P., Steig, E.J., Wolfe, B.B., 2004. Holocene thermal maximum in the western Arctic (0-180°W). Quat. Sci. Rev. 23, 529–560.

Keigwin, L.D., Donnelly, J.P., Cook, M.S., Driscoll, N.W., Brigham-Grette, J., 2006. Rapid sea-level rise and Holocene climate in the Chukchi Sea. Geology 34, 861–864.

Keigwin, L.D., Klotsko, S., Zhao, N., Reilly, B., Giosan, L., Driscoll, N.W., 2018. Deglacial floods in the Beaufort Sea preceded Younger Dryas cooling. Nat. Geosci. 11, 599–604.

Keller, C.K., Bacon, D.H., 1998. Soil respiration and georespiration distinguished by transport analyses of vadose CO2, 13CO2, and 14CO2. Global Biogeochem. Cycles 12, 361–372.

Keskitalo, K., Tesi, T., Bröder, L., Andersson, A., Pearce, C., Sköld, M., Semiletov, I.P., Dudarev, O. V., Gustafsson, Ö., 2017. Sources and characteristics of terrestrial carbon in Holocene-scale sediments of the East Siberian Sea. Clim. Past 13, 1213–1226.

Kim, K., Kim, Ji-young, Kim, Jinju, Yeo, S., Na, H., Hamlington, B.D., Leben, R.R., 2019. Vertical Feedback Mechanism of Winter Arctic Amplification and Sea Ice Loss. Sci. Rep. 9, 1–10.

Klotsko, S., Driscoll, N., Keigwin, L., 2019. Multiple meltwater discharge and ice rafting events recorded in the deglacial sediments along the Beaufort Margin, Arctic Ocean. Quat. Sci. Rev. 203, 185–208.

Köhler, P., Knorr, G., Bard, E., 2014. Permafrost thawing as a possible source of abrupt carbon release at the onset of the Bølling/Allerød. Nat. Commun. 5, 5520.

Köhler, P., Nehrbass-Ahles, C., Schmitt, J., Stocker, T.F., Fischer, H., 2017. A 156 kyr smoothed history of the atmospheric greenhouse gases CO2, CH4, and N2O and their radiative forcing. Earth Syst. Sci. Data 9, 363–387.

Kohn, M.J., 2010. Carbon isotope compositions of terrestrial C3 plants as indicators of (paleo)ecology and (paleo)climate. Proc. Natl. Acad. Sci. U. S. A. 107, 19691–19695.

Kolling, H.M., 2017. Decadal to centennial variability of (sub-) Arctic sea ice distribution and its paleoenvironmental significance. University of Bremen. PhD dissertation.

Kremer, A., 2018. The variability of sea ice in the Fram Strait throughout glacial-interglacial transitions of the Late Quaternary (MIS 11 to MIS 1). University of Bremen. PhD dissertation.

Kusch, S., Mollenhauer, G., Willmes, C., Hefter, J., Eglinton, T.I., Galy, V., 2021. Controls on the age of plant waxes in marine sediments – A global synthesis. Org. Geochem. 157, 104259.

Kusch, S., Rethemeyer, J., Schefuß, E., Mollenhauer, G., 2010. Controls on the age of vascular plant

biomarkers in Black Sea sediments. Geochim. Cosmochim. Acta 74, 7031–7047.

Ladd, S.N., Maloney, A.E., Nelson, D.B., Prebble, M., Camperio, G., Sear, D.A., Hassall, J.D., Langdon, P.G., Sachs, J.P., Dubois, N., 2021. Leaf Wax Hydrogen Isotopes as a Hydroclimate Proxy in the Tropical Pacific. J. Geophys. Res. Biogeosciences 126, e2020JG005891.

Lambeck, K., Rouby, H., Purcell, A., Sun, Y., Sambridge, M., 2014. Sea level and global ice volumes from the Last Glacial Maximum to the Holocene. Proc. Natl. Acad. Sci. U. S. A. 111, 15296–15303.

Lantuit, H., Overduin, P.P., Couture, N., Wetterich, S., Aré, F., Atkinson, D., Brown, J., Cherkashov, G., Drozdov, D., Donald Forbes, L., Graves-Gaylord, A., Grigoriev, M., Hubberten, H.W., Jordan, J., Jorgenson, T., Ødegård, R.S., Ogorodov, S., Pollard, W.H., Rachold, V., Sedenko, S., Solomon, S., Steenhuisen, F., Streletskaya, I., Vasiliev, A., 2012. The Arctic Coastal Dynamics Database: A New Classification Scheme and Statistics on Arctic Permafrost Coastlines. Estuaries and Coasts 35, 383–400.

Laskar, J., Robutel, P., Joutel, F., Gastineau, M., Correia, A.C.M., Levrard, B., 2004. A long-term numerical solution for the insolation quantities of the Earth. Astron. Astrophys. 428, 261–285.

Lattaud, J., Dorhout, D., Schulz, H., Castañeda, I.S., Sinninghe Damsté, J.S., Schouten, S., 2017a. The C32 alkane-1,15-diol as a proxy of late Quaternary riverine input in coastal margins. Clim. Past 13, 1049–1061.

Lattaud, J., Kim, J.H., De Jonge, C., Zell, C., Sinninghe Damsté, J.S., Schouten, S., 2017b. The C32 alkane-1,15-diol as a tracer for riverine input in coastal seas. Geochim. Cosmochim. Acta 202, 146–158.

Levy, L.B., Larsen, N.K., Davidson, T.A., Strunk, A., Olsen, J., Jeppesen, E., 2017. Contrasting evidence of Holocene ice margin retreat, south-western Greenland. J. Quat. Sci. 32, 604–616.

Leydet, D.J., Carlson, A.E., Teller, J.T., Breckenridge, A., Barth, A.M., Ullman, D.J., Sinclair, G., Milne, G.A., Cuzzone, J.K., Caffee, M.W., 2018. Opening of glacial Lake Agassiz's eastern outlets by the start of the Younger Dryas cold period. Geology 46, 155–158.

Lin, Y., Hibbert, F.D., Whitehouse, P.L., Woodroffe, S.A., Purcell, A., Shennan, I., Bradley, S.L., 2021. A reconciled solution of Meltwater Pulse 1A sources using sea-level fingerprinting. Nat. Commun. 12, 1–11.

Liu, J., An, Z., 2019. Variations in hydrogen isotopic fractionation in higher plants and sediments across different latitudes: Implications for paleohydrological reconstruction. Sci. Total Environ. 650, 470–478.

Liu, Z., Zhu, J., Rosenthal, Y., Zhang, X., Otto-Bliesner, B.L., Timmermann, A., Smith, R.S., Lohmann, G., Zheng, W., Timm, O.E., 2014. The Holocene temperature conundrum. Proc. Natl. Acad. Sci. U. S. A. 111, E3501–E3505.

Lochte, A.A., Repschläger, J., Kienast, M., Andersen, N., Hamann, C., Schneider, R., Garbe-schönberg, D., 2019. Labrador Sea freshening at 8.5 ka BP caused by Hudson Bay Ice Saddle collapse. Nat. Commun. 10, 1–9.

Loeb, V., Siegel, V., Holm-Hansen, O., Hewitt, R., Fraser, W., Trivelpiece, W., Trivelpiece, S., 1997. Effects of sea-ice extent and krill or salp dominance on the Antarctic food web. Nature 387, 897–900.

Lohmann, G., Butzin, M., Eissner, N., Shi, X., Stepanek, C., 2020. Abrupt Climate and Weather Changes

Across Time Scales. Paleoceanography and Paleoclimatology 35, e2019PA003782.

Lü, X., Liu, X.-L., Elling, F.J., Yang, H., Xie, S., Song, J., Li, X., Yuan, H., Li, N., Hinrichs, K.-U., 2015. Hydroxylated isoprenoid GDGTs in Chinese coastal seas and their potential as a paleotemperature proxy for mid-to-low latitude marginal seas. Org. Geochem. 89, 31–43.

Lyons, S.L., Baczynski, A.A., Babila, T.L., Bralower, T.J., Hajek, E.A., Kump, L.R., Polites, E.G., Self-Trail, J.M., Trampush, S.M., Vornlocher, J.R., Zachos, J.C., Freeman, K.H., 2019. Palaeocene–Eocene Thermal Maximum prolonged by fossil carbon oxidation. Nat. Geosci. 12, 54–60.

M'boule, D., Chivall, D., Sinke-Schoen, D., Sinninghe Damsté, J.S., Schouten, S., Van der Meer, M.T.J., 2014. Salinity dependent hydrogen isotope fractionation in alkenones produced by coastal and open ocean haptophyte algae. Geochim. Cosmochim. Acta 130, 126–135.

Macdonald, R.W., Sakshaug, E., Stein, R., 2004. The Arctic Ocean: Modern Status and Recent Climate Change, in: Stein, R., Macdonald, R.W. (Eds.): The Organic Carbon Cycle in the Arctic Ocean. Springer, Berlin, pp. 6–21.

Maloney, A.E., Nelson, D.B., Richey, J.N., Prebble, M., Sear, D.A., Hassall, J.D., Langdon, P.G., Croudace, I.W., Zawadzki, A., Sachs, J.P., 2019. Reconstructing precipitation in the tropical South Pacific from dinosterol 2H/1H ratios in lake sediment. Geochim. Cosmochim. Acta 245, 190–206.

Maloney, A.E., Shinneman, A.L.C., Hemeon, K., Sachs, J.P., 2016. Exploring lipid 2H/1H fractionation mechanisms in response to salinity with continuous cultures of the diatom Thalassiosira pseudonana. Org. Geochem. 101, 154–165.

Marcott, S. a., Shakun, J.D., Clark, P.U., Mix, A.C., 2013. A Reconstruction of Regional and Global Temperature for the Past 11,300 Years. Science. 339, 1198–1201.

Marcott, S.A., Bauska, T.K., Buizert, C., Steig, E.J., Rosen, J.L., Cuffey, K.M., Fudge, T.J., Severinghaus, J.P., Ahn, J., Kalk, M.L., McConnell, J.R., Sowers, T., Taylor, K.C., White, J.W.C., Brook, E.J., 2014. Centennial-scale changes in the global carbon cycle during the last deglaciation. Nature 514, 616–619.

Martens, J., Wild, B., Muschitiello, F., Regan, M.O., Jakobsson, M., Semiletov, I., Dudarev, O. V, Gustafsson, Ö., 2020. Remobilization of dormant carbon from Siberian-Arctic permafrost during three past warming events. Sci. Adv. 6, eabb6546.

Martens, J., Wild, B., Pearce, C., Tesi, T., Andersson, A., Bröder, L., O'Regan, M., Jakobsson, M., Sköld, M., Gemery, L., Cronin, T.M., Semiletov, I., Dudarev, O. V., Gustafsson, Ö., 2019. Remobilization of Old Permafrost Carbon to Chukchi Sea Sediments During the End of the Last Deglaciation. Global Biogeochem. Cycles 33, 2–14.

Matsumura, S., Kosaka, Y., 2019. Arctic–Eurasian climate linkage induced by tropical ocean variability. Nat. Commun. 10, 1–8.

Mayot, N., Matrai, P.A., Arjona, A., Bélanger, S., Marchese, C., Jaegler, T., Ardyna, M., Steele, M., 2020. Springtime Export of Arctic Sea Ice Influences Phytoplankton Production in the Greenland Sea. J. Geophys. Res. Ocean. 125, e2019JC015799.

McFarlin, J.M., Axford, Y., Masterson, A.L., Osburn, M.R., 2019. Calibration of modern sedimentary δ2H

plant wax-water relationships in Greenland lakes. Quat. Sci. Rev. 225, 105978.

McManus, J.F., Francois, R., Gherardl, J.M., Keigwin, L., Drown-Leger, S., 2004. Collapse and rapid resumption of Atlantic meridional circulation linked to deglacial climate changes. Nature 428, 834–837.

Meredith, M., Sommerkorn, M., Cassotta, S., Derksen, C., Ekaykin, A., Hollowed, A., Kofinas, G., Mackintosh, A., Melbourne-Thomas, J., Muelbert, M.M.C., Ottersen, G., Pritchard, H., Schuur, E.A.G., 2019. Polar Regions. Chapter 3, IPCC Special Report on the Ocean and Cryosphere in a Changing Climate. IPCC.

Meyer, V.D., Hefter, J., Köhler, P., Tiedemann, R., Gersonde, R., Wacker, L., Mollenhauer, G., 2019. Permafrost-carbon mobilization in Beringia caused by deglacial meltwater runoff, sea-level rise and warming. Environ. Res. Lett. 14, 085003.

Meyers, P.A., 1997. Organic geochemical proxies of paleoceanographic. Org. Geochem. 27, 213–250.

Meyers, P.A., Teranes, J.L., 2002. Sediment organic matter. Springer, Dordrecht.

Mollenhauer, G., Grotheer, H., Gentz, T., Bonk, E., Hefter, J., 2021. Standard operation procedures and performance of the MICADAS radiocarbon laboratory at Alfred Wegener Institute (AWI), Germany. Nucl. Instruments Methods Phys. Res. Sect. B Beam Interact. with Mater. Atoms 496, 45–51.

Monnin, E., Indermühle, A., Dällenbach, A., Flückiger, J., Stauffer, B., Stocker, T.F., Raynaud, D., Barnola, J.M., 2001. Atmospheric CO2 concentrations over the last glacial termination. Science. 291, 112–114.

Müller, J., Massé, G., Stein, R., Belt, S.T., 2009. Variability of sea-ice conditions in the Fram Strait over the past 30,000 years. Nat. Geosci. 2, 772–776.

Müller, J., Stein, R., 2014. High-resolution record of late glacial and deglacial sea ice changes in Fram Strait corroborates ice-ocean interactions during abrupt climate shifts. Earth Planet. Sci. Lett. 403, 446–455.

Müller, J., Wagner, A., Fahl, K., Stein, R., Prange, M., Lohmann, G., 2011. Towards quantitative sea ice reconstructions in the northern North Atlantic: A combined biomarker and numerical modelling approach. Earth Planet. Sci. Lett. 306, 137–148.

Mundy, C.J., Gosselin, M., Ehn, J., Gratton, Y., Rossnagel, A., Palmer, M., Barber, D.G., Martin, J., Arrigo, K.R., Fortier, L., Else, B., Papakyriakou, T., 2009. Contribution of under-ice primary production to an ice-edge upwelling phytoplankton bloom in the Canadian Beaufort Sea. Geophys. Res. Lett. 36, L17601.

Murton, J.B., Bateman, M.D., Dallimore, S.R., Teller, J.T., Yang, Z., 2010. Identification of Younger Dryas outburst flood path from Lake Agassiz to the Arctic Ocean. Nature 464, 740–743.

Nelson, D.B., Sachs, J.P., 2016. Galápagos hydroclimate of the Common Era from paired microalgal and mangrove biomarker 2H/1H values. Proc. Natl. Acad. Sci. U. S. A. 113, 3476–3481.

Nelson, D.B., Sachs, J.P., 2014. The influence of salinity on D/H fractionation in dinosterol and brassicasterol from globally distributed saline and hypersaline lakes. Geochim. Cosmochim. Acta 133, 325–339.

Nelson, D.B., Sachs, J.P., 2013. Concurrent purification of sterols, triterpenols and alkenones from sediments for hydrogen isotope analysis using high performance liquid chromatography. Org. Geochem. 64, 19–28.

Nesje, A., Dahl, S.O., 1993. Lateglacial and Holocene glacier fluctuations and climate variations in western Norway: A review. Quat. Sci. Rev. 12, 255–261.

Nesje, A., Matthews, J.A., Dahl, S.O., Berrisford, M.S., Andersson, C., 2001. Holocene glacier fluctuations of

Flatebreen and winter-precipitation changes in the Jostedalsbreen region, western Norway, based on glaciolacustrine sediment records. The Holocene 11, 267–280.

Niebauer, H.J., Alexander, V., 1985. Oceanographic frontal structure and biological production at an ice edge. Cont. Shelf Res. 4, 367–388.

Nørgaard-pedersen, N., Spielhagen, R.F., Erlenkeuser, H., Grootes, P.M., Heinemeier, J., Knies, J., 2003. Arctic Ocean during the Last Glacial Maximum : Atlantic and polar domains of surface water mass distribution and ice cover. Paleoceanography 18, 1–19.

North Greenland Ice Core Project members, 2004. High resolution record of Northern Hemisphere climate extending into the last interglacial period. Nature 431, 147–151.

Not, C., Hillaire-Marcel, C., 2012. Enhanced sea-ice export from the Arctic during the Younger Dryas. Nat. Commun. 3, 1–5.

Notz, D., Stroeve, J., 2016. Observed Arctic sea-ice loss directly follows anthropogenic CO2 emission. Science. 354, 747–750.

Onarheim, I.H., Årthun, M., 2017. Toward an ice-free Barents Sea. Geophys. Res. Lett. 44, 8387–8395.

Onarheim, I.H., Eldevik, T., Smedsrud, L.H., Stroeve, J.C., 2018. Seasonal and regional manifestation of Arctic sea ice loss. J. Clim. 31, 4917–4932.

Overeem, I., Anderson, R.S., Wobus, C.W., Clow, G.D., Urban, F.E., Matell, N., 2011. Sea ice loss enhances wave action at the Arctic coast. Geophys. Res. Lett. 38, L17503.

Park, H., Watanabe, E., Kim, Y., Polyakov, I., Oshima, K., Zhang, X., Kimball, J.S., Yang, D., 2020. Increasing riverine heat influx triggers Arctic sea ice decline and oceanic and atmospheric warming. Sci. Adv. 6, eabc4699.

Parkinson, C.L., Cavalieri, D.J., 2008. Arctic sea ice variability and trends , 1979 – 2006. J. Geophys. Res. 113, C07003.

Patton, H., Hubbard, A., Andreassen, K., Winsborrow, M., Stroeven, A.P., 2016. The build-up, configuration, and dynamical sensitivity of the Eurasian ice-sheet complex to Late Weichselian climatic and oceanic forcing. Quat. Sci. Rev. 153, 97–121.

Pearce, C., Andrews, J.T., Bouloubassi, I., Hillaire-Marcel, C., Jennings, A.E., Olsen, J., Kuijpers, A., Seidenkrantz, M.-S., 2015. Heinrich 0 on the east Canadian margin: Source, distribution, and timing. Paleoceanography 30, 1613–1624.

Peltier, W.R., Argus, D.F., Drummond, R., 2015. Space geodesy constrains ice age terminal deglaciation: The global ICE-6G_C (VM5a) model. J. Geophys. Res. Solid Earth 120, 450–487.

Peltier, W.R., Vettoretti, G., Stastna, M., 2006. Atlantic meridional overturning and climate response to Arctic Ocean freshening. Geophys. Res. Lett. 33, L06713.

Persson, J., Vrede, T., 2006. Polyunsaturated fatty acids in zooplankton: Variation due to taxonomy and trophic position. Freshw. Biol. 51, 887–900.

Petsch, S.T., Berner, R.A., Eglinton, T.I., 2000. A field study of the chemical weathering of ancient sedimentary organic matter. Org. Geochem. 31, 475–487.

Pickart, R.S., 2004. Shelfbreak circulation in the Alaskan Beaufort Sea: Mean structure and variability. J. Geophys. Res. C Ocean. 109, 1–14.

Pico, T., Mitrovica, J.X., Mix, A.C., 2020. Sea level fingerprinting of the Bering Strait flooding history detects the source of the Younger Dryas climate event. Sci. Adv. 6, eaay2935.

Pieńkowski, A.J., Gill, N.K., Furze, M.F.A., Mugo, S.M., Marret, F., Perreaux, A., 2017. Arctic sea-ice proxies: Comparisons between biogeochemical and micropalaeontological reconstructions in a sediment archive from Arctic Canada. Holocene 27, 665–682.

Poore, R.Z., Osterman, L., Hole, W., Hole, W., 1999. Late Pleistocene and Holocene meltwater events in the western Arctic Ocean. Geology 27, 759–762.

Praetorius, S., Condron, A., Mix, A., Walczak, M., McKay, J., Du, J., 2020. The role of Northeast Pacific meltwater events in deglacial climate change. Sci. Adv. 6, eaay2915.

Proshutinsky, A., Dukhovskoy, D., Timmermans, M., Krishfield, R., Bamber, J.L., 2015. Arctic circulation regimes. Philos. Trans. R. Soc. A Math. Phys. Eng. 373, 20140160.

Rampen, S.W., Abbas, B.A., Schouten, S., Damsté, J.S.S., 2010. A comprehensive study of sterols in marine diatoms (Bacillariophyta): Implications for their use as tracers for diatom productivity. Limnol. Oceanogr. 55, 91–105.

Rampen, S.W., Willmott, V., Kim, J.H., Uliana, E., Mollenhauer, G., Schefuß, E., Sinninghe Damsté, J.S., Schouten, S., 2012. Long chain 1,13- and 1,15-diols as a potential proxy for palaeotemperature reconstruction. Geochim. Cosmochim. Acta 84, 204–216.

Rasmussen, S.O., Andersen, K.K., Svensson, A.M., Steffensen, J.P., Vinther, B.M., Clausen, H.B., Siggaard-Andersen, M.L., Johnsen, S.J., Larsen, L.B., Dahl-Jensen, D., Bigler, M., Röthlisberger, R., Fischer, H., Goto-Azuma, K., Hansson, M.E., Ruth, U., 2006. A new Greenland ice core chronology for the last glacial termination. J. Geophys. Res. Atmos. 111, 1–16.

Reimer, P.J., Austin, W.E.N., Bard, E., Bayliss, A., Blackwell, P.G., Bronk Ramsey, C., Butzin, M., Cheng, H., Edwards, R.L., Friedrich, M., Grootes, P.M., Guilderson, T.P., Hajdas, I., Heaton, T.J., Hogg, A.G., Hughen, K.A., Kromer, B., Manning, S.W., Muscheler, R., Palmer, J.G., Pearson, C., Van Der Plicht, J., Reimer, R.W., Richards, D.A., Scott, E.M., Southon, J.R., Turney, C.S.M., Wacker, L., Adolphi, F., Büntgen, U., Capano, M., Fahrni, S.M., Fogtmann-Schulz, A., Friedrich, R., Köhler, P., Kudsk, S., Miyake, F., Olsen, J., Reinig, F., Sakamoto, M., Sookdeo, A., Talamo, S., 2020. The IntCal20 Northern Hemisphere Radiocarbon Age Calibration Curve (0-55 cal kBP). Radiocarbon 62, 725–757.

Reimer, P.J., Bard, E., Bayliss, A., Beck, J.W., Blackwell, P.G., Christopher Bronk Ramsey, Buck, C.E., Cheng, H., Edwards, R.L., Friedrich, M., Grootes, P.M., Guilderson, T.P., 2013. Intcal13 and Marine13 Radiocarbon Age Calibration Curves 0–50,000 Years Cal Bp. Radiocarbon 55, 1869–1887.

Renssen, H., Geel, B. Van, Plicht, J. Van Der, Magny, M., 2000. Reduced solar activity as a trigger for the start of the Younger Dryas? Quat. Int. 67–71, 373–383.

Retamal, L., Bonilla, S., Vincent, W.F., 2008. Optical gradients and phytoplankton production in the Mackenzie River and the coastal Beaufort Sea. Polar Biol. 31, 363–379.

Ribeiro, S., Sejr, M.K., Limoges, A., Heikkilä, M., Andersen, T.J., Tallberg, P., Weckström, K., Husum, K., Forwick, M., Dalsgaard, T., Massé, G., Seidenkrantz, M.S., Rysgaard, S., 2017. Sea ice and primary production proxies in surface sediments from a High Arctic Greenland fjord: Spatial distribution and implications for palaeoenvironmental studies. Ambio 46, 106–118.

Routson, C.C., McKay, N.P., Kaufman, D.S., Erb, M.P., Goosse, H., Shuman, B.N., Rodysill, J.R., Ault, T., 2019. Mid-latitude net precipitation decreased with Arctic warming during the Holocene. Nature 568, 83–87.

Rudels, B., 2015. Arctic Ocean circulation, processes and water masses: A description of observations and ideas with focus on the period prior to the International Polar Year 2007-2009. Prog. Oceanogr. 132, 22–67.

Sachs, J., Blois, J.L., McGee, T., Wolhowe, M., Haberle, S., Clark, G., Atahan, P., 2018a. Southward Shift of the Pacific ITCZ during the Holocene. Paleoceanography and Paleoclimatology 33, 1383–1395.

Sachs, J., Stein, R., Maloney, A.E., Wolhowe, M., Fahl, K., Nam, S. il, 2018b. An Arctic Ocean paleosalinity proxy from δ2H of palmitic acid provides evidence for deglacial Mackenzie River flood events. Quat. Sci. Rev. 198, 76–90.

Sachs, J.P., Maloney, A.E., Gregersen, J., Paschall, C., 2016. Effect of salinity on 2H/1H fractionation in lipids from continuous cultures of the coccolithophorid Emiliania huxleyi. Geochim. Cosmochim. Acta 189, 96–109.

Sachs, J.P., Schwab, V.F., 2011. Hydrogen isotopes in dinosterol from the Chesapeake Bay estuary. Geochim. Cosmochim. Acta 75, 444–459.

Sachse, D., Billault, I., Bowen, G.J., Chikaraishi, Y., Dawson, T.E., Feakins, S.J., Freeman, K.H., Magill, C.R., McInerney, F.A., Van Der Meer, M.T.J., Polissar, P., Robins, R.J., Sachs, J.P., Schmidt, H.L., Sessions, A.L., White, J.W.C., West, J.B., Kahmen, A., 2012. Molecular paleohydrology: Interpreting the hydrogen-isotopic composition of lipid biomarkers from photosynthesizing organisms. Annu. Rev. Earth Planet. Sci. 40, 221–249.

Sánchez-Machado, D.I., López-Cervantes, J., López-Hernández, J., Paseiro-Losada, P., 2004. Fatty acids, total lipid, protein and ash contents of processed edible seaweeds. Food Chem. 85, 439–444.

Schauer, U., Fahrbach, E., Osterhus, S., Rohardt, G., 2004. Arctic warming through the Fram Strait: Oceanic heat transport from 3 years of measurements. J. Geophys. Res. C Ocean. 109, 1–14.

Schefuß, E., Eglinton, T.I., Spencer-Jones, C.L., Rullkötter, J., De Pol-Holz, R., Talbot, H.M., Grootes, P.M., Schneider, R.R., 2016. Hydrologic control of carbon cycling and aged carbon discharge in the Congo River basin. Nat. Geosci. 9, 687–690.

Schell, T.M., Scott, D.B., Rochon, A., Blasco, S., 2008. Late quaternary paleoceanography and paleo-sea ice conditions in the Mackenzie Trough and Canyon, Beaufort Sea. Can. J. Earth Sci. 45, 1399–1415.

Schmidt, G.A., Bigg, G.R., Rohling, E.J., 1999. Global Seawater Oxygen-18 Database - v1.22 https://data.giss.nasa.gov/o18data/

Schneider Von Deimling, T., Grosse, G., Strauss, J., Schirrmeister, L., Morgenstern, A., Schaphoff, S.,

Meinshausen, M., Boike, J., 2015. Observation-based modelling of permafrost carbon fluxes with accounting for deep carbon deposits and thermokarst activity. Biogeosciences 12, 3469–3488.

Schouten, S., Hopmans, E.C., Sinninghe Damsté, J.S., 2013. The organic geochemistry of glycerol dialkyl glycerol tetraether lipids: A review. Org. Geochem. 54, 19–61.

Schouten, S., Ossebaar, J., Schreiber, K., Kienhuis, M.V.M., Langer, G., Benthien, A., Bijma, J., 2006. The effect of temperature, salinity and growth rate on the stable hydrogen isotopic composition of long chain alkenones produced by Emiliania huxleyi and Gephyrocapsa oceanica. Biogeosciences 3, 113–119.

Scott, D.B., Schell, T., St-Onge, G., Rochon, A., Blasco, S., 2009. Foraminiferal assemblage changes over the last 15,000 years on the Mackenzie-Beaufort Sea Slope and Amundsen Gulf, Canada: Implications for past sea ice conditions. Paleoceanography 24, PA2219.

Screen, J.A., Simmonds, I., 2010. The central role of diminishing sea ice in recent Arctic temperature amplification. Nature 464, 1334–1337.

Serreze, M.C., Barrett, A.P., Slater, A.G., Woodgate, R.A., Aagaard, K., Lammers, R.B., Steele, M., Moritz, R., Meredith, M., Lee, C.M., 2006. The large-scale freshwater cycle of the Arctic. J. Geophys. Res. Ocean. 111, 1–19.

Serreze, M.C., Holland, M.M., Stroeve, J., 2007. Perspectives on the Arctic's Shrinking Sea-Ice Cover. Science. 315, 1533–1536.

Sévellec, F., Fedorov, A. V, Liu, W., 2017. Arctic sea-ice decline weakens the Atlantic Meridional Overturning Circulation. Nat. Clim. Change 7, 604–610.

Sigman, D.M., Hain, M.P., Haug, G.H., 2010. The polar ocean and glacial cycles in atmospheric CO2 concentration. Nature 466, 47–55.

Smik, L., Belt, S.T., Lieser, J.L., Armand, L.K., Leventer, A., 2016a. Distributions of highly branched isoprenoid alkenes and other algal lipids in surface waters from East Antarctica: Further insights for biomarker-based paleo sea-ice reconstruction. Org. Geochem. 95, 71–80.

Smik, L., Cabedo-Sanz, P., Belt, S.T., 2016b. Semi-quantitative estimates of paleo Arctic sea ice concentration based on source-specific highly branched isoprenoid alkenes: A further development of the PIP25 index. Org. Geochem. 92, 63–69.

Smith., W.O., Nelson, D.M., 1985. Phytoplankton Bloom Produced by a Receding Ice Edge in the Ross Sea: Spatial Coherence with the Density Field. Science. 227, 163–166.

Soulet, G., Hilton, R.G., Garnett, M.H., Dellinger, M., Croissant, T., Ogric, M., 2018. Technical note: In situ measurement of flux and isotopic composition of CO2 released during oxidative weathering of sedimentary rocks. Biogeosciences 15, 4087–4102.

Spielhagen, R.F., Erlenkeuser, H., Siegert, C., 2005. History of freshwater runoff across the Laptev Sea (Arctic) during the last deglaciation. Glob. Planet. Change 48, 187–207.

Spielhagen, R.F., Werner, K., Sørensen, S.A., Zamelczyk, K., Kandiano, E., Budeus, G., Husum, K., Marchitto, T.M., Hald, M., 2011. Enhanced Modern Heat Transfer to the Arctic by Warm Atlantic Water. Science. 331, 450–453.

Stein, R., Fahl, K., 2004. The Kara Sea: Distribution, sources, variability and burial of organic carbon. Organic Carbon Cycle in the Arctic Ocean, Springer-Verlag, Berlin.

Stein, R., Fahl, K., Dittmers, K., Nissen, F., Stepanets, O.V., 2003. Holocene siliciclastic and organic carbon fluxes in the Oh and Yenisei estuaries and the adjacent inner Kara Sea: Quantification, variability, and paleoenvironmental implications. Siberian River run-off in the Kara Sea: Characterisation, quantification, variability, and environmental significance 401–432.

Stein, R., Macdonald, R.W., 2004. The organic carbon in the Arctic Ocean, Springer-Verlag, Berlin.

Stein, R., Nam, S.I., Schubert, C., Vogt, C., Fütterer, D., Heinemeier, J., 1994a. The last deglaciation event in the eastern central Arctic Ocean. Science. 264, 692–696.

Stein, R., Schubert, C., Vogt, C., Fütterer, D., 1994b. Stable isotope stratigraphy, sedimentation rates, and salinity changes in the Latest Pleistocene to Holocene eastern central Arctic Ocean. Mar. Geol. 119, 333–355.

Strass, V.H., Nöthig, E.M., 1996. Seasonal shifts in ice edge phytoplankton blooms in the Barents Sea related to the water column stability. Polar Biol. 16, 409–422.

Stroeve, J., Holland, M.M., Meier, W., Scambos, T., Serreze, M., 2007. Arctic sea ice decline: Faster than forecast. Geophys. Res. Lett. 34, L09501.

Stroeve, J., Notz, D., 2018. Changing state of Arctic sea ice across all seasons. Environ. Res. Lett. 13, 103001.

Stroeve, J.C., Kattsov, V., Barrett, A., Serreze, M., Pavlova, T., Holland, M., Meier, W.N., 2012. Trends in Arctic sea ice extent from CMIP5 , CMIP3 and observations. Geophys. Res. Lett. 39, L16502.

Stuiver, M., Reimer, P.J., Reimer, R.W., 2020. CALIB 7.1. http://calib.org.

Sun, S., Meyer, V.D., Dolman, A.M., Winterfeld, M., Hefter, J., Dummann, W., McIntyre, C., Montluçon, D.B., Haghipour, N., Wacker, L., Gentz, T., Van Der Voort, T.S., Eglinton, T.I., Mollenhauer, G., 2020. 14C Blank Assessment in Small-Scale Compound-Specific Radiocarbon Analysis of Lipid Biomarkers and Lignin Phenols. Radiocarbon 62, 207–218.

Svendsen, I., Mangerud, J., 1997. Holocene glacial and climatic variations on Spitsbergen, Svalbard. The Holocene 7, 45–57.

Svendsen, J.I., Alexanderson, H., Astakhov, V.I., Demidov, I., Dowdeswell, J.A., Funder, S., Gataullin, V., Henriksen, M., Hjort, C., Houmark-Nielsen, M., Hubberten, H.W., Ingólfsson, Ó., Jakobsson, M., Kjær, K.H., Larsen, E., Lokrantz, H., Lunkka, J.P., Lysså, A., Mangerud, J., Matiouchkov, A., Murray, A., Möller, P., Niessen, F., Nikolskaya, O., Polyak, L., Saarnisto, M., Siegert, C., Siegert, M.J., Spielhagen, R.F., Stein, R., 2004. Late Quaternary ice sheet history of northern Eurasia. Quat. Sci. Rev. 23, 1229–1271.

Synal, H.A., Stocker, M., Suter, M., 2007. MICADAS: A new compact radiocarbon AMS system. Nucl. Instruments Methods Phys. Res. Sect. B Beam Interact. with Mater. Atoms 259, 7–13.

Syring, N., 2020. Holocene sea-ice and ice-sheet variability on the Northeast Greenland continental shelf. University of Bremen. PhD dissertation.

Syring, N., Lloyd, J.M., Stein, R., Fahl, K., Roberts, D.H., Callard, L., O'Cofaigh, C., 2020a. Holocene Interactions Between Glacier Retreat, Sea Ice Formation, and Atlantic Water Advection at the Inner

Northeast Greenland Continental Shelf. Paleoceanogr. Paleoclimatology 35, e2020PA004019.

Syring, N., Stein, R., Fahl, K., Vahlenkamp, M., Zehnich, M., Spielhagen, R.F., Niessen, F., 2020b. Holocene changes in sea-ice cover and polynya formation along the eastern North Greenland shelf : New insights from biomarker records. Quat. Sci. Rev. 231, 106173.

Tanski, G., Wagner, D., Knoblauch, C., Fritz, M., Sachs, T., Lantuit, H., 2019. Rapid CO2 Release From Eroding Permafrost in Seawater. Geophys. Res. Lett. 46, 11244–11252.

Tao, S., Eglinton, T.I., Montluçon, D.B., McIntyre, C., Zhao, M., 2015. Pre-aged soil organic carbon as a major component of the Yellow River suspended load: Regional significance and global relevance. Earth Planet. Sci. Lett. 414, 77–86.

Tarasov, L., Peltier, W.R., 2005. Arctic freshwater forcing of the Younger Dryas cold reversal. Nature 435, 662–665.

Taylor, A., Blum, J.D., 1995. Relation between soil age and silicate weathering rates determined from the chemical evolution of a glacial chronosequence. Geology 23, 979–982.

Tesi, T., Muschitiello, F., Smittenberg, R.H., Jakobsson, M., Vonk, J.E., Hill, P., Andersson, A., Kirchner, N., Noormets, R., Dudarev, O., Semiletov, I., Gustafsson, 2016. Massive remobilization of permafrost carbon during post-glacial warming. Nat. Commun. 7, 13653.

Turetsky, M.R., Abbott, B.W., Jones, M.C., Anthony, K.W., Olefeldt, D., Schuur, E.A.G., Grosse, G., Kuhry, P., Hugelius, G., Koven, C., Lawrence, D.M., Gibson, C., Sannel, A.B.K., McGuire, A.D., 2020. Carbon release through abrupt permafrost thaw. Nat. Geosci. 13, 138–143.

Vaks, A., Mason, A.J., Breitenbach, S.F.M., Kononov, A.M., Osinzev, A. V., Rosensaft, M., Borshevsky, A., Gutareva, O.S., Henderson, G.M., 2020. Palaeoclimate evidence of vulnerable permafrost during times of low sea ice. Nature 577, 221–225.

Vance, D., Teagle, D.A.H., Foster, G.L., 2009. Variable Quaternary chemical weathering fluxes and imbalances in marine geochemical budgets. Nature 458, 493–496.

Versteegh, G., Bosch, H., De Leeuw, J., 1997. Potential palaeoenvironmental information of C24 to C36 mid-chain diols, keto-ols and mid-chain hydroxy fatty acids; a critical review. Org. Geochem. 27, 1–13.

Volkman, J.K., 1986. A review of sterol markers for marine and terrigenous organic matter. Org. Geochem. 9, 83–99.

Volkman, J.K., Jeffrey, S.W., Nichols, P.D., Rogers, G.I., Garland, C.D., 1989. Fatty acid and lipid composition of 10 species of microalgae used in mariculture. J. Exp. Mar. Bio. Ecol. 128, 219–240.

Vonk, J.E., Drenzek, N.J., Hughen, K.A., Stanley, R.H.R., McIntyre, C., Montluçon, D.B., Giosan, L., Southon, J.R., Santos, G.M., Druffel, E.R.M., Andersson, A.A., Sköld, M., Eglinton, T.I., 2019. Temporal deconvolution of vascular plant-derived fatty acids exported from terrestrial watersheds. Geochim. Cosmochim. Acta 244, 502–521.

Vonk, J.E., Sanchez-Garca, L., Van Dongen, B.E., Alling, V., Kosmach, D., Charkin, A., Semiletov, I.P., Dudarev, O. V., Shakhova, N., Roos, P., Eglinton, T.I., Andersson, A., Gustafsson, A., 2012. Activation of old carbon by erosion of coastal and subsea permafrost in Arctic Siberia. Nature 489, 137–140.

Vonk, J.E., Sánchez-García, L., Semiletov, I., Dudarev, O., Eglinton, T., Andersson, A., Gustafsson, O., 2010. Molecular and radiocarbon constraints on sources and degradation of terrestrial organic carbon along the Kolyma paleoriver transect, East Siberian Sea. Biogeosciences 7, 3153–3166.

Vonk, J.E., Semiletov, I.P., Dudarev, O. V., Eglinton, T.I., Andersson, A., Shakhova, N., Charkin, A., Heim, B., Gustafsson, Ö., 2014. Preferential burial of permafrost-derived organic carbon in Siberian-Arctic shelf waters. J. Geophys. Res. Ocean. 119, 8410–8421.

Wacker, L., Bonani, G., Friedrich, M., Hajdas, I., Kromer, B., Němec, M., Ruff, M., Suter, M., Synal, H.A., Vockenhuber, C., 2010a. Micadas: Routine and high-precision radiocarbon dating. Radiocarbon 52, 252–262.

Wacker, L., Christl, M., Synal, H.A., 2010b. Bats: A new tool for AMS data reduction. Nucl. Instruments Methods Phys. Res. Sect. B Beam Interact. with Mater. Atoms 268, 976–979.

Wacker, L., Němec, M., Bourquin, J., 2010c. A revolutionary graphitisation system: Fully automated, compact and simple. Nucl. Instruments Methods Phys. Res. Sect. B Beam Interact. with Mater. Atoms 268, 931–934.

Wadham, J.L., Hawkings, J.R., Tarasov, L., Gregoire, L.J., Spencer, R.G.M., Gutjahr, M., Ridgwell, A., Kohfeld, K.E., 2019. Ice sheets matter for the global carbon cycle. Nat. Commun. 10, 1–17.

Wagner, A., Lohmann, G., Prange, M., 2011. Arctic river discharge trends since 7ka BP. Glob. Planet. Change 79, 48–60.

Wanner, H., Beer, J., Bütikofer, J., Crowley, T.J., Cubasch, U., Flückiger, J., Goosse, H., Grosjean, M., Joos, F., Kaplan, J.O., Küttel, M., Müller, S.A., Prentice, I.C., Solomina, O., Stocker, T.F., Tarasov, P., Wagner, M., Widmann, M., 2008. Mid- to Late Holocene climate change: an overview. Quat. Sci. Rev. 27, 1791–1828.

Weckström, K., Massé, G., Collins, L.G., Hanhijärvi, S., Bouloubassi, I., Sicre, M.A., Seidenkrantz, M.S., Schmidt, S., Andersen, T.J., Andersen, M.L., Hill, B., Kuijpers, A., 2013. Evaluation of the sea ice proxy IP25 against observational and diatom proxy data in the SW Labrador Sea. Quat. Sci. Rev. 79, 53–62.

Weijers, J.W.H., Schouten, S., van den Donker, J.C., Hopmans, E.C., Sinninghe Damsté, J.S., 2007. Environmental controls on bacterial tetraether membrane lipid distribution in soils. Geochim. Cosmochim. Acta 71, 703–713.

Weiss, M.G., Pfannerstill, Y.E., Schouten, S., Sinninghe Damsté, S.J., Van Der Meer, T.J.M., 2017. Effects of alkalinity and salinity at low and high light intensity on hydrogen isotope fractionation of long-chain alkenones produced by Emiliania huxleyi. Biogeosciences 14, 5693–5704.

Werner, A., 1993. Holocene moraine chronology, Spitsbergen, Svalbard: lichenometric evidence for multiple Neoglacial advances in the Arctic. The Holocene 3, 128–137.

Williams, C., Flower, B.P., Hastings, D.W., 2012. Seasonal Laurentide Ice Sheet melting during the “Mystery Interval” (17.5-14.5 ka). Geology 40, 955–958.

Winsor, P., Chapman, D.C., 2004. Pathways of Pacific water across the Chukchi Sea: A numerical model study. J. Geophys. Res. Ocean. 109, 1–16.

Winterfeld, M., Mollenhauer, G., Dummann, W., Köhler, P., Lembke-Jene, L., Meyer, V.D., Hefter, J., McIntyre, C., Wacker, L., Kokfelt, U., Tiedemann, R., 2018. Deglacial mobilization of pre-aged terrestrial carbon from degrading permafrost. Nat. Commun. 9, 3666.

Wu, J., Mollenhauer, G., Stein, R., Köhler, P., Hefter, J., Fahl, K., Grotheer, H., Wei, B., Nam, S.-I., 2021. Deglacial exhumation of petrogenic carbon and mobilization of thawed permafrost in the Canadian Arctic and their impact on the carbon cycle. To be Submitted.

Wu, J., Stein, R., Fahl, K., Mollenhauer, G., Geibert, W., Syring, N., Nam, S., 2020. Deglacial to Holocene variability in surface water characteristics and major fl oods in the Beaufort Sea. Commun. Earth Environ. 1, 27.

Wunsch, C., 2006. Abrupt climate change: An alternative view. Quat. Res. 65, 191–203.

Xu, C., Yan, M., Ning, L., Liu, J., 2020. Summer westerly jet in northern hemisphere during the mid-holocene: A multi-model study. Atmosphere (Basel). 11, 1193.

Zhang, T., Barry, R.G., Knowles, K., Ling, F., Armstrong, R.L., 2003. Distribution of seasonally and perennially frozen ground in the Northern Hemisphere, in: Proceedings of the 8th International Conference on Permafrost. Zürich, Switzerland: AA Balkema Publishers. pp. 1289–1294.

Zhang, Z., Metzger, P., Sachs, J.P., 2011. Co-occurrence of long chain diols, keto-ols, hydroxy acids and keto acids in recent sediments of Lake El Junco, Galápagos Islands. Org. Geochem. 42, 823–837.

Zhang, Z., Sachs, J.P., 2007. Hydrogen isotope fractionation in freshwater algae: I. Variations among lipids and species. Org. Geochem. 38, 582–608.

Zhu, J., Liu, Z., Zhang, X., Eisenman, I., Liu, W., 2014. Linear weakening of the AMOC in response to receding glacial ice sheets in CCSM3. Geophys. Res. Lett. 41, 6252–6258.